The Pennsylvania State University

The Graduate School

College of Mechanical and Nuclear Engineering

DIGITAL RADIOGRAPHY INSPECTION TOOL FOR LARGE ADDITIVELY MANUFACTURED METALLIC COMPONENTS

A Thesis in

Mechanical Engineering

by

Brant Stoner

Submitted in Partial Fulfillment

of the Requirements

for the Degree of

Master of Science

May 2018

The thesis of Brant Stoner was reviewed and approved* by the following:

Richard P. Martukanitz
Senior Research Associate, Applied Research Laboratory
Thesis Co-Advisor

Sanjay Joshi
Distinguished Professor of Industrial and Manufacturing Engineering
Thesis Co-Advisor

Timothy W. Simpson
Paul Morrow Professor in Engineering Design and Manufacturing
Thesis Co-Advisor

Guha Manogharan
Assistant Professor of Mechanical and Nuclear Engineering

Mary Frecker
Associate Head of Graduate Programs for the Department of Mechanical and Nuclear Engineering
Professor of Mechanical Engineering & Biomedical Engineering

*Signatures are on file in the Graduate School.

Abstract

Through layerwise deposition, additive manufacturing (AM) allows previously unmanufacturable geometries such as organic looking structures and complex internal geometries to be produced. Utilizing these advantages, performance improvements can be gained through techniques such as topology optimization, lattice structures, and part consolidation. Continued improvement of the AM process has shifted the focus of AM to end-use components. Qualification is a key step in enabling AM as an end-use manufacturing method, and the industry has turned to Computed Tomography (CT) as a tool in this process. Although well suited for complex components a few centimeters in size, CT struggles as AM components exceed a meter in length due to limited source energy, restrictive inspection volumes, and excessive data generation. This work proposes Digital Radiography (DR) as a non-destructive inspection method capable of accurately inspecting AM components approaching and exceeding a meter in length. To both expedite the inspection process and make DR a feasible inspection technique, an application, SMART DR was developed to optimize component orientation during the inspection process and provide the probability of detection for flaw sizes of interest prior to manufacturing. By providing this information, SMART DR allows for an inspection plan to be developed or the necessary design changes to be made to ensure that a component can be accurately inspected.

SMART DR utilizes a ray trace algorithm for orientation optimization and experimental data along with theoretical relationships to determine a flaw's probability of detection. A parallelized back projection algorithm utilizes a virtual representation of the user's DR system and a STL representation of the component in question. By projecting the STL facets to the detector and back tracing the X-rays from the detector pixels to the source, the radiographic thickness of the component can be calculated efficiently. To determine the optimal orientation

for inspecting the component, the back-projection algorithm is coupled with a genetic optimization scheme to minimize the radiographic thickness of the component. The probability of detection metric is based off of the contrast-to-noise ratio and normalized image unsharpness.

Due to limited information on high energy DR in the literature, an experimental plan was created to aid in determining the contrast to noise ratio for source energy between 0.450 Mev to 12 Mev and thicknesses from 25.4 mm to 203.3 mm (1 in. to 8 in.). Square Ti-6Al-4V blocks 76.2 mm (3 in.) wide with cylindrical artificial flaws were used during the experiment. The contrast-to-noise ratio was then measured across each flaw based on ASTM standard E2597 while the normalized image unsharpness was determined based on ASTM standard E2698. Combining these two metrics allow for determining a flaw's probability of detection for a wide range of flaw sizes, DR systems, and component thicknesses. Validation was conducted on a 316-stainless steel fin produced using laser based directed energy deposition process. A 0.450 Mev DR system with a 2.5mm spot size and a GE DXR250U-W digital detector array were used during validation. SMART DR produced an optimal orientation that was 40mm thick and predicted that a 0.75 mm diameter flaw with length 0.400mm, .800mm, or 1.60 mm had probability of detection of 91%, 20.7% and 21.7%, respectively. This aligned closely with the smallest detectable flaws on the radiographs of the 316-stainless steel fin, which were 0.508 mm and 0.764 mm. Initial validation results showed that SMART DR is capable of optimizing the DR process and providing accurate probability of detection values within the bounds of the data.

Table of Contents

List of Figures

List of Tables

Acknowledgements

I would like to thank my advisors: Dr. Sanjay Joshi, Dr. Richard Martukanitz, and Dr. Timothy W. Simpson for their immense support and guidance throughout my academic career. Their different areas of focus and expertise provided vital insights and perspectives during my research. Without their guidance, the completion of this work would not have been possible. Furthermore, I would like to thank my advisors for the many experiences and opportunities that not only influenced me as an engineer but my thoughts and views of the world as well.

I would also like to thank Griffin Jones for his invaluable help in developing the probability of detection metric and also for our many impromptu discussions that enabled me to work out the finer points of my work. His expertise and guidance were imperative to the completion of this work.

I am also very grateful for my parents, Brian and Michelle Stoner, and my sister, Emilee Stoner, for their constant love and encouragement throughout my entire life. Because of them, I am the man that I am today, and without them none of this would have been possible. Through their guidance, they instilled in me the beliefs and discipline necessary to achieve my goals. I cannot express how grateful I am for their support through all the highs and lows.

Lastly, I am grateful for my fiancé, Emily Kirschenbaum, for her unwavering love and commitment while I chased my dreams. Her understanding and support while I devoted myself to my work showed me how truly blessed I am to have her. She was my calm in the storm, enabling me to fulfill my dream.

The authors would like to acknowledge the support of the Defense Advanced Research Projects Agency for funding of this work under award DARPA HR001-15-C-0029. The views, opinions and/or findings expressed are those of the author and should not be interpreted as representing the official views or policies of the Department of Defense or the U.S. Government

Chapter 1 Introduction

1.1 Motivation

Since its inception, additive manufacturing (AM) has promised to revolutionize how we design and manufacture products. By producing components in a layer-by-layer fashion, AM reduces complex geometry to a series of two-dimensional layers, enabling the production of components with complexity not possible or too expensive to manufacture by conventional methods. Up until recently, AM has mostly found use in rapid prototyping and tooling applications where AM is used to produce functional prototypes, tools and molds [1]. For example, Sachs et al. [2] demonstrated how conformal cooling channels can be manufactured into injection mold inserts, allowing precise temperature control of both the core and cavity inserts. This has several benefits such as reduced cycle time and increased mold longevity [2]. By only utilizing AM to produce tooling, the full benefit of AM cannot be fully realized because these applications are still constrained by traditional manufacturing methods.

Recent technological advancements along with deeper understanding of the AM process has shifted interest to producing end-use components through AM. The full extent of AM’s capabilities such as topology optimization, functionally graded materials, and part consolidation are possible when designing an end-use component directly through AM. Using AM to reduce the number of components in complex assemblies not only reduces the weight and failure points of a system but also leads to increases in performance. For instance, Schmelzle et al. [3] demonstrated this by additively manufacturing a hydraulic manifold used to test the drag strut retract actuator of the V-22 Osprey by AM. The total number of components was reduced from 17 to one, and overall weight reduction of 60% was achieved along with a height reduction of

53% [3]. Furthermore, improved flow characteristics where attained through the elimination of abrupt flow changes and connection points typical of manifolds produced by traditional means. These success stories along with many others, [e.g. 4-5], are beginning to build confidence in AM as a production-ready manufacturing process.

Qualification of AM components has been identified as a critical roadblock to realizing AM as an end use manufacturing method by the National Institute of Standards and Technology (NIST) in their *Measurement Science Roadmap for Metal-based Additive Manufacturing* [6]. Of particular concern with AM part qualification is the detection of flaws created during the deposition process. A mainstay of AM is being able to precisely control the deposition of material during the manufacturing process. This control allows for extremely complex internal and external geometries to be created, but small perturbations during the building processes can lead to flaws or defects within the component.

Defects within AM components take two main morphologies: (1) porosity and (2) lack of fusion defects [7]. Porosity defects, which are typically created during solidification from absorbed gas species, consist of spherical flaws that can be homogenously or heterogeneously distributed throughout the built material. Lack of fusion defects are introduced by suboptimal processing parameters and occur due to incomplete melting either between or within a layer. Flaws can lead to a reduction of mechanical properties and reduced component life. Determining the presence or lack thereof of these flaws is necessary to qualify AM components for end-use applications.

Because initial applications of AM focused on form and fit prototyping that did not require stringent performance requirements, inspection techniques for AM components are a relatively nascent subject [6]. Many non-destructive inspection (NDI) techniques have been established for the detection of subsurface defects. Techniques such as eddy current and ultrasonic are used extensively in the aerospace industry to inspect welds for similar flaw types found in AM [8]. The issue with eddy current and many of the other subsurface NDI techniques, in reference to AM, is that they only probe a few millimeters into the bulk material. While this is sufficient for surface related defects, these techniques are not sufficient to probe the complex internal geometries typically associated with AM [9].

Because of this, industry has turned to radiography, more specifically Computed Tomography (CT), for the inspection of AM components [10]. CT utilizes X-rays to probe the entire thickness of the component over multiple imaging orientations. From these orientations, a complete three-dimensional reconstruction of the AM component is produced, with all internal and external features. This reconstruction can be analyzed for dimensional accuracy, flaws, and many other characteristics within the entire bulk material. CT's holistic approach has made it one of the leading NDI techniques for the qualification of AM components.

Despite all of the benefits attributed to CT, several drawbacks exist such as small inspection volumes, excessive data generation, and limited X-ray penetration depth [9]. Up until recently this has not been an issue because the components being produced by AM were of a size and complexity that did not exceed the boundaries of CT. The continued advancement of AM has led to the production of components on the scale of multiple feet [11]. These components are not well suited for CT inspection due to their size and sometimes material. A need has arisen within the AM community for NDI techniques that allow for the rapid and efficient inspection of large AM components. These techniques need to be able to probe the internal features of a component and be applicable over a range of materials and thicknesses.

1.2 Objective and Overview of the Approach

In this work, a tool named SMART DR has been developed to assist in the inspection of large AM components. The objective in this work is to optimize the DR inspection process for large AM components by providing optimal radiographic orientations and flaw detectability predictions, thus decreasing the number of radiographs required to obtain qualitative inspection data.

SMART DR utilizes digital radiography (DR) to inspect large components for flaws in much the same way a doctor X-rays a broken bone to see where it is broken. The main goals of SMART DR, with minimal information from the user, is to provide two optimal radiographic orientations from which the size, location, and morphology of potential flaws can be obtained along with a Probability of Detection (POD) for a given flaw size based on system parameters. In comparison to typical NDI techniques, SMART DR looks to expand the range of inspectable geometries while reducing the cost, amount of data analysis, and inspection time for large AM component. In addition, SMART DR brings NDI into the design stage of the AM process. Since only a Standard Tessellation Language (STL) file is required for SMART DR to operate, inspectabiliy of the component can be analyzed throughout the entire iterative design process. Changes to the design can then be made so that qualification can be completed on site or arrangements can be made to outsource the inspection as needed.

To achieve the best radiograph, SMART DR focuses on two major factors, namely, (1) geometric, both part and flaw, and (2) system properties that affect image quality. Geometric considerations are based on component thickness and edge effects. As the thickness of a certain Area Of Interest (AOI) increases, more of the impinging X-rays are attenuated, reducing the contrast of the resultant radiograph. Therefore, an imaging orientation that minimizes an AOI's thickness as seen by the impinging X-rays will produce a radiograph with optimal contrast as opposed to another "thicker" orientation. To achieve this orientation, SMART DR uses a ray trace algorithm to determine an orientation's radiographic thickness based on unique system parameters of the inspection system; coupled with a genetic algorithm, it can identify an optimal radiographic orientation for a specific AOI.

System parameters such as X-ray tube energy, spot size, and detector pitch impact both the contrast and resolution of a radiograph and play an important role in the resulting image quality [9]. Contrast and resolution information of high energy (>450 Kev) DR systems for thicker materials is relatively nonexistent in literature. To obtain this data an experiment was designed to develop a relationship between tube energy, component thickness, and smallest detectable flaw size. A Cumulative Distribution Function (CDF) was derived for each set of tube energy, component thickness, and flaw size from the experimental results. A relationship for contrast and the smallest detectable flaw, was obtained based on the normalized image unsharpness and the CDFs. The normalized image unsharpness equation for radiographic definition was also verified through this experiment. By combining both of these relationships, the POD for a certain flaw size can be generated based on component thickness, tube energy, and the DR system's resolution and Contrast-to-Noise Ratio (CNR). The POD and optimal orientations are presented to the user as an inspection plan with all of the information required to achieve the optimal orientations and the expected image quality in each orientations. Using this information, a user can then assess the inspectability of a component prior to manufacturing and suggest design changes if necessary. Lastly, SMART DR removes the guess work when imaging large components. Since optimal orientations are known, fewer radiographs will be required to inspect a component, which will result in reduction in time, cost, and data analysis.

1.3 Organization of the Thesis

This thesis consists of seven chapters. Chapter 1 provides introductory information and gives a broad overview of the scope and goals of this work. Chapter 2 covers relevant information in current literature of AM processes and NDI and serves to establish the state-of-the-art in these areas. Specifically, the case for using AM as an end-use manufacturing technique is discussed as was as large-scale AM, NDI techniques used for AM, and their drawbacks and benefits. Chapters 3 reviews other similar research and present the workflow and logic behind SMART DR. Chapter 4 demonstrates the process of determining the optimal orientation, evaluating various ray trace algorithms, the logic and performance of the selected ray trace algorithms, as well as selection and performance of the optimization scheme. Chapter 5 reviews the specifics of radiographic image quality, describes the experiment that was conducted to collect relevant data, and discusses how the relationships for high energy contrast and resolution were developed, along with how SMART DR predicts image quality. Chapter 6 presents SMART DR as an application and discusses a validation case. Chapter 7 summarizes the contributions of this work as well areas for improvement and explores future development of utilizing DR for NDI inspection of large AM components.

Chapter 2 Literature Review

2.1 Additive Manufacturing

The advent of additive manufacturing (AM) has created a paradigm shift in the design conceptualization, development, and production of new products and components. AM has found application in the aerospace, medical, and defense industries. By building up a component in a layer-by-layer fashion, Schiller [12] has shown how AM can circumvent conventional restrictions on manufacturability, such as initial tooling costs, manufacturability, and economics of scale. This contrasts with conventional subtractive manufacturing (SM) where material is removed from a primitive billet to form a component.

Regardless of a component's level of complexity, the use of AM reduces a component to a series of consecutive two-dimensional slices. Part geometry becomes uncoupled with manufacturing cost, providing more flexibility in design and complexity. Economy of scale dictates that high production numbers are needed to offset the high capital investment required for SM. AM's ability to produce near net parts with minimal tooling requirements enables medium to one-off production runs to be cost effective, as shown by Eleonora et al [13]. Production of legacy components or low run highly customized parts can thus be done economically with AM due to its small capital investment. This ease of customization enabled Mohammed et al. [14] to develop a patient-specific mandible implant, improving both the functionality of implant and quality of life for the patient. Depending on what benefit of AM is to be leveraged, different AM processes must be used.

AM spans seven different technologies as define by ASTM 52900 [15]. These technologies are Vat Polymerization, Material Extrusion, Powder Bed Fusion, Directed Energy Deposition (DED), Material Jetting, Binder Jetting, and Sheet Lamination. Though methods and applications vary from process to process, the same AM workflow is present in each: CAD model generation, conversion to STL, build orientation determination, support structure generation, toolpath generation, build preparation, production, and if necessary, post-processing. Material extrusion and DED are of particular interest to this study due to their ability to produce large structures on the scale of many meters that pose a particular challenge to qualification.

2.1.1 Material Extrusion

Material extrusion produces components by melting plastic in either filament or pellet form using a heated nozzle, and the plastic melt is then selectively deposited using a Computer Numerical Control (CNC) gantry system to form a layer. Each layer is deposited onto the previous layer until the entire component is manufactured. Typical material extrusion printers such as the Makerbot Replicator have a build volume that allow them to produce components of several centimeters in length[16]. Oak Ridge National Laboratory (ORNL) has taken this technology and scaled it extensively with their Big Area Additive Manufacturing (BAAM) printer which has a build volume of 6.1 m. x 2.44 m. x 1.82 m [17]. This increased build volume enables a wide range of applications in the aerospace, rail, and energy industries. ORNL has already demonstrated the technology by producing a 50ft wind turbine blade mold for the U.S. Department of Energy [18]. Utilizing AM these molds were able to be produced significantly faster and have superior thermal properties as opposed to the traditionally manufactured molds.

2.1.2 Directed Energy Deposition

In a process analogous to laser cladding, DED builds up components through layer-by-layer the successive deposition of weld beads. Either an electron beam or laser is used to produce a melt pool on the build plate, metal wire or powder is then fed into the melt pool to form a bead. Successive weld beads are deposited beside each other to produce a layer. This occurs layer-by-layer until the final component is realized. DED machines such as Sciaky's EBAM systems have been leveraged by both the aerospace and defense industries to produce high lead time components multiple meters in length. By utilizing DED to produce a near net shape of a chord preform Stecker et al. [19] was able to drastically reduce the cost and lead-time required to produce this part by traditional manufacturing using the Sciaky process. By producing a near net shape, 75% less material was required to manufacture the chord and machining time was reduced by 83% making up most of the cost savings. The Applied Research Laboratory was also instrumental in developing a laser-based large DED process capable of building shapes representing a cubic meter of material. DED processes have also been combined with traditional subtractive CNC to create a hybrid system such as the Lasertec 65 produced by DMG Mori that combine the geometric freedoms of AM with the precision and surface quality of CNC machining [20]. In subtractive methods a boss or flange would have to be machined out of an initial oversized billet, whereas hybrid manufacturing enables the deposition and final machining of features onto a smaller billet and in a single machine. Taku [21] has shown that this reduction in initial material cost gives hybrid manufacturing a considerable cost advantage when producing multi-featured parts.

2.2 Non-Destructive Inspection

Non-destructive inspection (NDI) encompasses a range of test methods used to examine or inspect a component that do not affect its future usefulness [9]. These methods give many industries the ability to inspect and qualify critical components both prior to and during their service to ensure their continued safe performance. NDI methods can be used to test for a wide range of potential defects such as surface cracks, internal voids, and wall thinning. Developing NDI procedures and techniques for AM is a crucial hurdle to enabling the production and qualification of end-use parts using AM processes [10]. It has been shown that while porosity and lack of fusion defects typical of AM have a minimal impact on static properties of the material, they have a significant impact on the dynamic properties, such as fatigue and creep of AM manufactured components [22]. To inspect the complex geometries and internal features typical of small AM components for these defects, Computed Tomography (CT) is often the NDI method of choice discussed next.

2.2.1 Computed Tomography

Computed tomography (CT) was developed in the early 1960s as a method for imaging soft tissues within the body by irradiating the target area and measuring the attenuated rays that passed through [23]. The initial medical nature of this process meant high throughput and low dosage were used to minimize the amount of exposure to the patient. The eventual adoption of CT for industrial use saw the removal of these restrictions, allowing for a wide variety of sizes and energy levels [9]. CT produces a full three-dimensional reconstruction containing all external and internal features that can then be inspected for various types of flaws, such as porosity and lack of fusion defects. To achieve this, the component in question is irradiated by an x-ray source from many angles encircling the component, and the transmitted x-ray intensities are captured by a detector. The linear attenuation coefficient is then calculated for each pixel on the detector from which a cross-sectional slice of the component can be reconstructed. Each of these slices views the component as if it was sectioned at the slicing plane and viewed from the top. A complete three-dimensional reconstruction of the component is created by assembling all of the slices together.

From this three-dimensional reconstruction, the various defects that arise from the AM process such as porosity and lack of fusion defects can be identified. Fabien et al. [24] demonstrated CT's ability to capture fine porosity and defects in AM processed components. To do this, three different geometries - a cube, a cylinder, and a triangular prism - were manufactured in several different orientations with misaligned hatching patterns to induce flaws. Within the CT reconstruction of the components, large lack of fusion defects, produced by the misalignment, with sizes on the order 1mm were evident along with randomly distributed fine porosity. The equivalent void diameter of the porosity was 20 to 35 μm, validating CT's ability to inspect AM manufactured components.

Despite CT's many benefits, there are also drawbacks inherent to the system. The many angles approach that allows CT to produce three-dimensional reconstructions also requires thousands of images, making the inspection time encompass multiple hours for a single component. Inspecting low production runs becomes costly and time-consuming and medium production runs unfeasible. Limited inspection volumes and low source energies further restrain the applicability of CT to AM due to restrictions on component size and thickness. Lastly, analysis and manipulation of CT data can be tedious due to the large file sizes produced during the inspection.

2.2.2 Digital Radiography

Digital Radiography (DR), a precursor to CT, similarly uses the attenuation of x-rays to capture the projected image on a digital detector using only a single orientation, producing a two-dimensional projection of the component with geometries superimposed on top of one another. Applications for DR range from the inspection of welds and castings to luggage and cargo inspection [9]. Alkhimov et al. [25] used DR to inspect for porosity in titanium to titanium and titanium to 12X18H10T steel laser welded joints. These high-performance metals used in the aerospace industry exhibit a high tendency to produce pores during the welding process. Using DR, Alkhimov et al. [25] were able to achieve a relative contrast sensitivity of 1 to1.5% with exposure times two to three times lower than conventional film radiography and still detect pores greater than 0.1mm, validating DR for inspection of critical components. Udod et al. [26] compiled a state-of-the-art review of DR citing major advances in matrix detectors and inspection methods which have allowed DR to meet or exceed the capabilities of more traditional film radiography. Their review also projected that future DR research would focus on improving source quality, resolution and contrast of detectors, and developing efficient algorithms for analysis.

In comparison to CT, DR lacks the ability to derive three-dimensional information about flaws from a single setup like CT, but, is significantly faster and produces a more manageable data set. This limitation can be negated, though, if multiple DR images are taken from different orientations. This method is called multi-radiography. Three-dimensional information can then be derived through coordinate transformations from the imaged orientations to a known initial orientation. Crucial for multi-radiography is the detection of flaws in the radiograph, which is typically done by comparison with a reference image. Several different methods for creating a reference image have been studied by Domingo et al. [27], most notably simulation, filtering, and learning. By using a parametric model with or without the aid of a CAD model, an ideal reference image can be created, though model development is time-consuming and difficult to tune. Applying filters to the current radiography to detect flaws requires no previous information other than flaw size; however, issues arise with false detection of component geometry as flaws [28]. Neural networks can also be taught to identify defects through an initial learning process, but they are time-consuming and sensitive to positioning errors.

Once potential flaws or indications have been identified attempts are made to track the indications across a range of different orientations [29]. Tracking of indications has two purposes. First, false positives can be eliminated if the indication cannot be tracked through all images. Second, information regarding the size, location, and morphology can be obtained by successive coordinate transformations between the images. Utilizing multi-radiography along with the current advances in detector quality and flaw detection algorithms, digital radiography has become a viable inspection technique for additively manufactured components. When compared to CT, DR provides a cheaper and faster alternative while still achieving the required contrast and resolution. In the next chapter DR will be discussed in more detail along with the development and workflow for SMART DR.

Chapter 3 NDI using Digital Radiography

3.1 Introduction to Digital Radiography

3.1.1 Major Components

In order to understand the work presented within this thesis, a basic knowledge of the DR inspection process is required. There are two major components of a DR system, the X-ray source and the Digital Detector Array (DDA), as seen in Figure 1.

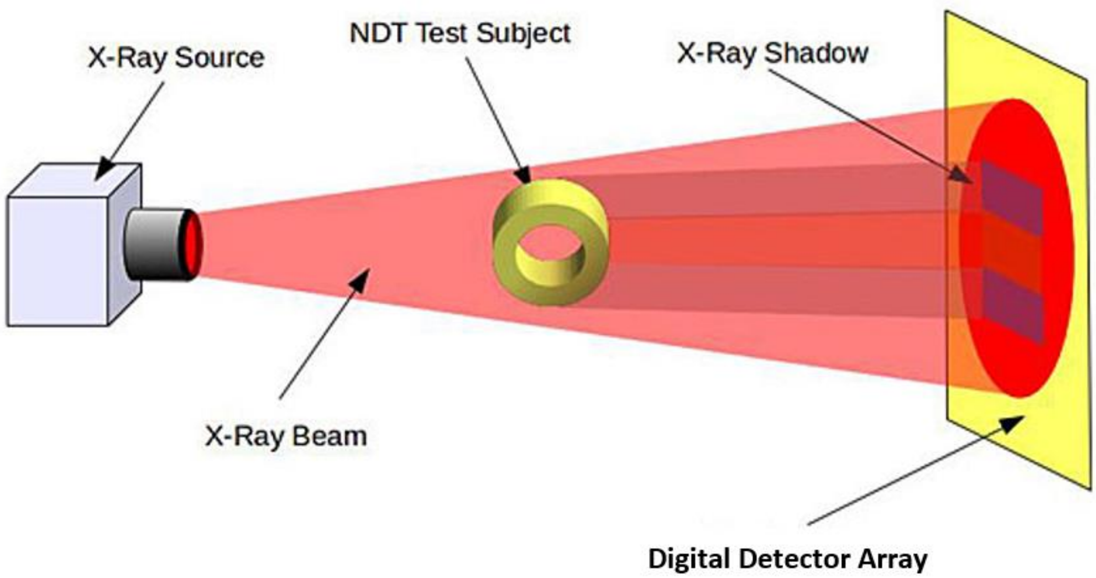

Figure 1 DR schematic

The X-ray source is where the generation of x-rays occurs, and the typical x-ray tube source consists of a cathode and anode. By applying an accelerating voltage across the cathode and anode, electrons are emitted from a filament at the cathode by a process called thermionic emission, shown in Figure 2A. When the electrons impact the anode, their energy is converted into x-ray radiation. This type of x-ray source is often described as “bremsstrahlung” or “braking” radiation source, where the electrons traveling from the cathode are decelerated at a target material through various atomic interactions with that material.

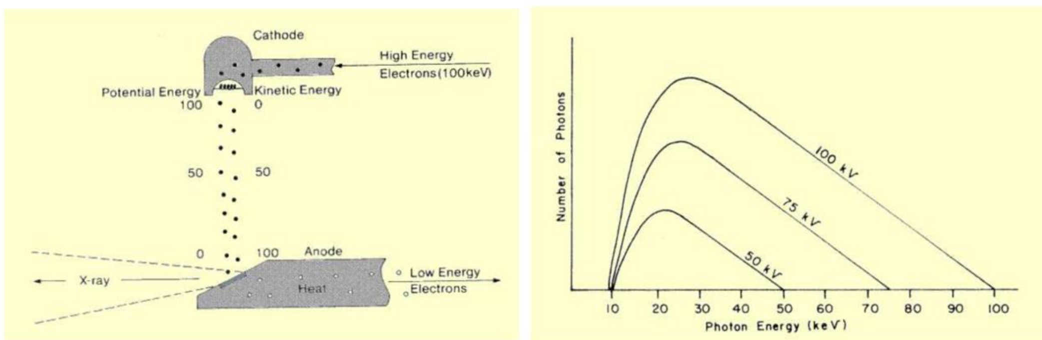

A. B.

Figure 2 A. Diagram of X-ray Tube B. Number of Photons vs, Photon Energy as a function of Accelerating voltage [30]

From the conservation of energy, the deceleration of the electrons is accompanied by the emission of photons in the form of x-ray radiation. The maximum energy of photons emitted through “bremsstrahlung” interactions is determined by the accelerating voltage, as seen in Figure 2B. This spectrum of radiation is what is used for radiographic imaging of components. At lower energies (≤ 450keV), only low density material or thin components (≤ 100 mm of Ti) can be imaged while higher energies (> 450keV) of interest to this study allow a wider range of material and thicknesses (>100 mm of Ti) to be imaged.

The DDA is made up of a pixelated array of conversion and capturing layers. The conversion layer converts x-rays into visible light or luminescence. This luminescence is then converted into an electric signal by each pixel of the capturing layer. Through several stages of modification each pixel is eventually given a grayscale value and combined to produce the resulting radiograph image. Variations in grayscale values are produced by differing amounts of attenuation as the x-rays pass through the component and interact with the DDA. Thicker or denser sections of the component result in more attenuation. Figure 3A shows a CAD model of a Hastelloy step block that was produced by powder bed fusion with various sizes and morphologies of flaws. The different step thicknesses along with the different flaw sizes produce different levels of attenuation that manifest as the different grayscale values as seen in Figure 3B. Thickness is just one of the many factors, such as focal spot size and magnification, which affect the image quality of a radiograph.

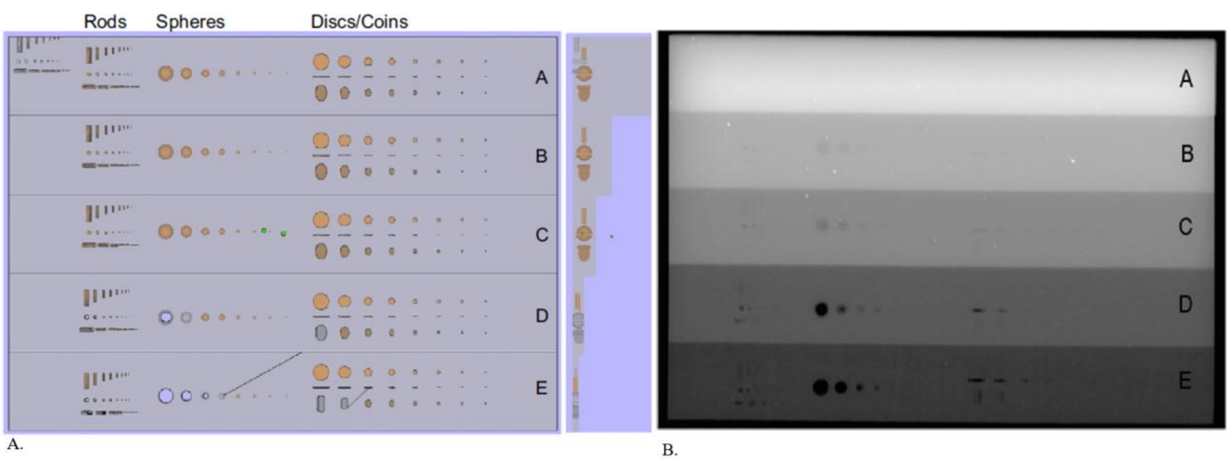

Figure 3 A. CAD model of a Hastelloy X step block that was produce by PDF. The steps range from 10mm to 0.8 mm. B. An X-ray image of manufactured step block [31]

3.1.2 <u>Image Quality</u>

Radiographic image quality can be defined as a function of radiographic definition and radiographic contrast. Radiographic definition refers to the smallest resolvable feature on a radiograph and is related to the total image unsharpness [32]. Radiographic contrast is the difference between grayscale values at two different regions of a radiograph and is related to the contrast-to-noise ratio. Both contrast and definition are required to achieve an acceptable level of image quality, and the improvement of one can lead to the reduction of the other [9]. Radiographic image quality is a multi-faceted and highly coupled topic that encompasses the entirety of the DR process. What follows is a brief description of both radiographic definition and radiographic contrast.

Total image unsharpness is a cumulative metric that combines all contributors to unsharpness into a single parameter. The key components of total image unsharpness are geometric and inherent unsharpness. Geometric unsharpness relates to how the geometry of the inspection system affects the radiographic quality, specifically the focal spot size and geometric magnification. Physical limitations prevent x-ray sources from being a point source; therefore, the x-ray sources used for DR have a finite size or focal spot size. This sub-optimal source geometry produces an overlapping of edges in a radiograph due to differing ray perspectives, which is called the penumbra, as illustrated in Figure 4.

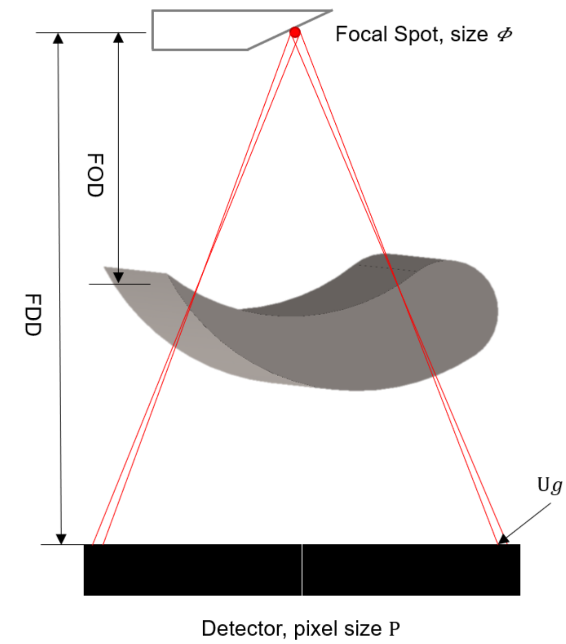

Figure 4 Penumbra diagram

Focal spot sizes vary from tube to tube and can be mini-, micro-, or nano-focused for lower energy (<300 Kev) systems. The smaller the focal spot size, the more the source behaves like a point source, and the unsharpness due to this affect is reduced. For higher energy systems, the focal spot size, is on the scale of a couple millimeters and can contribute significantly to the radiographic image quality.

Geometric magnification is introduced by placing the component between the source and the detector; the closer the component is placed to the source, the greater the magnification. This causes the irradiated geometry to be scaled based on the geometric constraints of similar triangles. Therefore, geometric magnification increases the apparent size of component features, but it also exaggerates the penumbra. Both focal spot size and geometric magnification can be combined into a single term called geometric unsharpness, U_g, as shown in Equation 1 [33], where φ is the focal spot size and υ is the magnification.

$$U_g = \varphi * (\vartheta - 1) \qquad \text{Equation (1)}$$

Inherent unsharpness comes from limiting factors of the DDA used during imaging, most notably the Basic Spatial Resolution (SR_b). SR_b is the smallest geometrical detail that can be resolved using a particular DDA and is related to and slightly larger than the pitch of the DDA [34] . If a DDA has 200 micron pitch, then its SR_b will be approximately 250 microns. The SR_b of a DDA is provided by the manufacturer when purchased and is routinely checked with the use of a duplex wire gauge shown in Figure 5. A line trace is taken that bisects each pair of wires, and the SR_b is calculated as described in ASTM E2002 [35].

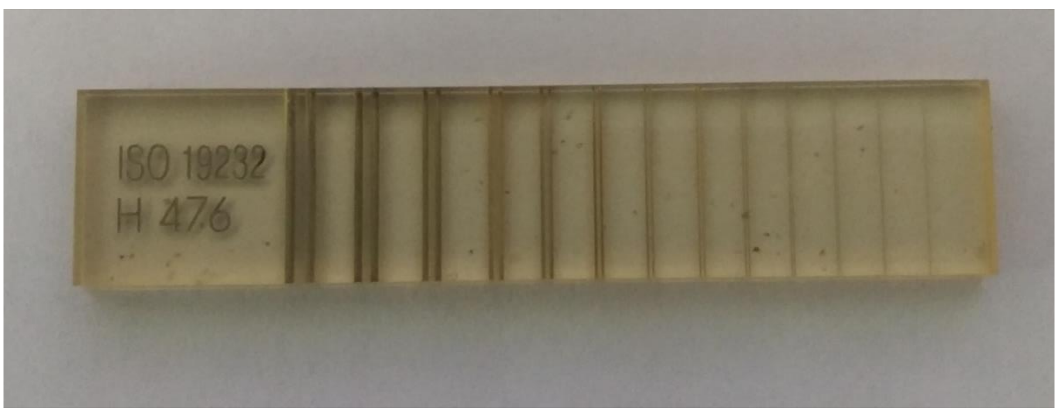

Figure 5 Duplex Wire gauge used to calculate the SR_b

Radiographic contrast is affected by material type and thickness, beam energy, beam flux and DDA performance [9]. As a material's density increases, so does its ability to attenuate x-rays, which reduces the number and energy of incident x-rays on the DDA. Stainless steel, for example, is denser then Ti-6A-4V alloy and would have a higher attenuation coefficient. As a component's thickness increases, so does the attenuation of the x-rays, reducing the contrast of flaws to the bulk material surrounding the thicker area, as seen in Figure 3B. The beam energy (kV) and beam operating current need to be appropriate for the material and component thickness to be imaged. If the beam energy or operating current is to low then not enough photons will reach the DDA. If they are too high. then the DDA will be saturated. A DDA's quantum efficiency, among other performance metrics, impacts how efficiently a DDA converts photons into an electrical signal. High quality DDAs allow for this conversion more easily, absorbing more photons, and increasing image contrast.

3.1.3 Inspection Process

To inspect a component, the appropriate DR system must be selected based on the material and component thickness, as shown in Figure 6. The system's source energy, inspection volume, and image quality limit the components and materials that can be inspected within a given system. A higher source energy is required for materials of greater radiographic attenuation, and only components that can fit within the inspection volume can be imaged. Also, the system must have the radiographic definition and contrast to detect flaws of the desired length scale.

When these conditions are defined, a manual iterative loop is typically utilized to find an acceptable orientation, which is based on the operator's experience and intuition [33]. The component is placed between the source and the DDA based on the desired magnification and orientated based on the area of interest. Both the magnification and component orientation can be non-intuitive, especially for complex AM components, even for an experienced user. Imaging parameters such as exposure time and operating current are then determined based on obtaining an acceptable image quality. The operator must then decide if the area of interest has the required level of definition and contrast to resolve flaws of the desired length scale. If not, then this process is repeated with changes to the magnification, orientation, and imaging parameters until a flaw has been identified or the user is convinced that the component meets the qualification requirements. This is a time-intensive and expensive process, especially for larger components that do not fit within the bounds of the detector. SMART DR has been designed to eliminate this manual iterative process and to remove the uncertainty in radiographic orientation and flaw detectability for digital radiography. The process and workflow behind SMART DR are discussed next in Section 3.2.

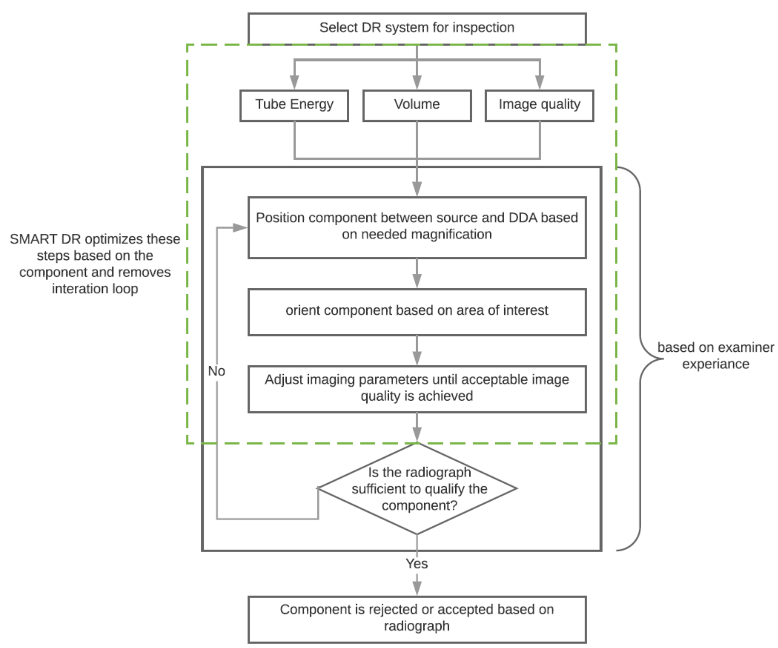

Figure 6 DR inspection workflow

3.2 SMART DR

3.2.1 Application and Benefits

As the technology and understanding of AM processes continues to grow, the design tools and methodologies, simulation methods, and machines need to concurrently advance. The same can be said for qualification methods and NDI. AM components, with their internal structures and complex geometries, has pushed the boundaries of NDI techniques since AM's inception. The initial small size of AM components allowed for CT to adequately inspect components for flaws and defects. As the size of components capable of being manufactured through AM continues to grow, this is no longer possible due to the restrictive size of CT inspection volumes and limited x-ray energy sources.

To meet this need SMART DR was developed to optimize NDI of large AM components through DR and act as an inspection tool and design aid. One of the challenges with DR is the placement and orientation of the component as one orientation may be radiographically superior to another, and for complex components this is relatively unintuitive. Discovery of a radiographically acceptable orientation through trial and error methods is time-consuming and costly. SMART DR takes into consideration the examiner's specific system parameters and through the use of a ray tracing algorithm, coupled with a genetic algorithm, determines the optimal orientation for imaging.

A DR system must also be able to produce a radiograph of sufficiently high quality to resolve a defect representing a critical flaw size. Using novel high energy DR, data SMART DR provides a Probability of Detection (POD) for various flaw sizes of interest, allowing the examiner to ensure imageability prior to inspection. Together, by determining the optimal radiographic orientations and the POD of critical flaw sizes, SMART DR can provide an in-depth evaluation of a component's inspectability prior to manufacturing.

Production of large AM components is of little benefit unless these components can be inspected and qualified. By leveraging SMART DR, the inspectability of a component can be analyzed during the design stage. Questions such as will in-house DR systems be sufficient or where can the component be inspected can be answered long before it is manufactured. Designs can even be modified to improve inspectability, or if a critical area cannot be inspected, then extra safety measures can be incorporated into the design.

3.2.2 Interface and Workflow

To facilitate a better user experience and effective use of SMART DR, a Graphical User Interface GUI was developed using Matlabs GUIDE interface, which is illustrated in Figure 7. GUIDE provides a platform for designing GUI's with prebuilt objects such as push buttons and user editable text boxes. Using these objects, SMART DR's GUI can be broken into three different regions. Region 1 consists of a graphical window that displays the component within the virtual DR system to the user. This window is updated during each step of the SMART DR workflow to help the user visualize the positioning of the component within the system. Basic user manipulation of the component, such as orbiting and panning are also done within this window. Region 2 is where all inputs and parameter selection are conducted. User actions and application outputs are shown in Region 3. This provides the user with necessary information to properly position and image the component. Additionally, a step-by-step log of all the user inputs allows for results to be easily reproduced.

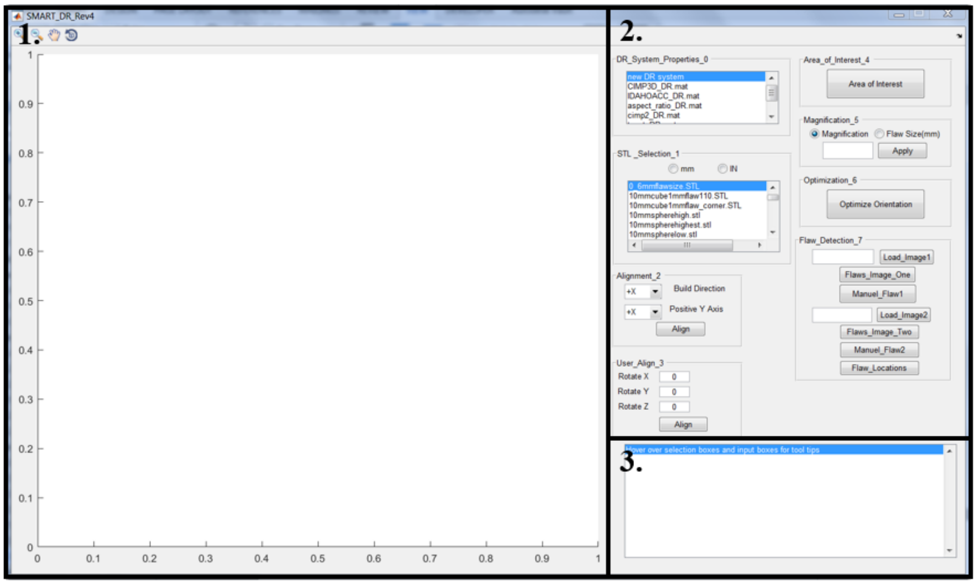

Figure 7 SMART DR GUI

SMART DR provides design and inspection insight through a generalized approach, allowing for a wide range of applications. Due to this consideration, specific imaging parameters will not be predicted for individual DR systems. The difficulties of defining system settings for images are twofold. First, the probabilistic nature of detectors and x-ray tubes create responses that not only vary from machine to machine but a particular detector or x-ray tube response can vary depending on age and maintenance. Second, the metrics that define the responses of these systems, such as the Modular Transfer Function (MTF) or polychromatic spectrum of the x-ray tube, are difficult to measure and are not readily available to an engineer or technician. Here, input parameters were chosen based on the minimum requirements for defining a virtual DR system within the software and information that is typically known for a given DR system. A total of seven inputs were chosen and can be grouped into three different categories - detector inputs, source inputs, and system inputs - as seen in Table 1.

Table 1 SMART DR inputs

Detector	Source	System
Pixel size/Pitch (mm)	Energy (Kev)	Operating Distance
Width (pixels)	Spot size (mm)	
Height(pixels)		
Basic spatial resolution		

Detector parameters define the area of the detector as well as the pixel size. These three parameters are used to produce a grid of points that represent the center of every pixel. Source energy and spot size allow for resolution and contrast prediction which in turn define the smallest detectable flaw size of a DR system. Lastly, the operating distance defines the relative distance between the source and the detector. These six input parameters were chosen because within the context of SMART DR they fully define a DR system and are easily obtainable by an operator. Even though the number of inputs is minimal, the following work shows that a robust predictive NDI software can utilize this information to guide the development of a NDI process.

The workflow for SMART DR can be seen in Figure 8. The first step is loading the desired DR system parameters into the application. If a previous unused DR system is to be analyzed, then a new parameter file is constructed and loaded. The units for the STL are then chosen, and the STL is selected and displayed in the graphic window. Initial placement is conducted out by aligning the STL coordinate system with the virtual DR coordinate system. To do this, the user is asked which axes of the virtual DR coordinate system are aligned with the build direction and the positive y axis of the STL in the graphical window. Further adjustments can be made to the component's initial placement through user-specified angles, or if no adjustments are required, then the operator can proceed to the Area of Interest (AOI) selection step.

The source is initially centered on the component's geometric center based on its bounding box. The center of the source can be moved to an AOI by dragging a box over the AOI, which is shown in Figure 9. A desired magnification or imageable flaw size is then selected. Optimization of the components orientation is next, and depending on time constraints a partial, full, or user specified number length of optimization is performed. Optimization is conducted by a ray trace algorithm coupled to a genetic algorithm that is discussed in Chapter 4 Achieving Optimal Radiographic Perspective. SMART DR then creates an inspection plan with all of the necessary information to position the component in the optimized orientation for imaging.

Using the DR system parameters, along with the optimized orientation, the POD for flaw diameters of interest can be determined. If the POD indicates that the flaw size of interest is not able to be resolved, then a different DR system with higher resolution is required to properly inspect the component. Any further adjustment of the components orientation will increase the radiographic thickness, resulting in a reduction in image quality. The development of the POD is explained in detail in Chapter 5 Predicting Radiographic Image Quality. At this point, radiographs can be taken and analyzed in SMART DR or utilizing a secondary software can be used. Detailed descriptions of both the ray trace algorithm and image quality metrics are discussed in the next chapters along with a validation case for SMART DR.

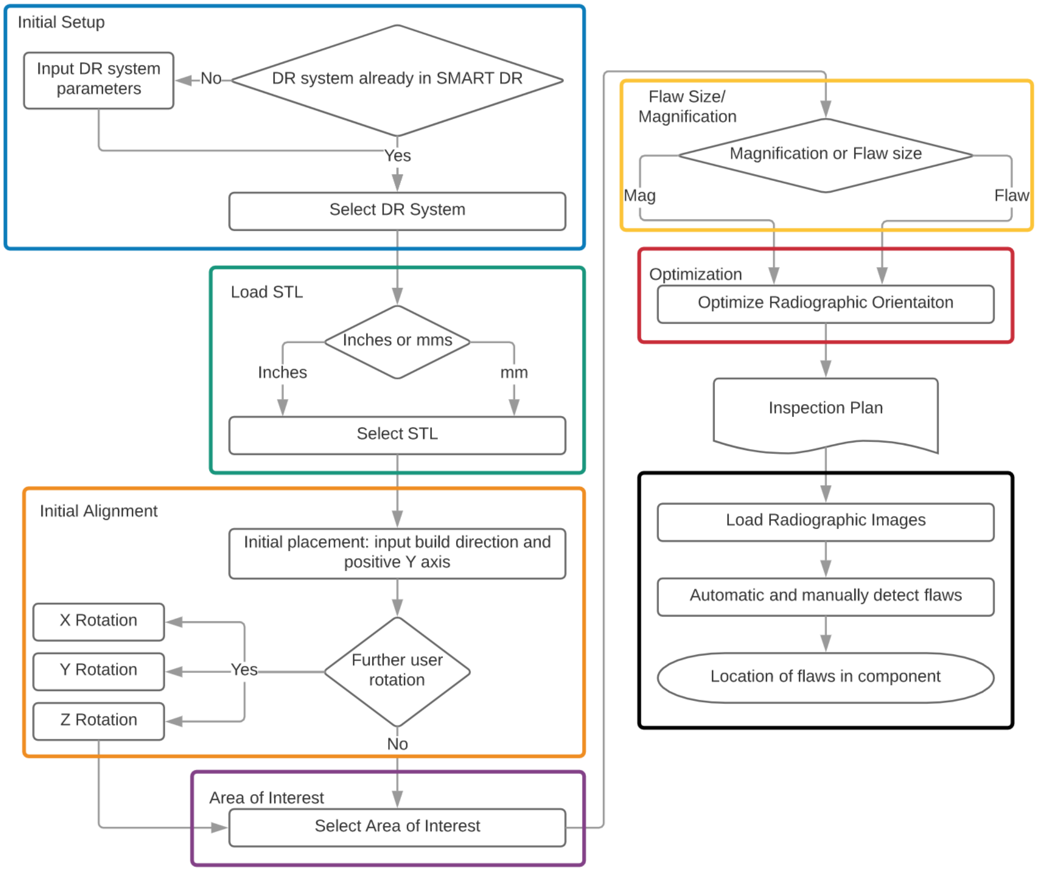

Figure 8 SMART DR Workflow

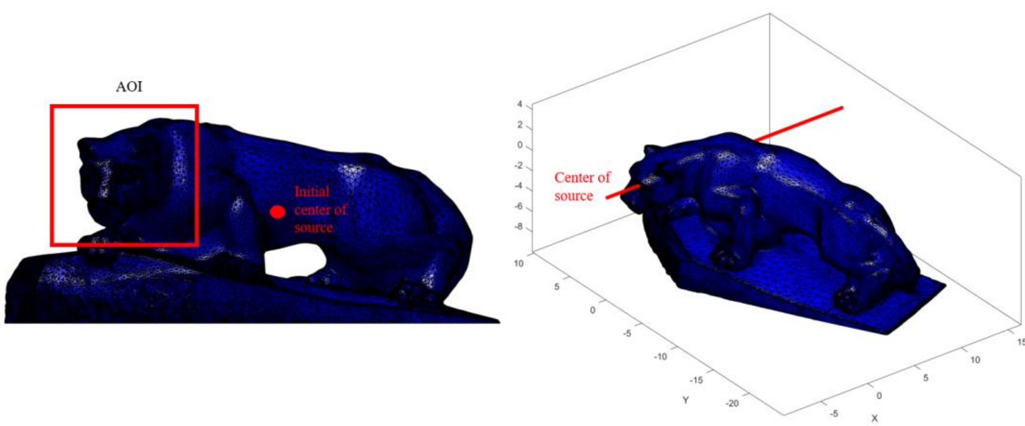

Figure 9 AOI selection

Chapter 4 Achieving Optimal Radiographic Perspectives

4.1 Applications of Ray Trace Algorithms

Designed to simulate the path of rays or waves through a medium, ray trace algorithms have found many applications, such as dosing calculations for radiation treatments [36] and complex volume rendering [37]. In their simplest form, ray trace algorithms are used to determine the intersections of a ray with a given solid. Rays are able to interact with the solid in several different ways depending on the purpose of the algorithm. In the case of determining radiation dosing for proper treatment of tumors, the solid is transmissive to the ray. The path length of a ray through the solid is then used to determine the attenuation coefficient and the resultant dosage to the patient. Sibbion [38] utilized this method to develop an efficient algorithm to find the ray path length for CT scan data. By discretizing CT scan data into prismatic slices, Sibbion was able to reduce the complexity of the problem from R^3 to R^2, which greatly reduced computational time [38]. The goal of SMART DR's ray trace algorithm is much the same, namely to determine the maximum ray path length for a specific orientation of a component and optimize this orientation to minimize the maximum ray path length.

4.2 SMART DR's Back Projection Algorithm

A back projection ray tracing scheme was selected for determining the ray path length needed to compute the attenuation through the component, as opposed to a forward projection scheme, because of its speed and robustness. This can be attributed to the method by which a back projection scheme solves for a photon or ray path. A forward projection scheme evaluates the projection created starting from the photons emitted by a source. These photons interact with an object and scatter in random directions, with only a few hitting a receptor (eye, charged couple device, DR detector, etc.). Following this logic, to determine the image on the receptor would mimic reality, thousands of unnecessary photon paths would have to be calculated, resulting in a slow and problematic algorithm. Back projection algorithms apply this logic in reverse and follow a ray from the receptor back to the source. This eliminates unnecessary ray paths from being calculated, producing a much more efficient and robust algorithm.

Many different back projection schemes have been developed over the years. Of particular interest to this study is an x-ray simulation code called Virtual X-ray Imaging (VXI) developed by Freud et al. [39]. VXI's deterministic ray trace approach is a powerful alternative to time-consuming Monte Carlo simulations of radiographic imaging. Both coherent and Compton scattering effects can be simulated, and geometric unsharpness can be taken into account quite easily through coupling with Computer Aided Design (CAD) software. Of most importance is VXI's ability to handle triangular faceted geometries such as STL representations. By utilizing STL files, it is then possible to analyze any additively manufactured components because the current AM design process necessitates the creation of an STL file. Faceted geometries also account for most of the speed associated with the VXL back projection algorithm by reducing complex geometries to a series of triangles in three-dimensional space. Each triangle is projected onto the detector as if being illuminated by a source. This concept is illustrated in

4.2.2 Ray Trace Logic

Since a usable STL is watertight, meaning that there are no missing triangles on the boundary, a ray from the source to a pixel must intersect the STL N_p*2 times, where N_p is the number of instances of intersections for a given pixel p, as shown in Figure 10. To determine the ray path length through the STL, the ray trace algorithm uses these intersection points. The ray tracing process consists of three major steps: (1) facet projection, (2) inclusion determination, and (3) ray length calculation. Figure 11 shows the high-level flow chart of each of these three stages. At the beginning of the algorithm, the virtual DR system properties and the STL file of the component are loaded. The virtual DR system consists of a structured array containing the energy and spot size of the DR system, DDA dimensions, pixel size, and the distance from the source to the DDA defined by the user. An N x 3 matrix defines the STL file that has N vertices, where there are N/3 triangles and each row is an {x, y, z} vertex of a triangle.

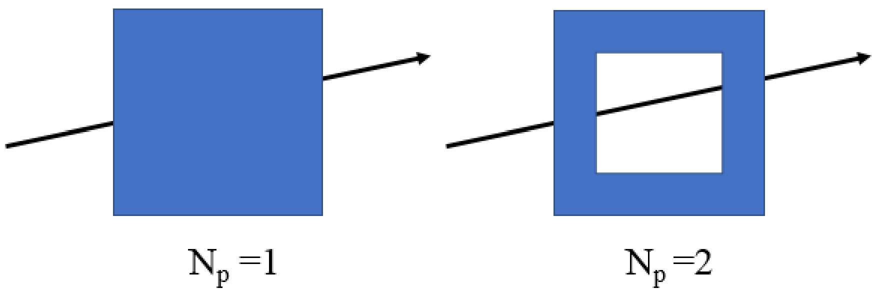

Figure 10 Examples of Different Intersection Types

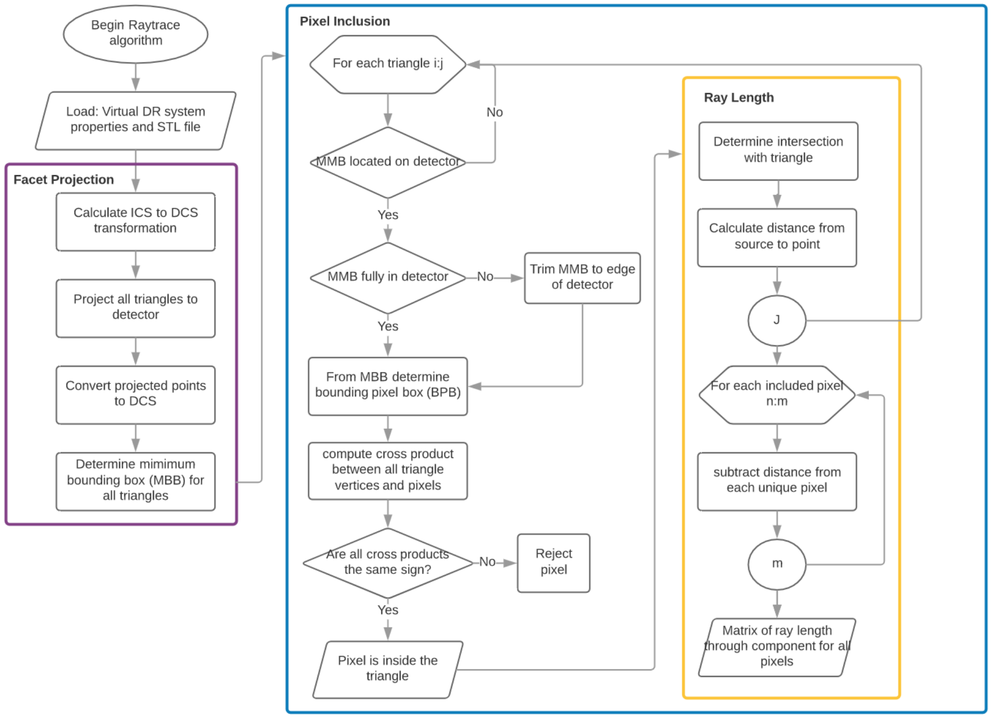

Figure 11 Ray Trace Pseudo Code Diagram

All calculations for converting information between the ICS and DCS and the projection of the triangles onto the DDA are done during the facet projection stage. First, the transformation between the ICS and the DCS is calculated based on distance between the source and detector as well as the DDA dimensions. This is further discussed in Appendix A – Coordinate Transformations and Conversions. Next, each triangle is projected onto the DDA plane through the use of similar triangles and the equation for a ray. Figure 12 illustrates the projection of a triangle to the DDA plane and ray equation, where **A** is the projected point, α is the similarity ratio, **V** is the vertex to be projected and **P** is the location of the source. Once projected, the vertices are then converted to the DCS coordinate system for the calculation of the included pixels. Since all of the vertices are stored in an N x 3 array, matrix operations can be used to rapidly project and convert all vertices simultaneously. Lastly, the xy-minimum bounding box (MMB) for each triangle is determined and stored in a matrix. The MMB is used during the pixel inclusion stage of the ray trace algorithm to quickly determine which pixels to use during back projection.

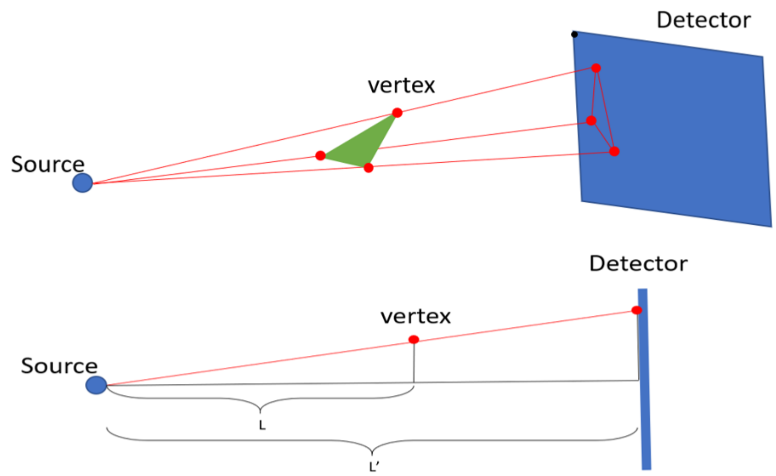

$$\mathbf{A} = (\alpha * \boldsymbol{V}) + P \qquad \alpha = \frac{L'}{L} = \frac{Source(X,0,0) - Detector(X,0,0)}{Source(X,0,0) - Vertex(X,0,0)}$$

Figure 12 Projection of Triangles to the DDA

The pixel inclusion stage is the most important step in the back projection algorithm. In this stage, the bounding boxes of each projected triangle are used to determine which pixels are utilized for ray tracing. Two potential issues arise from projecting the triangles onto the DDA, the triangle could either lay (1) partially or (2) entirely off of the DDA, as illustrated in Figure 13A. To account for this, two checks are put in place prior to inclusion determination. The first check tests whether the MMB is at least partially overlapping the DDA. If this is true, then the

MMB moves on to the next block of code; otherwise, it is discarded. Next, the MMB is either trimmed to fit within the DDA if it is partially overlapping, or, if the MMB is fully within the DDA, then the MMB moves on to the next block of code. Next, the bounding pixel box (BPB), the minimum grid of pixels that encloses the triangle, is determined from the MMB.

An example of a BPB can be seen in Figure 13B. This subtle yet imperative shift expedites the inclusion process by allowing pixels to be quickly indexed from the BPB. With the BPB defined, the selection of included pixels can begin. For each pixel in the BPB, the cross product for each triangle vertex is computed and compared, which is shown in Figure 14. For a given pixel, if all cross-products are of the same sign then the point must lie within the triangle. This process is carried out for all pixels simultaneously through the use of matrix operations, with the included pixels being passed onto the next stage of the algorithm to calculate the ray path length.

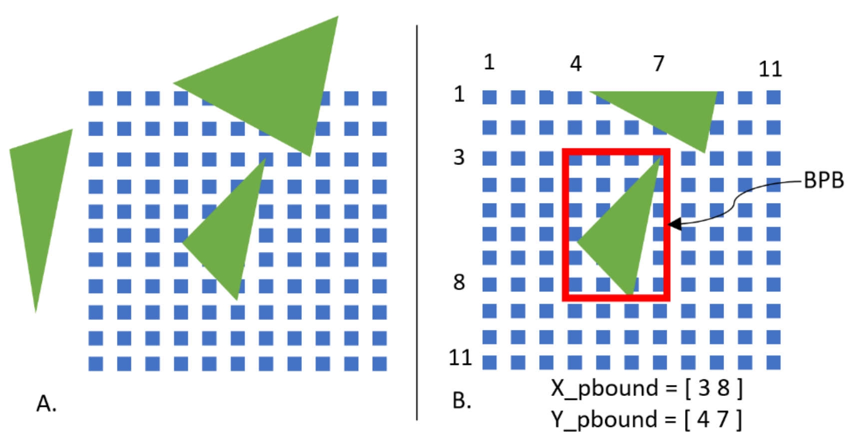

Figure 13 A. noncompliant triangles B. Determination of bounding pixel box

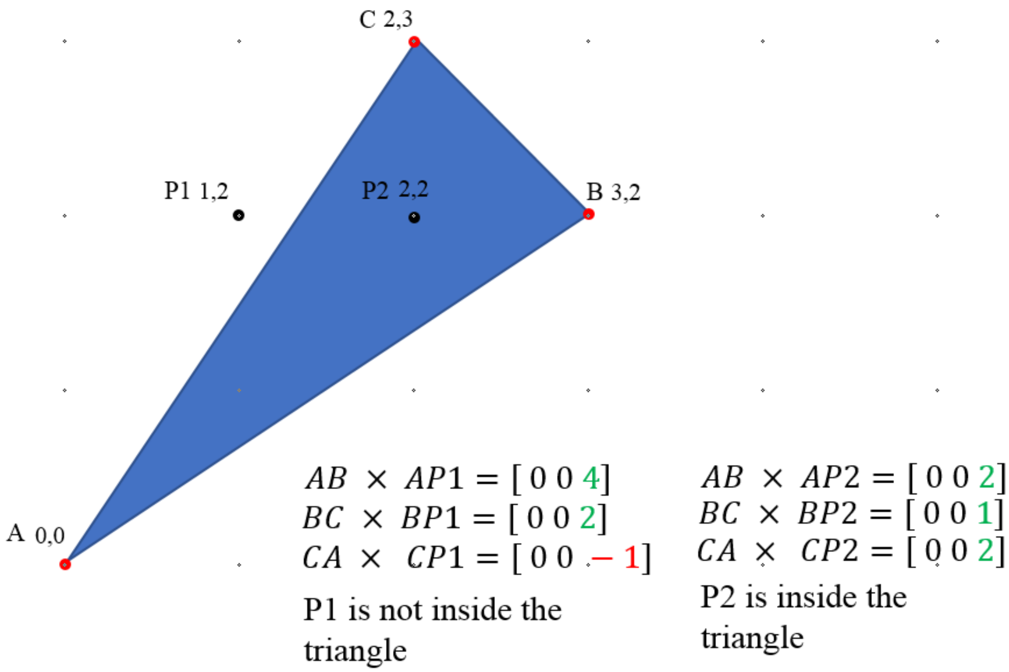

Figure 14 Examples of inclusion logics. If all cross products are the same sign then the point must lie inside the triangle

To determine the ray path length for a given pixel, the distance from the source to a given triangle must be calculated. By taking advantage of the fact that each triangle of an STL defines a plane, this process can be done quite efficiently. Equation 1 shows the equation for a plane that contains triangle ABC. The constants a, b, and c are the coordinates of the vector normal to ABC, as in Equation 2, and d, shown in Equation 3, states that **A** belongs to the triangle's plane.

In much the same way in which the triangles are projected onto the DDA, by scaling the vector that spans from the source to a given pixel to a plane, the intersection point with that triangle can be calculated. Equation 4 is the ray equation where $\mathbf{S_I}$ is the intersection coordinate,

β_p is the scaling value, and $\mathbf{S_p}$ is the pixel's coordinate. The expression for β_p can be derived by combining Equation 1 and Equation 3 as shown in Equation 5. Expressions for D and N are given in Equation 6 and Equation 7. Subscripts p and s denote pixel and source values, respectively. The distance from the source to a given intersection location L_i is the given by $\beta_p \|\boldsymbol{S_p}\|$ and saved to an M x 2 matrix where the first column is the intersection distance and the second column is the corresponding pixel.

$$ax + by + cz + d = 0 \qquad \text{Equation (1)}$$

$$\boldsymbol{n} = \boldsymbol{AB} \times \boldsymbol{AC} \qquad \text{Equation (2)}$$

$$d = -\boldsymbol{n} \cdot \boldsymbol{A} \qquad \text{Equation (3)}$$

$$\boldsymbol{SI} = \beta_p \boldsymbol{SP} \qquad \text{Equation (4)}$$

$$\beta_p = \frac{N}{(D - ax_p - by_p - cz_p)} \qquad \text{Equation (5)}$$

$$D = ax_s + by_s + cz_s \qquad \text{Equation (6)}$$

$$N = D + d \qquad \text{Equation (7)}$$

For the special cases where the pixel lies on a vertex or edge, the cross-product between the pixel and the vertex or edge will be zero. These pixels are saved in a separate matrix until all of the intersection calculations are made, and only the unique intersection points are carried over to the ray path length stage. As mentioned earlier, a given pixel has N_p*2 intersections with a STL. The total ray path length through the STL can then be calculated by sorting L_i from largest to smallest, subtracting every even index from the odd index, and summing the result, as seen in Equation 8. The maximum ray path length for a given orientation can be obtained by repeating this calculations for all pixels and finding the maximum value.

$$\sum_{i=1}^{N_p} (L_{2i} - L_{2i-1})$$ Equation (8)

4.2.3 Performance

The speed and robustness of a back projection algorithm is critical to its performance. Many applications for these algorithms involve either rendering or optimization which involve hundreds to thousands of function evaluations. If the algorithm is not written in an efficient manner, then the computational time becomes exceedingly long and depending on the application, may not be viable. Two different methodologies were used to increase the speed of the back projection algorithm: (1) matrix operations and (2) parallel processing. Matrix operations allow for a large number of calculations to be executed simultaneously. An example of this code is when the inclusiveness of each pixel is being determined. By containing all of the pixel coordinates in a single column matrix, the cross-products between all the pixels and their respective triangle vertices can be executed simultaneously. When compared to using a for-loop to calculate each cross product individually, using matrix operations to perform this calculation is significantly faster. In general the use of for-loops was avoided whenever possible due to their poor performance.

Parallel processing was also utilized to increase performance, by using multiple cores to execute the algorithm. Since the calculation of the triangles included pixels and therefore the ray path lengths for those pixels is independent from one another, a different triangle can be processed on each computing core.

Performance not only depends on the efficiency of the code but also the amount of calculations that is required. In this case the major contributors to increased data are the number of triangles in the STL and the number of pixels on the DDA. Analysis of performance was carried out on a four core i7-3610QM 2.3 GHz processor with 16 gigabits of RAM. Multiple spheres with increasingly more triangles was used to evaluate how the number of triangles affected computational run time. These spheres are depicted in Figure 15. A larger number of triangles results in more iterations of inclusion, reducing the algorithms performance.

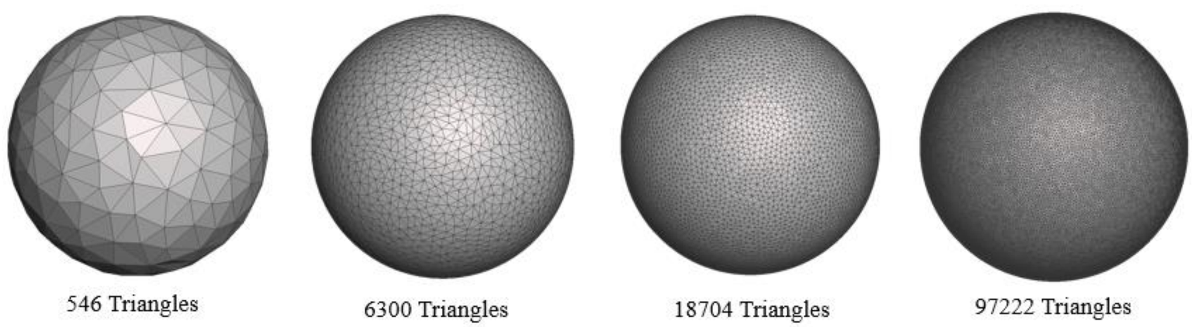

Figure 15 Spheres with increasing number of triangles

It should be noted that the size of the component does not affect run times because a larger component does not necessarily produce a STL file with more triangles. A more complex part, shown in Figure 16, was used analyze how the pixel width of the DDA effects computational time. Figure 17a shows how computation time changes with the number of triangles, clearly showing the trend that as the number of triangles increases, so does computation time. The number of pixels in the DDA also increases the run time of the algorithm for a similar reason; more pixels increases the number of calculations. Figure 17b shows that as the DDA’s width increased, so did the computation time.

48440 Triangles

Figure 16 Model used for DDA width analysis

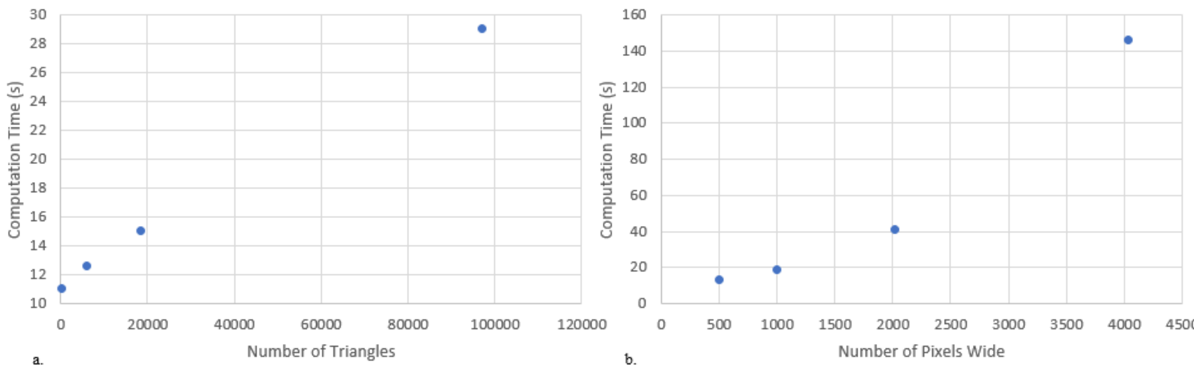

Figure 17 a. Computation time vs Number of Triangle, b. Computation Time vs DDA Width

The largest increase in computation time as the DDA width increases was attributed to the ray path length for-loop. With the current algorithm, several options exist to further increase its performance. The algorithm was written in MATLAB to capitalize on the extensive library and ease of use of the software. Though this expedited the development phase, MATLAB is inherently slow when comparted to C++ or Python. MATLAB converts its code to C++ during execution; so, removing this step would increase the performance of the algorithm. Also, this analysis was carried out with only four cores; access to more processors would further increase performance by allowing more triangles to be processed simultaneously. The most promising performance boost could come from multi-core processing on GPUs. GPUs have hundreds to thousands of cores that allow for massive parallelization of the algorithm.

4.3 Orientation Optimization

With a method for rapidly calculating the radiographic thickness of a component in a specific orientation, the search for an optimal orientation can proceed. Rather than testing the entire design space, a search method that selects new orientations intelligently will produce an optimal solution faster than brute force methods. Furthermore, gradient-based optimization is insufficient for this problem due to its multi-modal and non-differentiable behavior. Non-gradient based methods such as genetic algorithms can handle these characteristics and are well suited for optimization of this type of problem.

4.3.1 Applications of Genetic Algorithms

Genetic Algorithms (GA) are part of a much larger category of algorithms called Evolutionary Algorithms (EA) that mimic natural selection through a "survival of the fittest" mentality to solve nonlinear, non-differentiable, multimodal functions [40]. These strategies have shown great success in solving continuous parameter and high dimensionality optimization problems, mostly due to their ability to avoid local minima. Several different EA methodologies have been presented over the years. Voigt [41] describes a new scaling rule for multiple mutation GAs based on soft genetic operators call the Evolutionary Algorithm with Soft operators (EASY). By shifting the selection process to a stochastic approach, EASY was able to achieve sustained convergence through all generations for a range of multi-dimensional testbed functions. A EA written by Storn et al. [42] has been shown to be an efficient and simple method for nonlinear optimization and reported faster convergence times than EASY. To do this, Storn's et al.'s EA uses N-dimensional vectors to describe a population P for each generation G, where each N dimensional vector defines set parameters for the cost function. The initial population is produced randomly from a uniform probably distribution covering the entire feasible region. For each initial vector, the cost function is evaluated and ranked using the "greedy criteria". A vector with a lower cost function value is said to be more fit and will out rank a vector of higher outcome. New vectors are created through parameters mixing or crossover between two parent vectors in the current. If a new vector has a smaller cost function value a one of its parents, then it replaces that parent in the next generation. This process continues until the algorithm meets a convergence criterion or has evaluated all generations. Due to this strategy and the simplicity of the algorithm, SMART DR's optimization scheme was adapted for this work.

4.3.2 Genetic Algorithm Logic

SMART DR uses a Genetic Algorithm (GA) to minimize a component's maximum thickness as seen by the X-ray source. Specifically, a discrete two-dimensional differential evolution (DE) scheme is used to minimize the back projection (BP) algorithm function in the form:

$$minimize\ BP(x_1, x_2) \qquad \text{Equation (9)}$$

$$subject\ to - 90 \leq x_1 \leq 90\ \& - 180 \leq x_2 \leq 180$$

where x_1 and x_2 are the angle of rotation about the y and z axes. A flow chart for the optimization can been found in Figure 18. The inputs to the algorithm are the rotation bounds, the number of generations, the survival rate, and the mutation rate. The survival rate is the percentage of the top individuals in the current generation that are retained for the next generation. These individuals are also used during the crossover stage because they have the lowest current fitness value. Mutation rate defines the likelihood of an individual mutating.

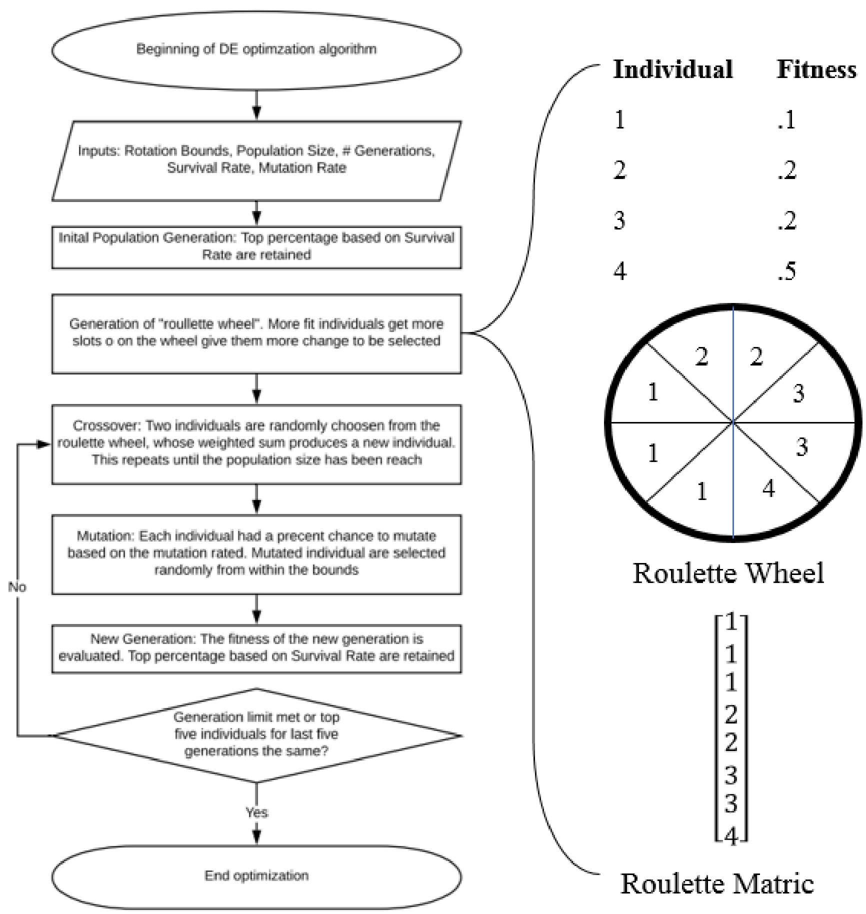

Figure 18 DE Optimization Pseudo Code

The initial population is generated from evenly distributed values across the optimization bounds. Each individual's fitness is evaluated, and the top percentage defined by the survival rate is retained. The next stage generates a virtual "roulette wheel" that gives individuals with better fitness values more slots on the wheel, which translates to more indexes in the roulette matrix. The reason for this approach is that more weight is given to better performing individuals, increasing the likelihood in their selection for crossover.

From this roulette matrix, two indexes are randomly selected, and the two corresponding individuals are then used during crossover. Two random weights are generated and used in two separate weighted averages of the two parents, creating two new children. This cycle continues until the population has reached its maximum value. Each individual is then passed through the mutation stage where it is assigned a random value between zero and one. If this value is higher than the mutation rate then a random new individual replaces the current one.

At this point a new generation has been established. The parameter values and their fitness values are saved, and the whole process begins over again. Optimization continues until all generations have been evaluated or the top five individuals for the last five generations are the same. Once the convergence criteria has been met, the fittest individual of the current generation is considered to be the optimal solution and is used as the orientation for inspection.

4.3.3 Second Orientation

During the optimization process, a second orientation is also calculated that, when combined with the initial optimal orientation, can be used to determine the morphology, size, and three-dimensional location of a flaw. An optimal second orientation from a flaw characteristic perspective would be a 90 degree rotation along either the Y or Z axis from the initial optimal orientation, producing two orthogonal views of a flaw. All of the information pertaining to a flaw’s size, location, and morphology can easily be obtained from these two orientations due to their orthogonality. Limitations of the DR system being used or of the component being inspected may make a 90 degree rotation impractical or impossible. To account for this, SMART DR uses a classical golden search algorithm and flaw detectability data, described in the next chapter, to determine the closest angle of rotation that can be achieved and still allow a flaw size of interest to be detectable.

Chapter 5 Predicting Radiographic Image Quality

5.1 Image Quality Predication

An important part of SMART DR is its ability to predict the image quality, or more specifically, the detectability of a flaw size of interest for high energy (≥ 1 Mev) DR systems. This prediction serves as a "go/no go" metric for the inspectability of a component by informing the user, if given an optimal orientation, the component can be inspected with the DR system in question. To achieve this, SMART DR combines component thickness information from the ray trace portion of the applications and two image quality metrics, Contrast to Noise Ratio (CNR) and Normalized Image Unsharpness (U_{IM}) which represent radiographic contrast and definition to create a Probability of Detection (POD) for flaws diameters of interest. The POD estimates the probability of detecting a given flaw over the imaged section of the component. Since image quality measurements for DR are typically done in-situ and are qualitative in nature, very little has been published on image quality for high energy DR systems. The contents of this chapter discuss the experimental set up used to obtain high energy DR image data, how CNR and U_{IM} relate to image quality and their calculation, and how they combine to produce the POD for flaw diameters of interest.

5.2 Experiment

Due to the lack of information in the literature on high energy DR, an experiment was conducted to establish a relationship between x-ray energy, component thickness, and the minimum detectable flaw size (F_{min}). Mr. Griffin Jones of the Applied Research Laboratory a Level 3 radiography inspector assisted in the design of the evaluation and the analysis of the results. The evaluation entailed varying the energy of the x-ray source and component thickness over the ranges provided in Table 2. The radiographic contrast and definition were analyzed for the range of flaw types defined in Table 3. The specific set of flaws that were selected based on SMART DR's focus on aerospace applications, and test geometries containing the flaws were made from titanium six percent aluminum and four percent vanadium (Ti-6Al-4V) alloy. Eight test geometries consisting of 76.2 mm (3 in.) square blocks of Ti-6Al-4V that varied from 25.4 mm to 76.2 mm (1 to 8 in.) in thickness were purchased. Each block had 15 artificial flaws that varied from one, two, and four percent total thickness, which are a specific subset of the range of flaws in Table 2. An example of a 50.8 mm (2 in.) thick block and its artificial flaws is illustrated in Figure 19.

Table 2 Experimental Variables Levels

Energy(Mev)	0.45	3	4	6	8	12		
Component Thickness(mm)	25.4	50.8	76.2	101.6	127	152.4	177.8	203.2

Table 3 Artificial Flaw Geometries

Diameter (mm)	0.41	0.79	1.194	1.600	1.981	2.387	2.77	3.175	3.581	3.962
Percent Thickness (%)	1	2	4							

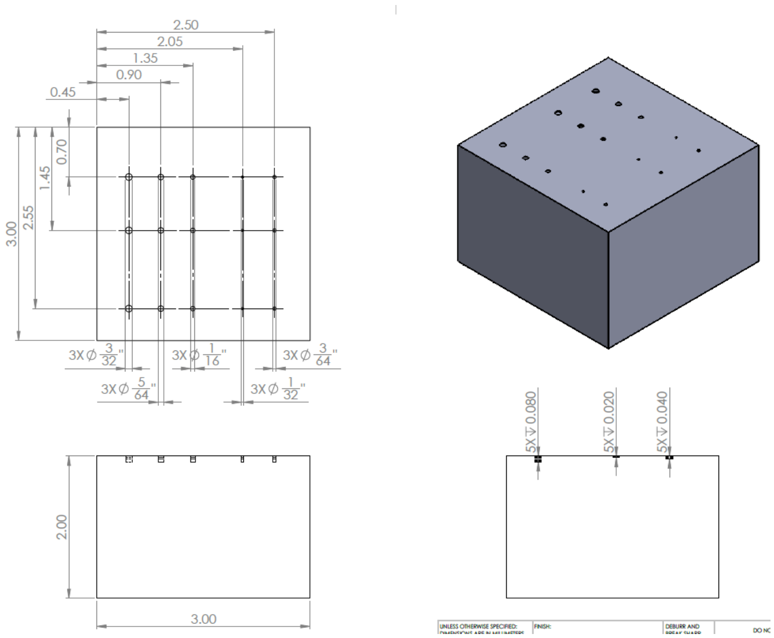

Figure 19 Example of a 50.8 mm (2 in.) thick Ti-6Al-4V block

A detailed table of the flaw sizes for all block types can be found in Appendix B – Ti-6Al-4V Experimental Blocks. The specific set of flaw sizes and depths for each block where chosen to mimic hole type Image Quality Indicators (IQIs) that are typically used to determine acceptable image quality levels and to test the extreme limits of radiographic definition and contrast.

The experiment was conducted at the Idaho Accelerator Center (IAC), University of Idaho in Pocatello, ID using their Yxlon Y.TU450-D10 450 Kev source and custom linear accelerator (linac) with an energy range of 1 to 12 Mev. A GE DXR250U-W DDA was used for image capturing. The major advantage of this site was the use of their variable power linac which allowed for energies ranging from 1 Mev to 12 Mev to be tested easily within the same set up. Due to limitations of the linac system, only certain energy bands are stable enough for radiographic imaging, limiting this experiment to the energies of 3, 4, 6, 8, and 12 Mev. Important parameters for the 450 Kev system, linac, and DDA are given in Table 4.

For a given energy level, starting with the 25.4 mm (1 in.) block, each block was imaged in the middle of and directly against the DDA. The source to detector distance was 1219.2 mm (48 in.) for 25.4 mm to 101.6 mm (1 to 4 in.) blocks, and 1524 mm (60 in.), for the 127 mm to 203.3 mm (5 to 8 in.) blocks. Figure 20 is a photograph showing the experiment set up and the lead blocks placed around the test block to reduce edge affects and noise. The blocks were positioned so that the artificial flaws were facing the source. The exposure time and number of integrations were modulated until a radiograph was obtained that utilized the full energy band of the DDA. This was carried out for all blocks over all energy levels. An example radiograph of the 50.8 mm (2 in.) test block at 450 Kev is show in Figure 21. The radiographs for each energy level and thickness, totaling 26 radiographs, can be found in Appendix C – Experiment Radiographs. These radiographs were then analyzed to determine the effects of energy and component thickness on radiographic contrast and definition.

Table 4 450 Kev system, linac, and DDA paramters

X-ray source	Energy(Mev)	Spot size(mm)
Y.TU450-D10	.450	2.5
Linac	1-12	variable
DDA	Pitch(µm)	SR_b (mm)
GE DXR250U-W	200	.249

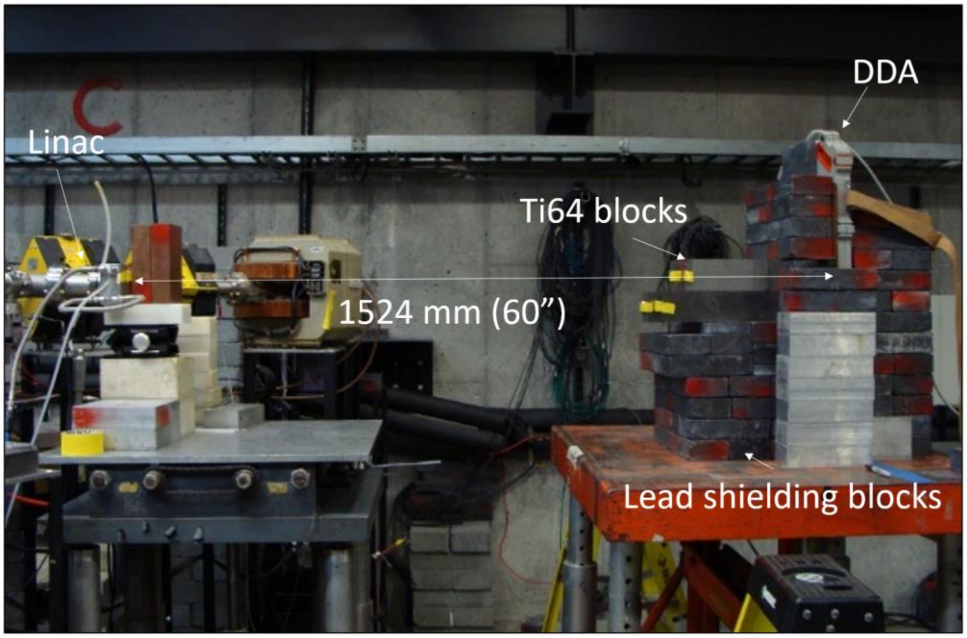

Figure 20 Experiment set up for Image quality experiment

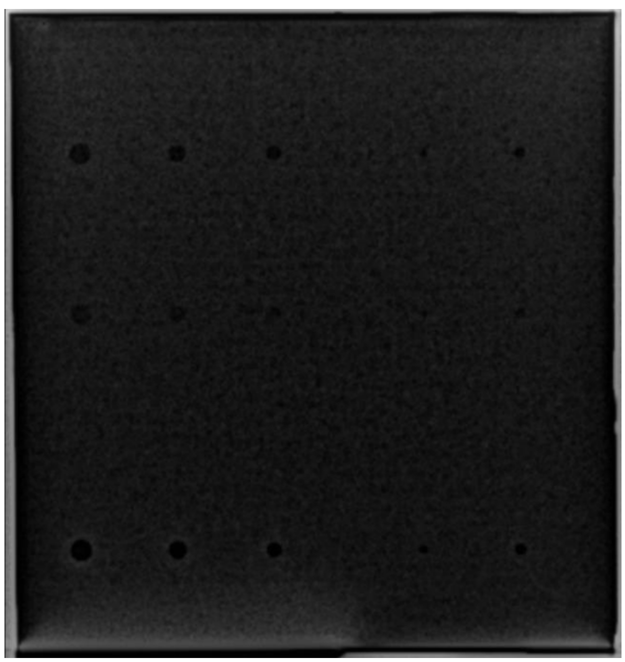

Figure 21 Radiograph sample of the 50.8 mm (2 in.) test block at 450 Kev

5.3 Contrast

Radiographic contrast is defined as the difference in grayscale intensity between two different regions of interest [32] and consists of subject and DDA contrast. Subject contrast is due to variations in thickness or material within the component being imaged. In this way, subject contrast can be thought of as a measure of the smallest discernable change in thicknesses that can be perceived on a radiograph.

DDA contrast refers to the smallest difference in x-ray energy between two pixels that the DDA can detect and is affected by a wide variety of DDA characteristics that do not pertain to this work. Without the proper level of radiographic contrast, edges and changes in thicknesses become difficult to see even if they are above the systems definition limit. An example of this can be seen in the radiograph of a step block Figure 22. As the thicknesses of the step block increases, the contrast is reduced, and the edges of the flaws become less clear.

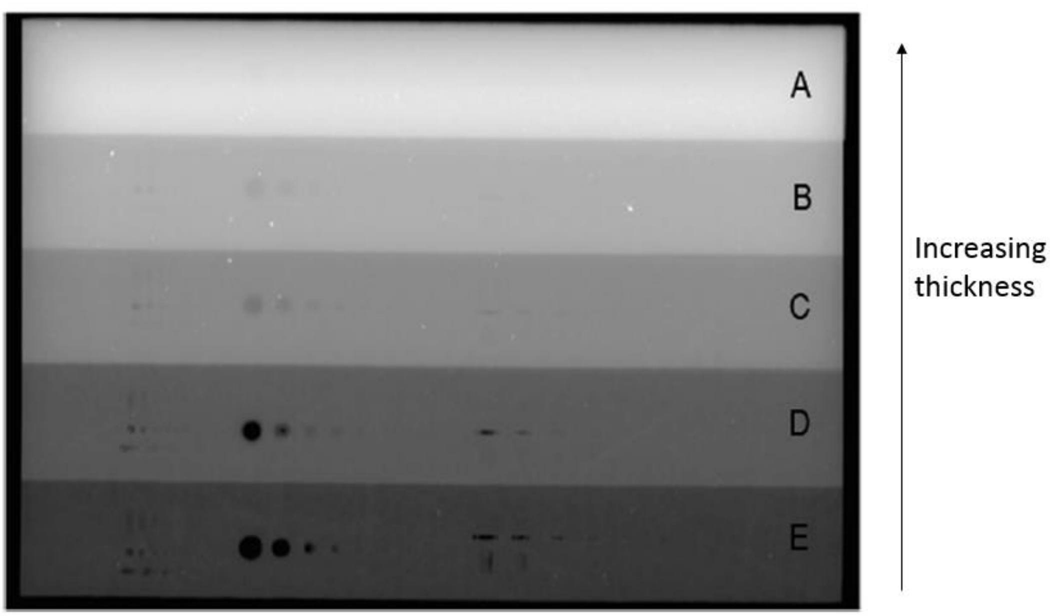

Figure 22 Example of different levels of contrast due to thickness changes in a step block [31]

5.3.1 Contrast to Noise Ratio

Several different metrics have been developed to quantify the contrast level of a radiograph. ASTM standard E2597 [43] defines one such a metric called the Contrast-to-Noise Ratio (CNR), which quantifies the difference between the contrast and relative noise of a feature. To calculate the CNR of a feature, the signal (mean grayscale value) and noise (standard deviation, STDEV) are calculated for the three areas as shown in Figure 23.

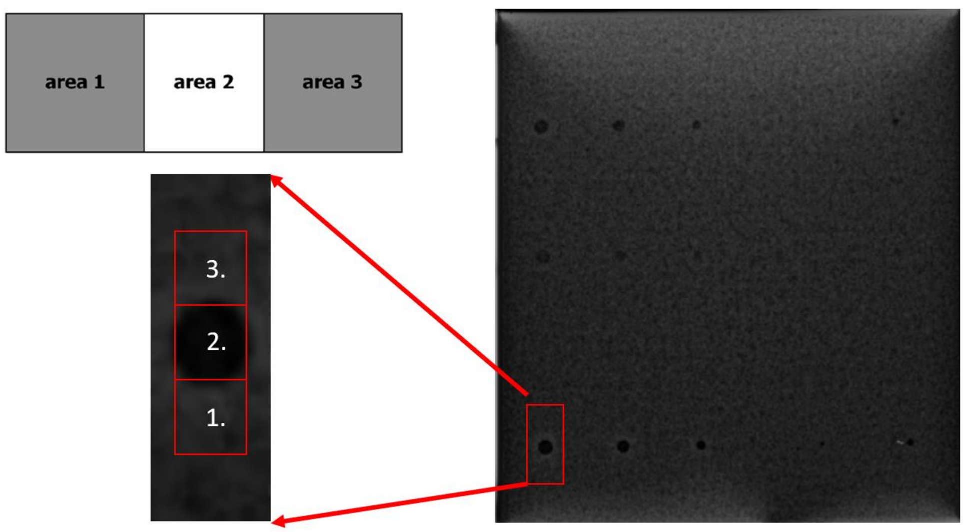

Figure 23 CNR sampling method [43]

Areas 1 and 3 correspond to bulk areas directly adjacent to the AOI, and Area 2 is the AOI itself. In this experiment, grayscale measurements for Area 2 were taken from the center of the artificial flaws, and Areas 1 and 3 were from the surrounding area. Sampling was done vertically instead of horizontally to remove striated artifacts produced by the linac. The sampled grayscale values along with Equation 8 are then used to calculate the AOI's CNR. The signal is the average grayscale value of each area.

$$CNR = \frac{0.5 \times \left(signal(area\ 1) + signal(area\ 3)\right) - signal(area\ 2)}{0.5 \times (noise(area\ 1) + noise(area\ 3))} \qquad \text{Equation (8)}$$

The noise is the median STDEV and is found by taking the STDEV of each column pixel in the sample area and finding the median value. A detailed example of the CNR calculations for the flaw shown in Figure 23 is given in Table 5.

Table 5 Detailed CNR calculations for the 25.4 (1 in.) block with 2.38 mm (3/32") flaw diameter that is 4% of the total thickness

	AREA ONE GRAYSCALE VALUES							Average(SIGNAL)
	6808	6842	6868	6876	6883	6909	6945	6853
	6787	6838	6860	6867	6885	6910	6942	
	6800	6820	6847	6873	6882	6915	6942	
	6783	6806	6837	6879	6895	6906	6931	
	6763	6803	6815	6840	6868	6907	6906	
	6762	6789	6802	6828	6874	6887	6884	
	6740	6765	6798	6820	6851	6873	6872	
								Median STD (NOIS
Column ST	23.85272	27.17842	27.90972	24.70974	14.22941	15.17674	30.17647	25
	AREA TWO GRAYSCALE VALUES							Average(SIGNAL)
	6847	6911	6936	6972	6977	6988	6966	6931
	6883	6909	6942	6961	6965	6993	7006	
	6870	6913	6947	6953	6960	6984	6991	
	6856	6880	6915	6948	6969	6967	6971	
	6849	6888	6918	6950	6948	6967	6974	
	6831	6876	6897	6911	6938	6954	6990	
	6842	6867	6888	6906	6915	6943	6969	
	AREA THREE GRAYSCALE VALUES							Average(SIGNAL)
	6465	6510	6517	6521	6551	6575	6596	6488
	6442	6471	6501	6511	6534	6548	6582	
	6442	6468	6494	6505	6518	6533	6566	
	6429	6456	6469	6488	6517	6520	6557	
	6406	6431	6448	6480	6515	6514	6543	
	6393	6413	6437	6468	6488	6498	6518	
	6385	6407	6425	6437	6463	6480	6494	
								Median STD (NOIS
Column ST	29.31114	36.45741	34.98775	28.77168	29.0156	31.58586	35.70447	32
								CNR Value
								9.24

The CNR for all 15 artificial flaws for all 26 radiographs were sampled and measured nine times to improve the accuracy of the measurements. By analyzing this CNR data, a method for quantifying the effects of source energy and component thickness was created.

5.3.2 Data Analysis

Based on the CNR data from the experiment, a cumulative distribution function (CDF) was created for each energy, component thickness, flaw depth, and flaw diameter combination. The CDF defines what percentage of the sampled data is at or above a certain CNR value. Figure 24 is an example CDF for the flaw used in Table 5.

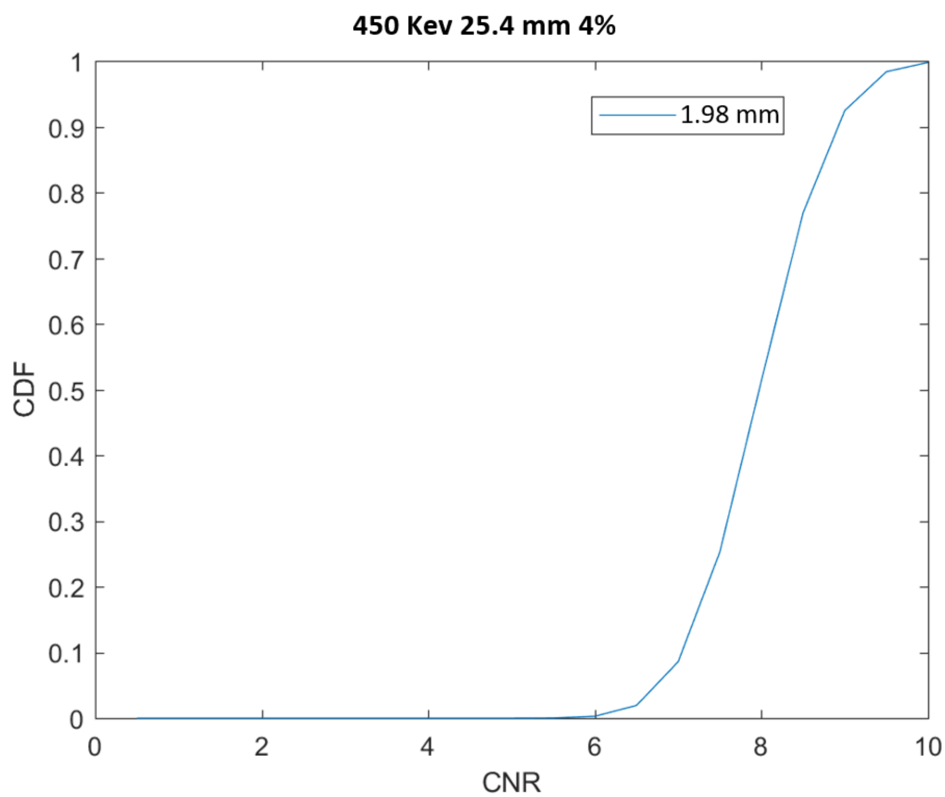

Figure 24 Example CDF for a 2.38 mm (0.78 in.) diameter flaw that is 1.016 mm (0.04 in.) deep in a 25.4 (1 in.) block imaged at 450 Kev.

As stated in Section 10.19.3.2 of ASTM standard E2698 [43], the CNR across a hole-type IQI must be at least 2.5 for the DR system to be considered sufficient for inspecting the given geometry. This value provides a cut-off value below which a feature is no longer able to be accurately detected. The CDFs allow for the percentage of the sampled data at or below 2.5 to be quantified. The likelihood of a flaw having a CNR higher than 2.5 is then one minus the CDF value. For example, if a value of the POD at a CNR of 2.5 is 100, as it is in Figure 25, then there is a 100 percent possibility of detecting this flaw, but if the POD is below 100, then this value is the probably of detecting that flaw. The remainder of this section explains the creation of the CDF plots and their conversation to POD plots.

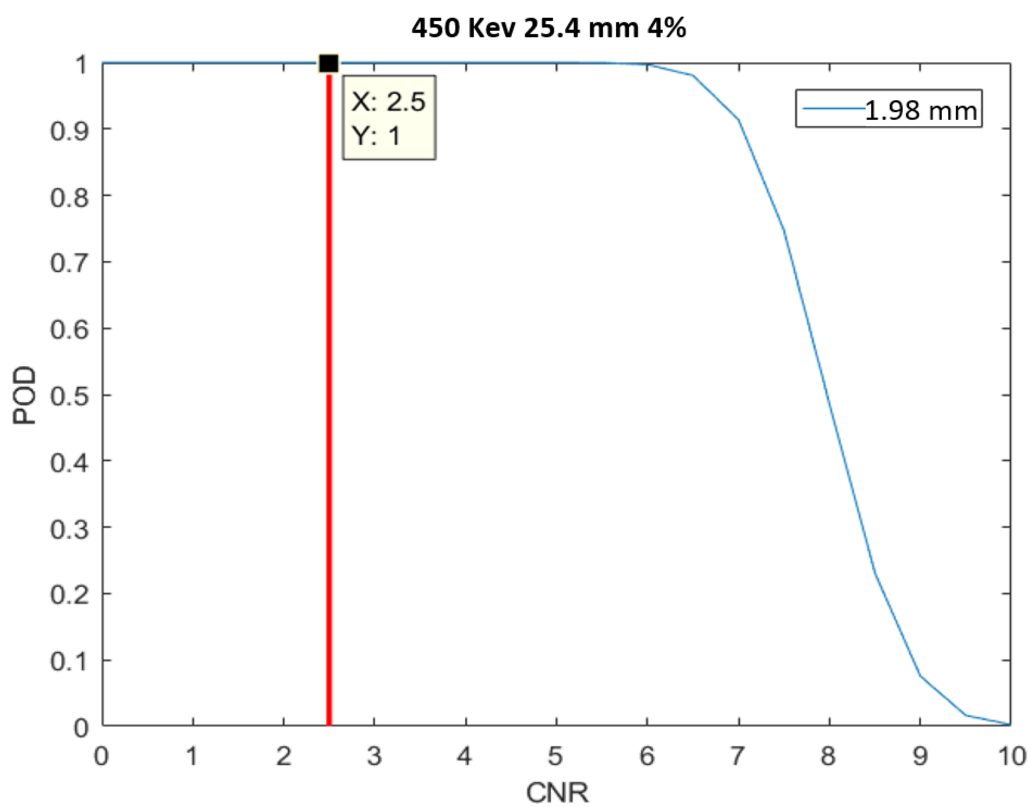

Figure 25 Probability of detection of 1.98 mm (0.078 in.) flaw

Data analysis was conducted using MATLAB due to the availability of many built in analysis tools. By using the fitdist and cdf commands, a PDF could be fit to the CNR data from each experimental case and then be converted to a CDF. The benefit of fitting the data to a PDF is that the resulting CDF is a continuous function as opposed to the discrete function that is produced when directly using the data. To verify that the data was normally distributed, CDF were created without fitting the data then compared to the fitted CDF by use of the R^2 values. First, histograms (see Figure 26a) of the CNR values for each combination where created with bins 0.5 CNR wide. The number of instances in each bin where then divided by the total number of data points, nine, to produce a PDF. As seen in Figure 26b, when visually comparing the manually generated PDF with a fitted PDF, the two sets of data are in good agreement.

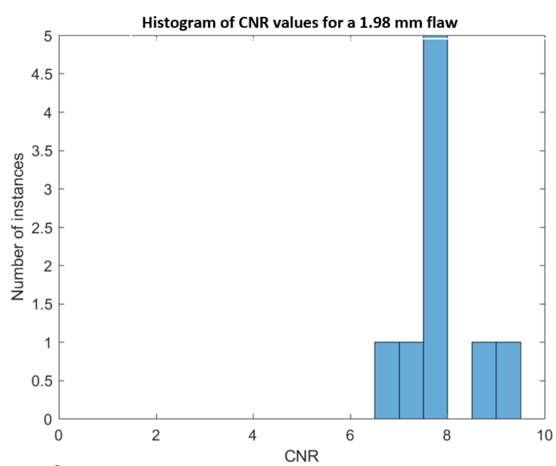

a.

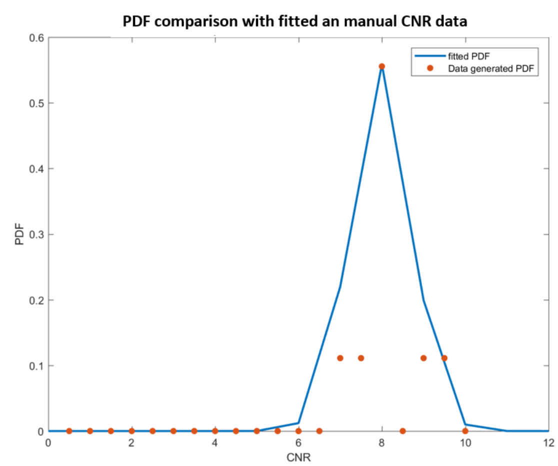

b.

Figure 26 a. Histogram of CNR values for the 2.38 mm (3/32”) flaw used in Section 5.3.1, b. comparison of fitted PDF with manually generated PDF.

Of more concern is how well the CDF of this data aligns with a fitted CDF. Figure 27 shows the comparison between the fitted and manually generated CDF curves; the manually generated CDF has a R^2 value of 0.975. This high level of agreement provides confidence that the data is normally distributed and can be analyzed as such.

Repeating this process for all flaw diameters on the 25.4 mm (1 in.) block, the final POD curves can be seen in Figure 28. From this graph it can be observed that a 0.41 mm (0.016 in.) flaw has a 42% chance of being detected, and larger flaws have a near 100% chance of detection The goal of creating these POD curves that cover a wide range of energies, component thicknesses, and flaw types is that they may can be applied to a wide range of DR systems and applications. All POD curves for contrast can be found in Appendix D – Probability of Detection. Contrast is not the only measure of radiographic image quality. Definition also restricts the detection limits of a radiograph, and the incorporation of a metric for radiographic definition into the POD curves is discussed in the next sections.

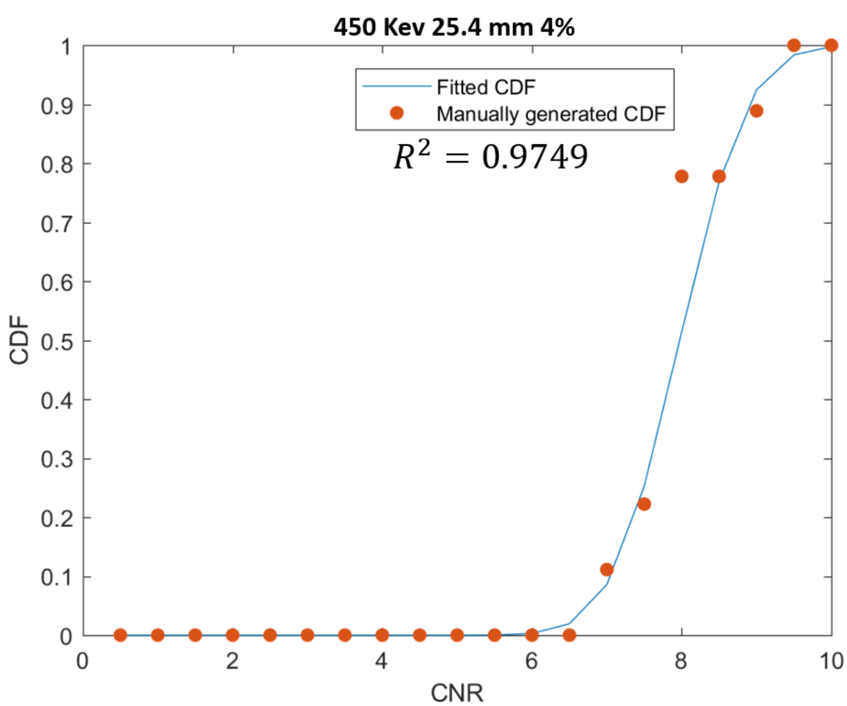

Figure 27 Comparison of fitted and manually generated CDF

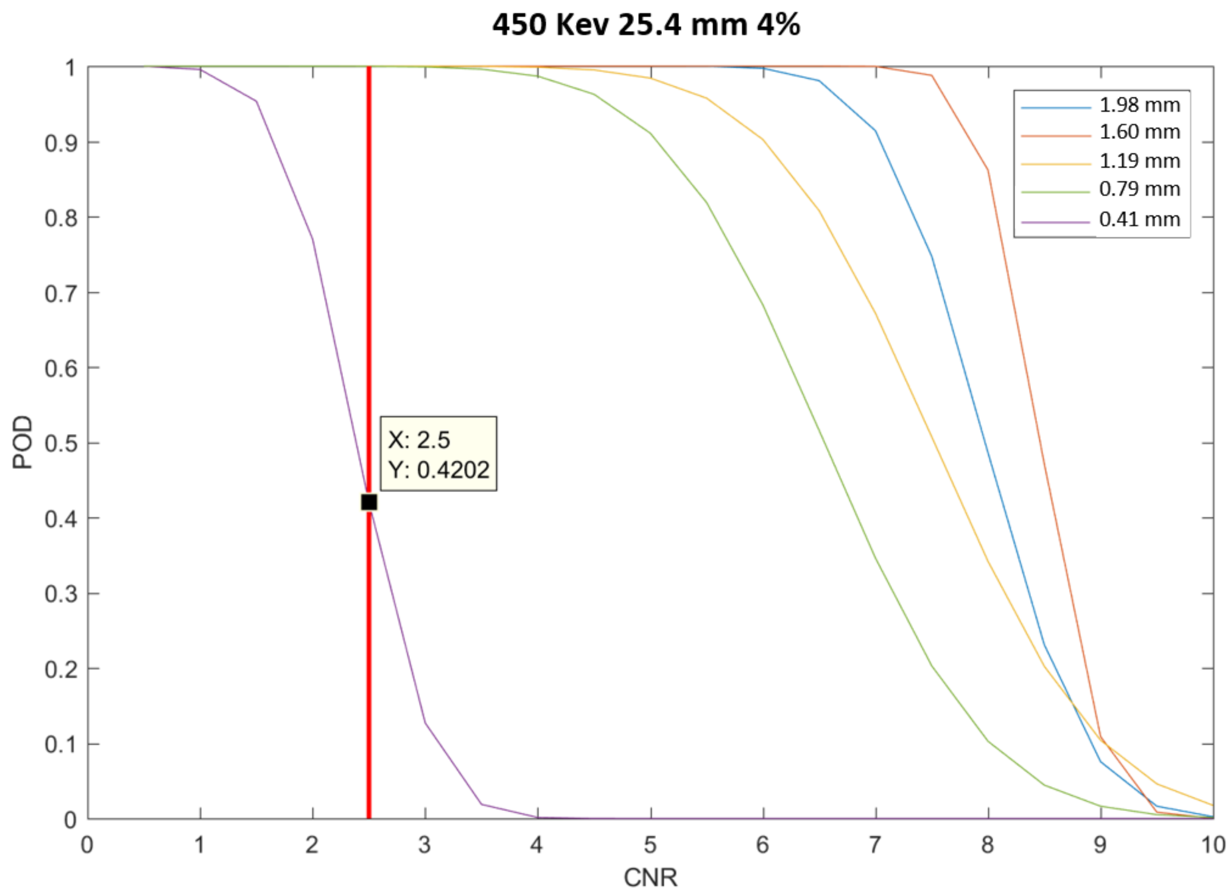

Figure 28 Final POD curve for all flaw diameters with 1 mm (0.04 in.) depth for a 25.4 mm (1 in.) block at 450 Kev. POD of a 0.41 mm (0.016 in.) diameter flaw is 42%

5.4 Normalized Image Unsharpness

Radiographic definition refers to how sharp an image is in both edge quality and small feature resolution and is comprised of inherent and geometric unsharpness [32]. Inherent unsharpness is attributed to the resolution of the DDA, mainly the pixel size. A smaller pixel size allows for finer details to be captured in the radiograph, increasing its sharpness. Geometric unsharpness is due to the DR system's focal spot size and magnification. Both of these effects create an overlapping of projections called the penumbra that blur edges and fine details. If the radiographic definition is not high enough then small features will not be resolved, and potential critical defects could be missed. Figure 29 shows an example of a how definition affects edge clarity. Figure 29a has reduced definition when compared to Figure 29b. Due to this the features in the imaged component are blurred.

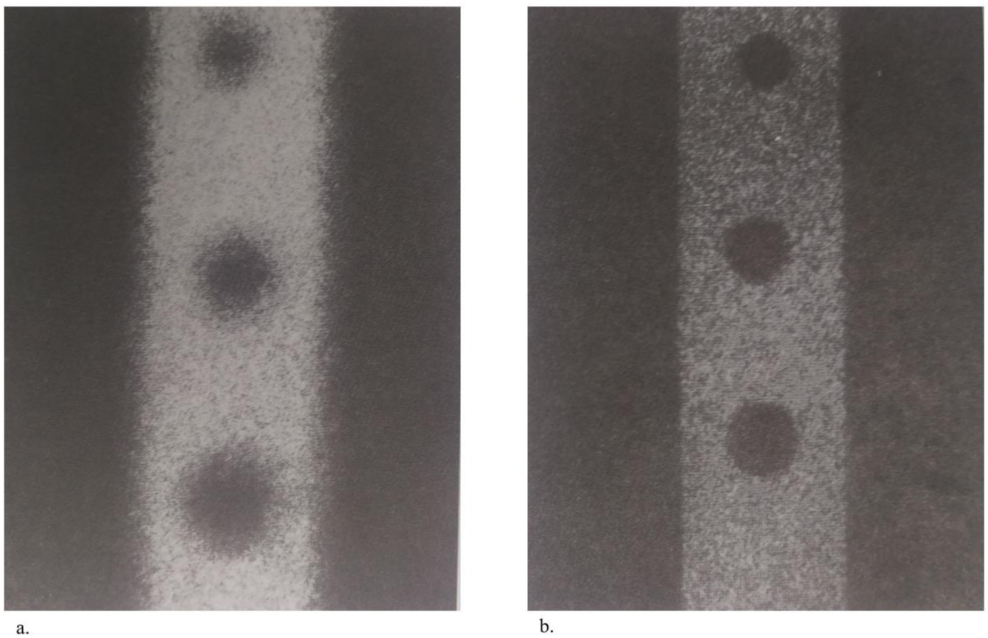

Figure 29 example of how different levels of definition affect edge clarity [9]

5.4.1 Normalized Image Unsharpness

The multi-faceted nature of radiographic definition mandates that any metric used to describe it must take into account many different characteristics. To this point, the normalized image unsharpness metric, as described in ASTM standard 2698 [44] will be used to quantify radiographic definition. Normalized image unsharpness (U_{im}), defined in Equation 9, takes into account inherent unsharpness through the DDA Basic Spatial Resolution (SR_b), which defines the resolution limit of the DDA used, and geometrical unsharpness through the magnification (υ) and the geometric image unsharpness (U_g) terms.

$$U_{im} = \frac{1}{\vartheta} * \sqrt[3]{U_g^3 + (1.6 * SR_b)^3} \qquad \text{Equation (10)}$$

Through the combination of all of these terms, U_{im} defines the smallest imageable feature for a DR system in millimeters. The geometric image unsharpness, U_g is defined in Section 3.1.2 by Equation 1. All of the parameters required to calculate U_{im} are easily known or obtainable for a DR system. The amount of magnification is simply the distance from the component to the DDA divided by the source distance. The DDA used during the experiments had a SR_b of 0.249 mm and was determined using a duplex wire gauge as described in ASTM E 2002 [35]. U_g is composed of the magnification υ and focal spot size φ. For high energy DR systems with a specific energy level, the focal spot size is given by the manufacturer. The variable energy nature of the x-ray source used during the experiment allowed for different energies to be easily used, but focal spot size was not available. Therefore, the focal spot size for the linac had to be calculated from the radiographs taken during the experiment.

5.4.2 Focal Spot Calculations

To calculate the focal spot, the equation for geometric unsharpness was rearranged to solve for the spot size as seen in Equation 10. The magnification is easily known from the radiographic set up by dividing the thickness of the block by the working distance of the DR system. To determine the geometric unsharpness, the apparent diameter of the 11th flaw of every block was measured on each radiograph; this flaw represented both the largest diameter and deepest flaw on each block. Figure 30 shows the location of the 11th flaw on the 152.4 mm (6 in.) block imaged at 3 Mev.

$$\varphi = \frac{\mathrm{U_g}}{(\vartheta - 1)} \qquad \text{Equation (11)}$$

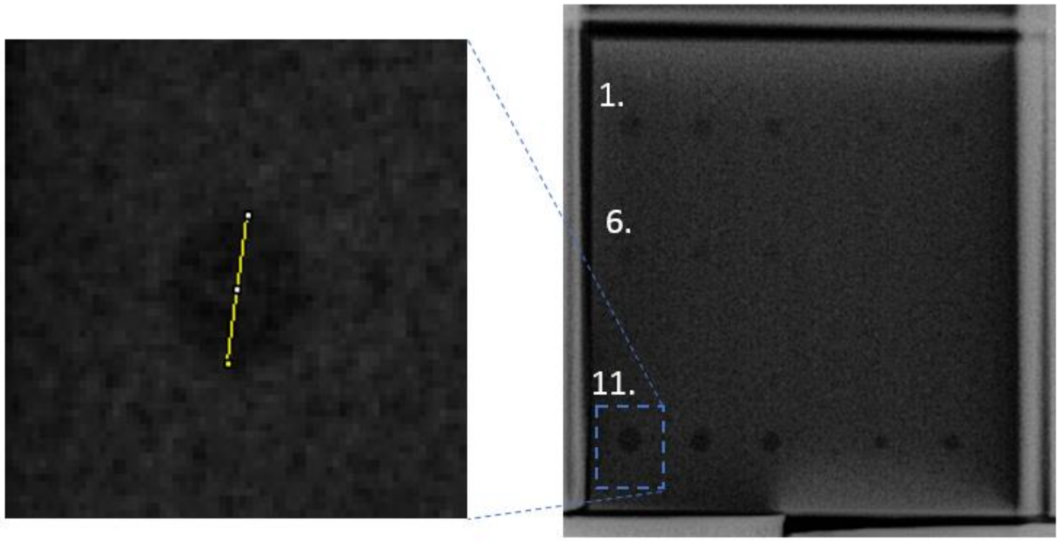

Figure 30 152.4 mm (6 in.) block imaged at 3 Mev displaying 11th flaw

These measurements are not the true diameter of the flaw but a composite of the nominal diameter plus magnification and focal spot effects. Figure 31 shows how these properties affect the diameter of the imaged flaw and the procedure used to calculate U_g from the imaged diameter measurement.

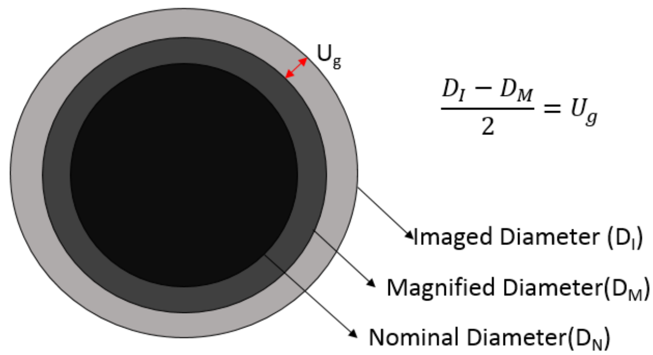

Figure 31 Calculation of U_g

For each parameter combination, the 11th hole was measured five times, and the average of these measurements was taken as the imaged diameter of the holes. To calculate U_g, the imaged diameter is subtracted from the magnified diameter and divided by two. This value along with the magnification were inserted into Equation 10 to solve for the focal spot size. For each energy level, the focal spot size was calculated for each thickness that was imaged and averaged to create the final mean focal spot size. The calculations for 3 Mev are shown in Table 6. Focal spot sizes for all the energy levels along with U_{im} values are given in Table 7. By combining U_{im} and CNR, a complete description of a DR systems image quality can be achieved.

Table 6 Mean focal spot size calculations for 3 Mev

MeV	Block Thickness (mm)	t, distance from source side of hole to detector plane (mm)	Nominal Diameter of #11 hole (in.)	Nominal Diameter of #11 hole (mm)	Radius of Measured Hole less Expected Radius of Hole = U_g = x_r (mm)	ϕ_c, Calculated Focal Spot size (mm)	Pooled Mean Focal Spot Size, X_ϕ (mm)
3	50.8	51	0.078	1.98	0.29	6.67	2.26
3	76.2	76	0.109	2.78	0.14	2.05	
3	101.6	102	0.109	2.78	0.19	2.14	
3	127	127	0.125	3.18	0.10	1.08	
3	152.4	152	0.141	3.57	-0.07	-0.62	

Table 7 Focal spot sizes and U_{im} Values

MeV	Block Thickness (mm)	Pooled Mean Focal Spot Size, X_ϕ (mm)	Pooled Mean Focal Spot Size Standard Deviation, S_ϕ (mm)
3	50.8	2.26	2.80
3	76.2		
3	101.6		
3	127		
3	152.4		
4	76.2	1.38	2.07
4	101.6		
4	127		
4	152.4		
4	177.8		
6	101.6	0.87	1.51
6	127		
6	152.4		
6	177.8		
6	203.2		
8	127	1.25	1.26
8	152.4		
8	177.8		
8	203.2		
12	152.4	1.66	1.06
12	177.8		
12	203.2		

5.5 Probability of Detection Metric

It was important when developing a method to predict image quality that it was not specific to a single DR system but adaptable to any DR system. Determining image quality through CNR and U_{im} allowed for this method to have a wide range of applicability. The CNR data covers the range of energies, thicknesses, and flaw types that are of interest for large AM build volumes, and U_{im} can be calculated for an individual DR system. As long as the user can provide the energy, focal spot size, and SR_b of the DR system to be used along with a STL of the component, the probability of detection (POD) for a flaw can be calculated. To combine both radiographic contrast and definition, the different flaw sizes used in the POD curves are normalized by the U_{im} of the DR system to be used, which is illustrated in Figure 32.

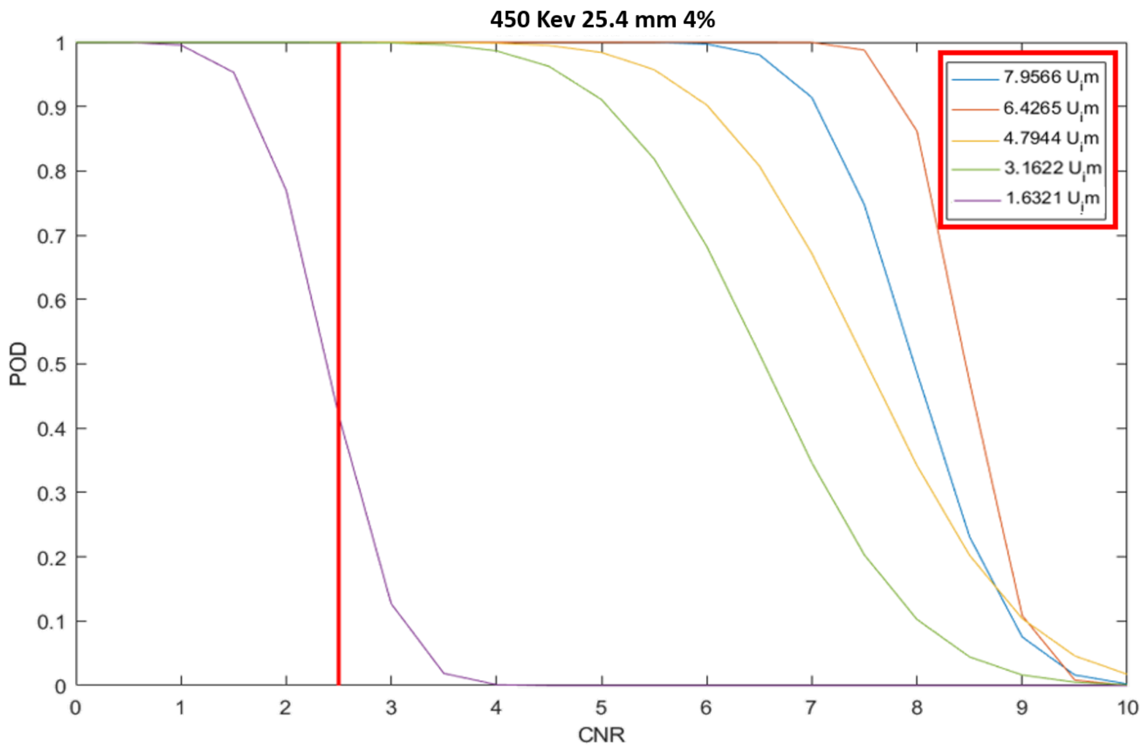

U_im	1.63	3.16	4.79	6.42	7.95
POD	42.02%	99.98%	100.00%	100.00%	100.00%

Figure 32 Normalized flaw sizes

For a flaw to have a non-zero probability of being detected, it must be larger or equal to the U_{im} and have the potential to have a CNR above 2.5. For example, the 450 Kev system used in the experiment had at U_{im} of 0.390 mm when imaging a 25.4 mm (1 in.) thick block of titanium. Normalizing flaw size by this U_{im} produces the POD chart in Figure 32. If the critical flaw size is between one and two U_{im}, then based on the POD value of the 1.63 U_{im} curve there is a 42% chance of this flaw being detected if it is at least 4% of the component's thickness. To validate this method of predicting image quality and the use of SMART DR in general, a 316 Stainless Steel fin produced by DED was inspected to using the information provided by SMART DR.

Chapter 6. Validation

One of DED's major benefits is its ability to produce large components with minimal material by only depositing material that is required to produce a near net shape. A good example of this is the 316 stainless steel fin, shown in Figure 33, which was produced by DED and measures 345 mm wide, 290 mm tall, and 40 mm thick. This fin presents a challenge for CT scanning due to excessive thickness in certain orientations and the high density of stainless steel. Since DR does not require that the component be radiographically imageable around an entire axis, the orientation of the component can be optimized to allow an area of interest of be imaged. By using SMART DR, optimal radiographic orientations can easily be achieved along with the work instructions for component placement.

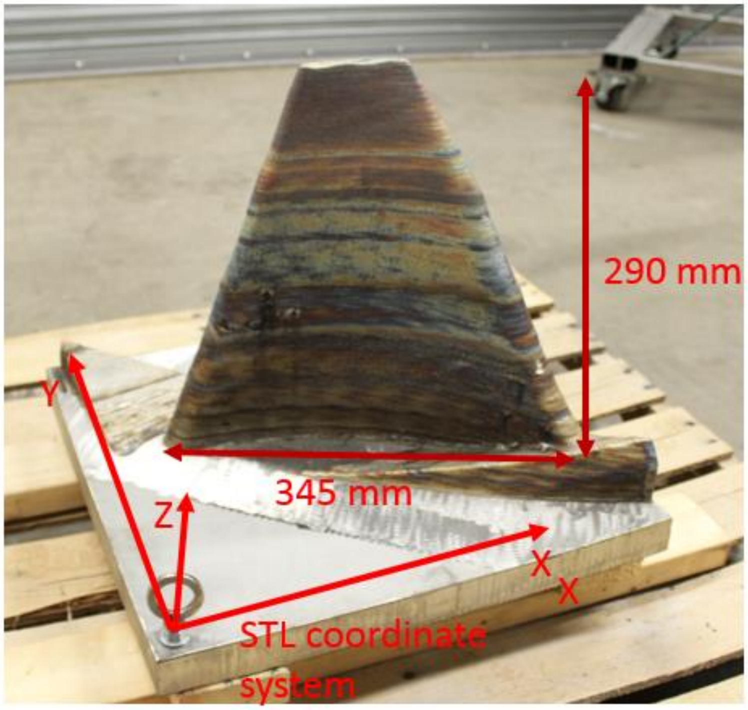

Figure 33 Fin produced using the DED process and stainless steel 316 material

Figure 34 illustrates how the fin STL was manipulated during the SMART DR workflow. When first loading the fin into SMART DR, the component's coordinate system must be aligned with the inspection coordinate system since a STL's coordinate system is arbitrary. SMART DR queries the user to define what inspection axes correlate to the build direction and positive y axis of the fin. Step 1 in Figure 34 shows the loading orientation of the STL where the +Z and +Y axis of the inspection coordinate system correlates with the build direction and positive Y axis of the fin. The fin is reoriented, and the user is shown the fin as seen by the DR system to select the area of interest, as seen in Figure 34 Steps 2 and Step 3. The selection of the area of interest repositions the center of the x-ray source to the center of the area of interest, which is shown in Figure 34 Step 4. A flaw size of 0.5 mm was chosen as the critical flaw size to be imaged, and the orientation optimizer was performed. Part orientation and optimization within SMART DR had a total run time of five minutes. The resulting inspection plan for the fin can be seen in Figure 35.

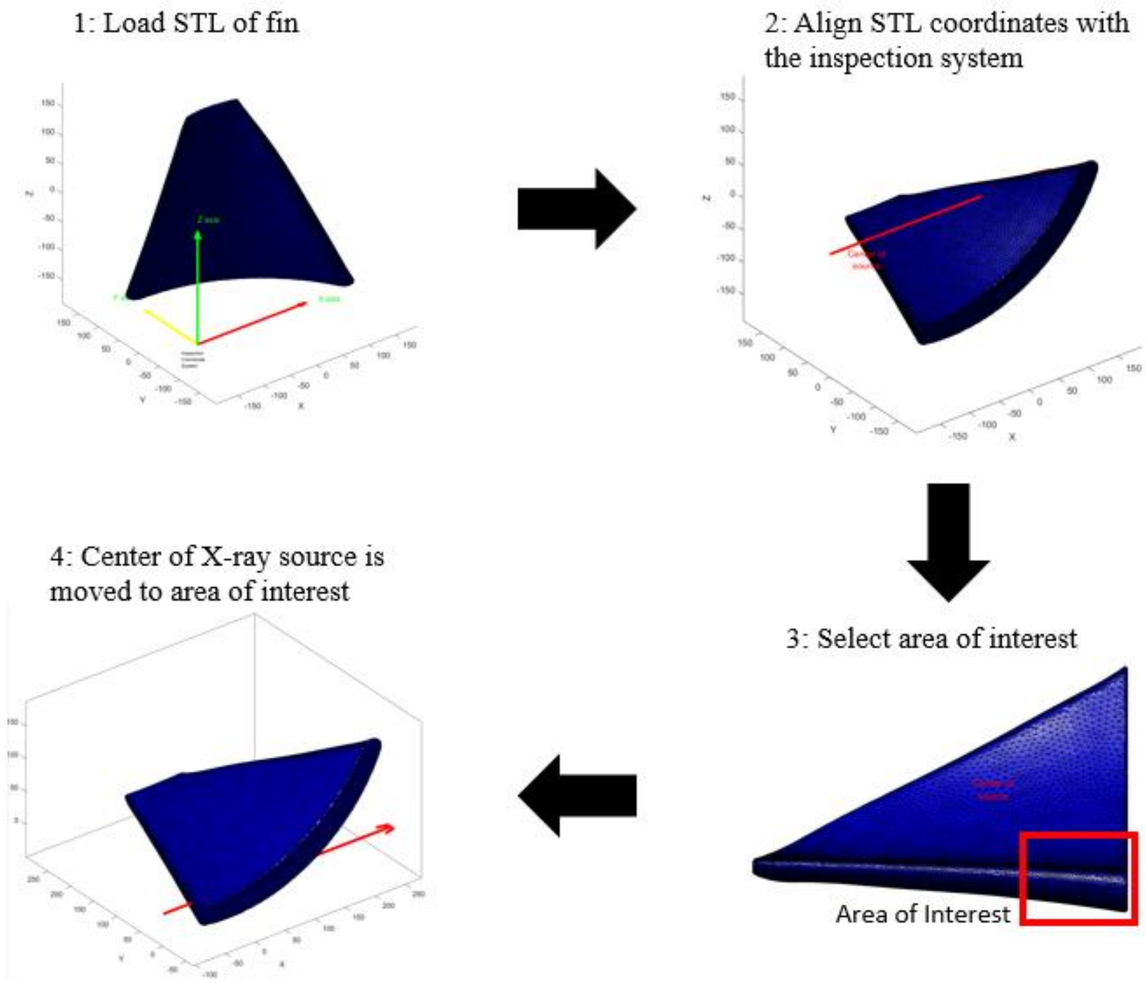

Figure 34 Manipulation of the fin STL in SMART DR

Alignment

Step 1:
Align the ZY plane of the Inspection system with the ZY plane of the fin so that is normal points towards the detector

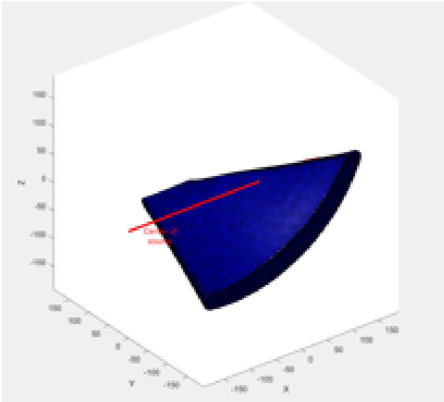

Area of Interest

Step 2:
Position the center of the beam -12 mm in the Y and -176 mm in the Z from the top of the fin

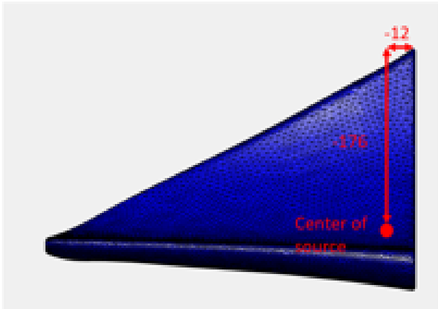

Optimal Orientation

Step 3:
Rotate the fin 59 degrees about the Y axis and 10 degrees about the Z axis and place against the DDA

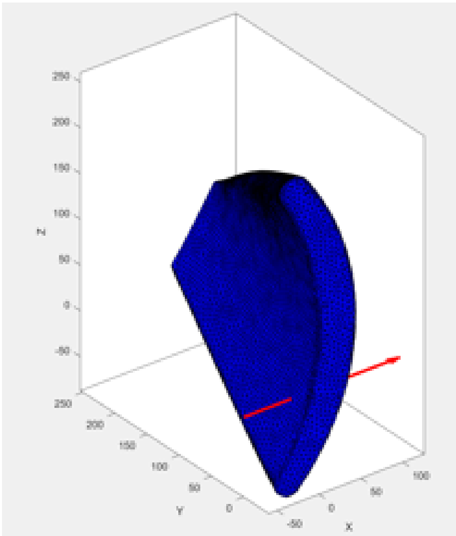

Figure 35 Inspection plan for fin based on SMART DR (red arrow on bottom image indicates the center of the X-ray source)

In the optimal orientation, a thickness of 40mm was achieved. To utilize the contrast and resolution metrics, the thickness of the stainless steel is normalized based on an equivalent thickness of Ti-6Al-4V alloy that will produce the same level of attenuation. This can be performed quite easily for energies up to 450 Kev because radiographic equivalence and conversion factors are well documented [9]. These factors allow for the conversion between different materials radiographically. To convert from stainless steel to Ti-64 the thickness of the stainless steel is multiplied by 1.41 to obtain a radiographically equivalent thickness [9]. This is due to stainless steel's higher density when compared to Ti-6Al-4V; so, 25.4 mm (1 in.) of stainless steel is radiographically equivalent 1.41 mm of Ti-6Al-4V. Since the fin is 40mm thick, 56.4 mm of Ti-6Al-4V is the equivalent thickness. Figure 36 shows the probability of detection for flaws between 0.5 mm and 1 mm in diameter for 40 mm thick stainless steel based on an equivalent 56.4 mm thickness of Ti-6Al-4V. To calculate the POD for values of energy, thicknesses, and flaw diameter that are in between the experimental data, both quadratic and linear interpolation is used. For intermediate values of source energy and component thickness, quadratic interpolation is used since both of these data sets are quadratic in nature. Intermediate flaw diameters are calculated though linear interpolation.

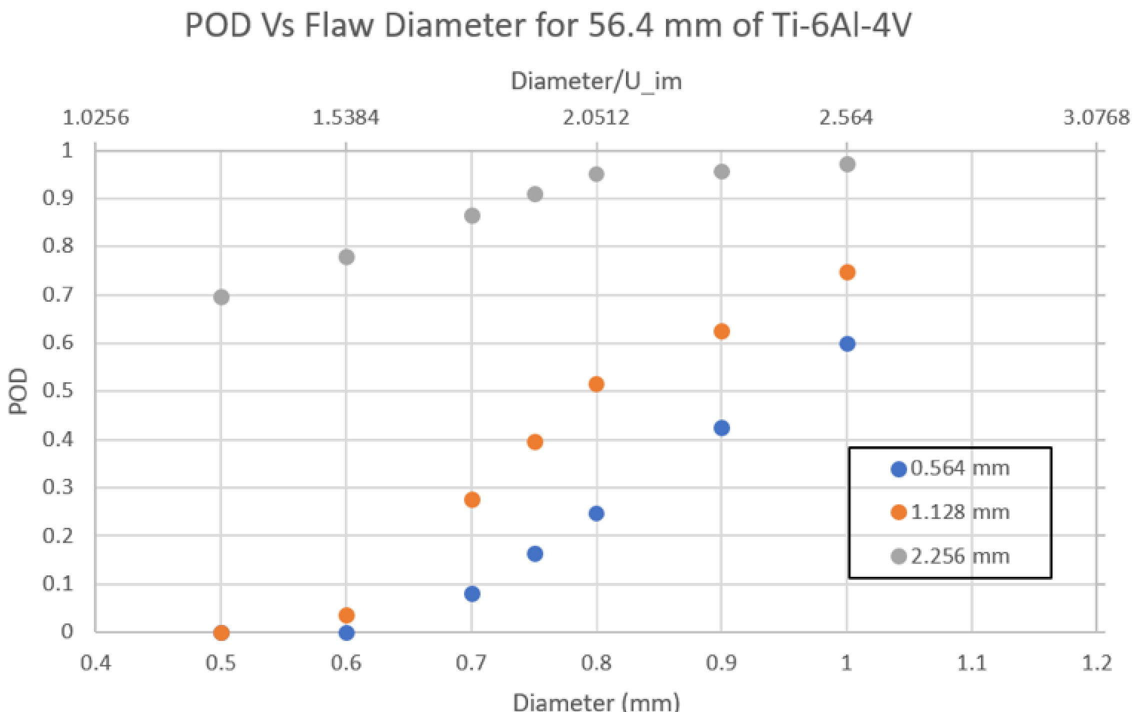

	Flaw Diameter (mm)	0.5	0.6	0.7	0.75	0.8	0.9	1
	Flaw Diameter/U_im	1.282051	1.538462	1.794872	1.923077	2.051282	2.307692	2.564103
Flaw length	0.564 mm	0%	0%	8%	16%	25%	42%	60%
	1.128 mm	0%	4%	28%	40%	52%	63%	75%
	2.256 mm	70%	78%	87%	91%	95%	96%	97%

Figure 36 POD for flaw diameters between 0.5mm and 1mm for 56.4mm of Ti-64

With the optimal orientation determined and the inspection plan created, the fin can be positioned in the DR system as shown in Figure 37. However, a small modification was made to the orientation of the fin when it was positioned in the DR system to enable the fin to be positioned easily within the inspection area. This necessitated the fin to be rotated 180° about the x-axis.

Figure 37 Optimal positioning of the fin in the DR system

Rotation about the x-axis does not impact the resulting radiograph because the as-seen thickness of the fin did not change. Also, additional shielding was placed directly onto the DDA above the fin to reduce the effects of edge scattering. The entire DR system with the Yxlon Y.TU450-D10 450 Kev, GE DXR250U-W DDA and fin is shown in Figure 38.

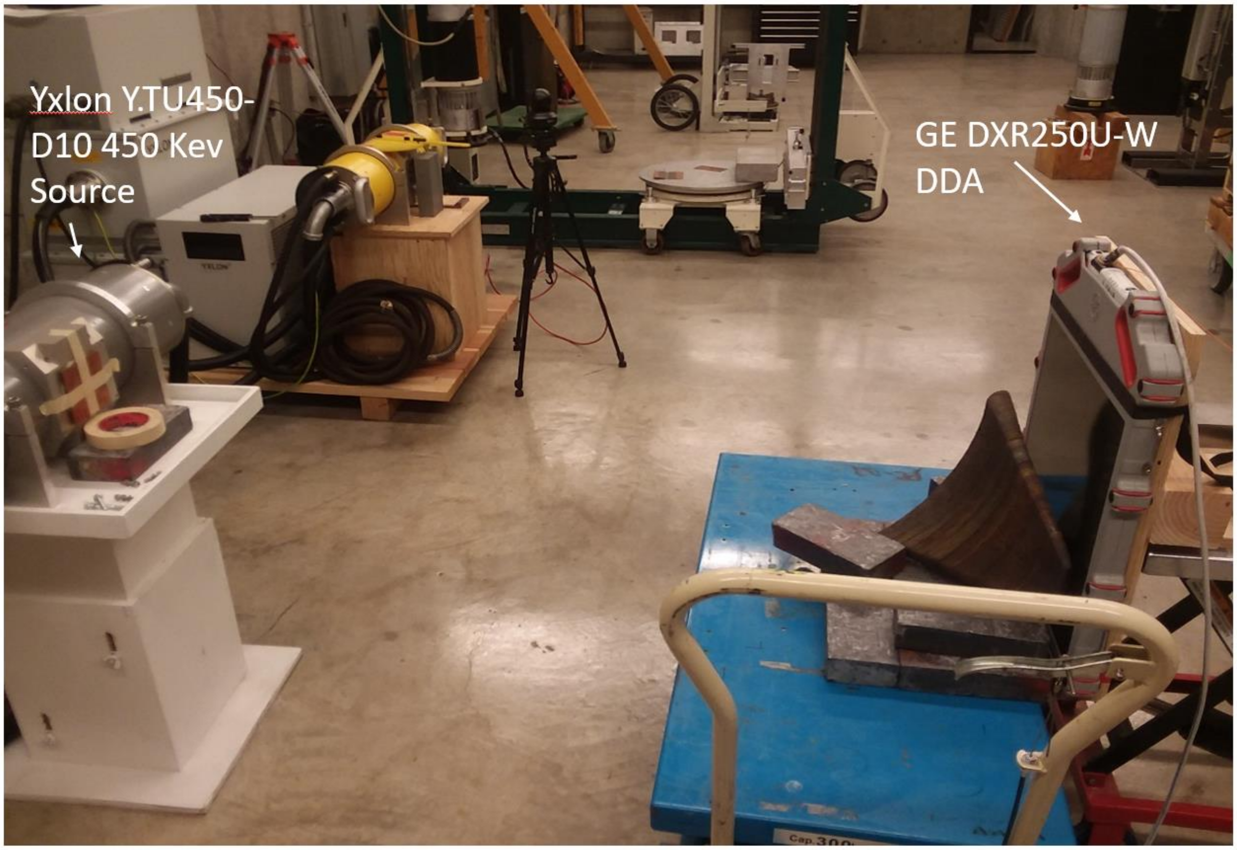

Figure 38 450 Kev source setup

The exposure times and number of integrations were changed until the radiograph of the fin used the full energy range of the detector without oversaturating areas of interest. The final radiograph of the fin can be seen in Figure 39. Examination of the radiograph shows significant large-scale porosity with diameters of 0.508 mm and 0.764 mm (0.02 in. and 0.03 in.). Examples of these are shown in Figure 40.

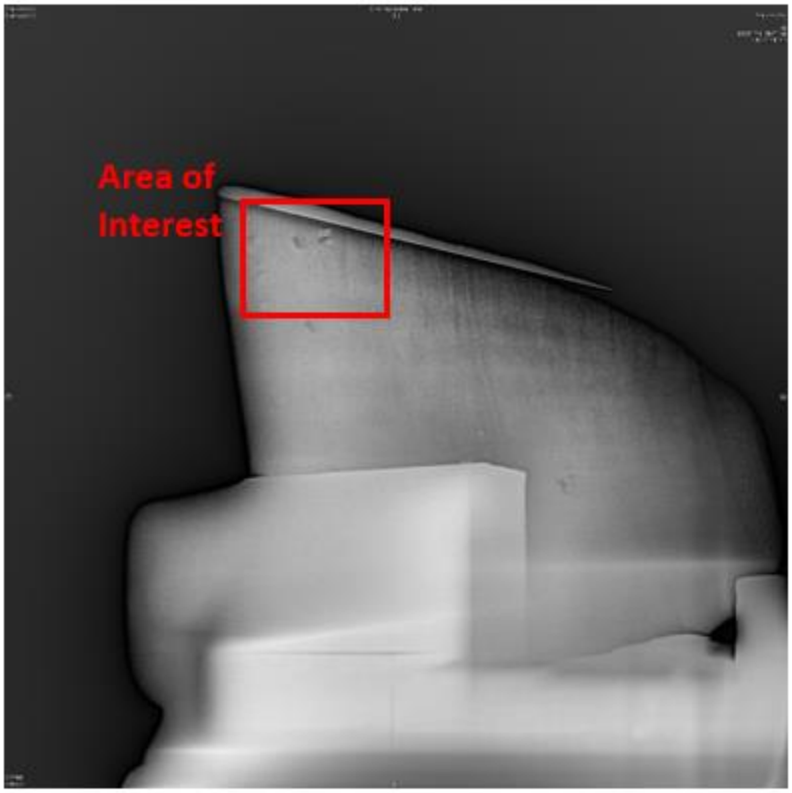

Figure 39 Radiograph of corner of fin

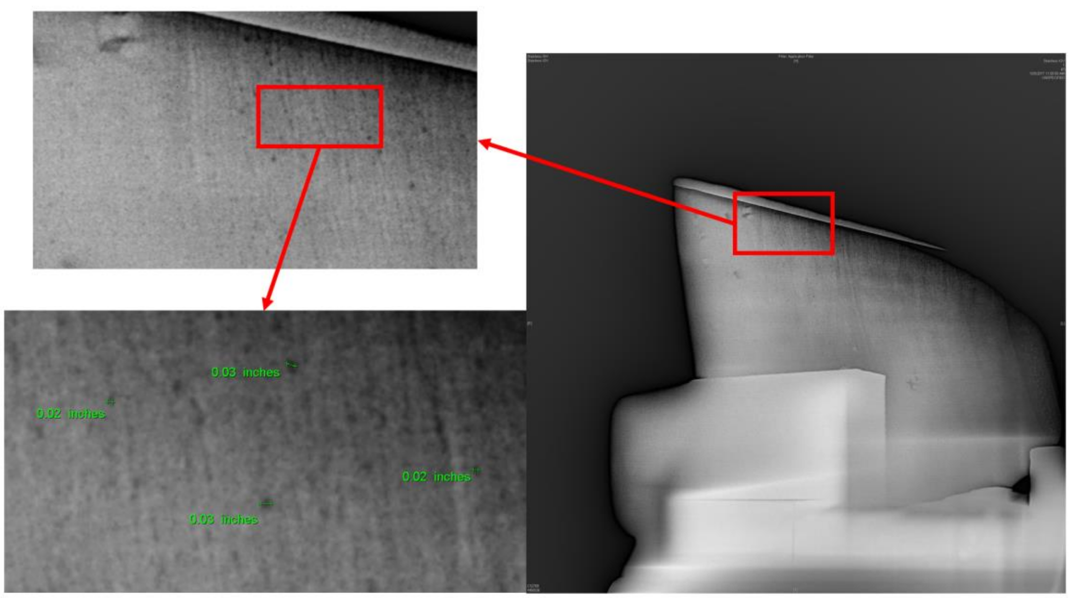

Figure 40 Example of imaged porosity

The size of these flaws has good correlation with the contrast and definition metrics that were created from the experimental data. For a cylindrical flaw with a diameter of 0.764 mm and a length of 0.400mm, 0.800mm, or 1.60 mm, which corresponds to 4%, 2%, and 1% of the fins total thickness, the probability of detection is 91%, 20.7% and 21.7% respectively, as shown in Figure 36.

Initial validation testing of SMART DR through the radiographic inspection of a 40mm stainless steel fin demonstrated SMART DR's effectiveness in providing optimal radiographic orientations and image quality predictions. The computational run-time was sufficiently short to not impede the progress of the inspection, even with the need for multiple iterations due to changes in the STL and different areas of interest. The probability of detection metric showed that flaw sizes of interest were detectable if imaged in the calculated orientation. The total inspection time was reduced because the iterative imaging process was reduced to a single optimal orientation. Lastly the radiographs of the fin showed clear indications of small spherical porosity with diameters between 0.508 mm and 0.764 mm. These flaw sizes were near the detectability limits provided by SMART DR (see Figure 36) and showed good agreement between the probability of detection and the experimental results.

Chapter 7 Conclusion and Future Work

7.1 Conclusion

SMART DR was developed to optimize the digital radiography inspection process for large additively manufactured components. Digital radiography outperforms computed tomography for components larger than several centimeters because of unrestricted inspection volumes, source energies higher than 450 Kev, and better imaging of high aspect ratio components. SMART DR combines a robust orientation optimization scheme and probability of detection metric with a user friendly GUI to improve and expedite the DR inspection process.

Optimal radiographic orientations for an area of interest are determined by an efficient parallelized ray tracing algorithm combined with a genetic optimization scheme to minimize the penetration thickness of the component. A novel method for predicting flaw detectability was derived from experimental digital radiography contrast and definition data. By utilizing DR system specific parameters and component thickness, the probability of detection for a flaw size of interest can be calculated. Validation was performed through the inspection of a 316 stainless steel fin produced using the DED process that was 40 mm thick. Conclusions that can be drawn from this work are as follows.

- SMART DR reduces the iterative DR inspection process to one or two optimal imaging orientations and provides a metric for flaw size detectability. Overall, this reduces the cost and time of inspection by reducing the number of required radiographs to inspect and qualify a component.
- SMART DR enables the inspectability of areas of interest such as rapid geometrical changes or safety critical features, to be analyzed prior to manufacturing. If the in-house

DR system is not sufficient to inspect the areas of interests, then design changes can be made to improve the imageability of the area of interest or to strengthen it.

- SMART DR was designed to have a wide range of application and not specific to a DR system. Therefore, only seven basic system parameters are required: (1) detector pitch, (2) width, (3) height, and (4) basic spatial resolution, (5) source energy, and (6) spot size, and the (7) operating distance.
- To optimize the DR inspection process, a ray trace algorithm coupled with a genetic optimization scheme is used to determine the optimal radiographic orientations, and experimental CNR values, and the U_{im} of the DR system are used to determine flaw size detectability.
- A parallelized back projection algorithm allows for efficient ray path determination for a given orientation. Computational time is unrelated to the component complexity and increases with both the number of triangles in the STL and the pitch of the DDA being used.
- Experimental data led to the development of an image quality metric that defines probability of detecting a flaw of a given size. This metric combines the contrast-to-noise ratio and normalized image unsharpness to incorporate both the contrast and definition of a DR system.
- Validation of SMART DR through the inspection of an additively manufactured 40mm stainless steel fin showed that there was good agreement between the detectable flaw sizes and the image quality metric. Flaws of 0.76 mm were detected in the radiograph, and the probability of detection for a .078 mm flaw was 91%, 20.7% and 21.7% of its length is 4%, 2%, or 1% of the total thickness, respectively. The low probability of

detection indicates that 0.78mm flaw should be near the limits of the imageability of the DR system used in this study. No viable flaws smaller then 0.5mm were found on the radiographs, demonstrating that SMARTS DR image quality metric is viable.

7.2 Future Work

Future work should focus on improving the GUI, decreasing the computational time of the ray trace algorithm, and increasing the accuracy and fidelity of the probability of detection metric. Improvements to the GUI will aid in creating a more intuitive and user-friendly application. Nomenclature and phrasing for prompts and commands should to be updated so that they are clear and precise to users of all experience levels

. Reductions in the computational time can be achieved in several ways. The most promising reduction will come from converting/rewriting the algorithm into C++ or Python, both of these languages having reduced overhead allowing for faster computational speed. In conjunction with language conversion, increased parallelization through graphic card processing should further reduce computational time. Finally, removal of for loops and build in functions would eliminate iterative computations and further reduce overhead. The probability of detection metric would benefit from a second experiment with a wider range of smaller holes that straddles the detectability limits of the various energy and component thickness combinations used in this study. This new data along with a larger amount of sampling would improve both the accuracy and reliability of the probability of detection metric.

References

[1] Y. Huang, M. C. Leu, J. Mazumder, and A. Donmez, “Additive Manufacturing: Current State, Future Potential, Gaps and Needs, and Recommendations,” *J. Manuf. Sci. Eng.*, vol. 137, p. 14001, 2015.

[2] E. Sachs, S. Allen, M. Cima, E. Wylonis, and H. Gu, “Production of Injection Molding Tooling With Conformal Cooling Channels Using the Three Dimensional Printing Process,” *Polym Eng Sci*, vol. 40, pp. 1232–1247, 2000.

[3] J. Schmelzle, E. V. Kline, C. J. Dickman, E. W. Reutzel, G. Jones, and T. W. Simpson, “(Re)Designing for part consolidation: understanding the challenges of metal additive manufacturing,” *J. Mech. Des.*, vol. 137, no. 11, 2015.

[4] R. Dehoff, C. Duty, W. Peter, Y. Yamamoto, W. Chen, C. Blue, and C. Tallman, “Case study: Additive manufacturing of aerospace brackets,” *Adv. Mater. Process.*, vol. 171, no. 3, pp. 19–22, 2013.

[5] D. Cooper, J. Thornby, N. Blundell, R. Henrys, M. A. Williams, and G. Gibbons, “Design and manufacture of high performance hollow engine valves by Additive Layer Manufacturing,” *Mater. Des.*, vol. 69, pp. 44–55, 2015.

[6] National Institute for Standards and Technology, *Measurement Science Roadmap for Metal-Based Additive Manufacturing*. 2013.

[7] A. Bauereiss, T. Scharowsky, and C. Korner, “Defect generation and propagation mechanism during additive manufacturing by selective beam melting,” *J. Mater. Process. Technol.*, vol. 214, no. 11, pp. 2497–2504, 2014.

[8] A. Lamarre, O. Dupuis, and M. Moles, “Complete inspection of friction stir welds in aluminum using ultrasonic and eddy current arrays,” in *16th WCNDT , Monteral, Canada,* 2004.

[9] American Society for Nondestructive Testing, *Nondestructive Testing Handbook*, 2nd ed. American Society for Nondestructive Testing, 2011.

[10] J. M. Waller, B. H. Parker, K. L. Hodges, E. R. Burke, and J. L. Walker, “Nondestructive Evaluation of Additive Manufacturing State-of-the-Discipline Report,” *NASA/TM-2014-218560*, pp. 1–36, 2014.

[11] K. M. Taminger and R. A. Hafley, “Electron Beam Freeform Fabrication for Cost Effective Near-Net Shape Manufacturing,” *Nato Unclassif.*, pp. 1–19, 2004.

[12] G. J. Schiller, “Additive manufacturing for Aerospace,” *IEEE Aerosp. Conf. Proc.*, vol. June, 2015.

[13] E. Atzeni and A. Salmi, “Economics of additive manufacturing for end-usable metal parts,” *Int. J. Adv. Manuf. Technol.*, vol. 62, no. 9–12, pp. 1147–1155, 2012.

[14] M. I. Mohammed, A. P. Fitzpatrick, and I. Gibson, “Customised design of a patient specific 3D printed whole mandible implant,” in *The International Conference on Design and Technology*, 2017, pp. 104–111.

[15] ASTM International, “Standard Terminology for Additive Manufacturing – General Principles – Terminology,” *ISO/ASTM52900-15*, pp. 1–9, 2015.

[16] “The MakerBot Replicator+ | MakerBot.” [Online]. Available: https://www.makerbot.com/replicator/. [Accessed: 21-Mar-2018].

[17] C. E. Duty, V. Kunc, B. Compton, B. Post, D. Erdman, R. Smith, R. Lind, P. Lloyd, L. Love, and P. L. Lonnie, “Structure and mechanical behavior of Big Area Additive Manufacturing (BAAM) materials Structure and Mechanical Behavior of Big Area Additive Manufacturing (BAAM) Materials,” *Rapid Prototyp. J.*, vol. 23, no. 1, 2017.

[18] B. Post, B. Richardson, P. Lloyd, Lonnie Love, and S. N. Tpi, “Additive Manufacturing of Wind Turbine Molds,” no. June, 2017.

[19] S. Stecker, K. Lachenberg, H. Wang, and R. Salo, “Advanced Electron Beam Free Form Fabrication Methods & Technology,” in *AWS Welding Show*, 2006, pp. 35–46.

[20] R. Liu, Z. Wang, T. Sparks, F. Liou, and J. Newkirk, *Aerospace applications of laser additive manufacturing*. Elsevier Ltd, 2016.

[21] T. Yamazaki, “Development of A Hybrid Multi-tasking Machine Tool: Integration of Additive Manufacturing Technology with CNC Machining,” *Procedia CIRP*, vol. 42, pp. 81–86, 2016.

[22] E. Wycisk, A. Solbach, S. Siddique, D. Herzog, F. Walther, and C. Emmelmann, “Effects of defects in laser additive manufactured Ti-6Al-4V on fatigue properties,” *Phys. Procedia*, vol. 56, pp. 371–378, 2014.

[23] G. N. Hounsfield, “Computerized transverse axial scannin g (tomography): Part 1. Decription of system,” *Br. J. Radiol.*, vol. 46, pp. 1016–1022, 1973.

[24] F. Léonard, S. Tammas-williams, P. B. Prangnell, I. Todd, P. J. Withers, H. Moseley, and X. I. Facility, “Assessment by X-ray CT of the effects of geometry and build direction on defects in titanium ALM parts,” *Conf. Ind. Comput. Tomogr.*, pp. 85–93, 2012.

[25] Y. V. Alkhimov, S. F. Gnyusov, B. I. Kapranov, V. A. Klimenov, and A. M. Orishich, "Investigation of laser-welded titanium and stainless steel specimens using digital radiography methods," *Russ. J. Nondestruct. Test.*, vol. 48, no. 4, pp. 238–244, 2012.

[26] V. A. Udod, Y. Van, S. P. Osipov, S. V. Chakhlov, E. Y. Usachev, M. B. Lebedev, and A. K. Temnik, "State-of-the art and development prospects of digital radiography systems for nondestructive testing, evaluation, and inspection of objects: a review," *Russ. J. Nondestruct. Test.*, vol. 52, no. 9, pp. 492–503, 2016.

[27] V. Rebuffel, S. Sood, and M. Keynes, "Defect Detection Method in Digital Radiography for Porosity in Magnesium Castings," *ECNDT*, pp. 1–10, 2006.

[28] D. Mery, T. Jaeger, and D. Filbert, "A review of methods for automated recognition of casting defects," *Insight Non-Destructive Test. Cond. Monit.*, vol. 44, no. 7, pp. 428–436, 2002.

[29] D. Mery and M. Carrasco, "Automated multiple view inspection based on uncalibrated image sequences," *Image Anal. Proc.*, vol. 3540, pp. 1238–1247, 2005.

[30] P. Sprawls, *Physical Principles of Medical Imaging*, 2nd ed. Gaithersburg: Md: Aspen Publishers, 1993.

[31] P. A. Rometsch, D. Pelliccia, D. Tomus, and X. Wu, "Evaluation of polychromatic X-ray radiography defect detection limits in a sample fabricated from Hastelloy X by selective laser melting," *NDT&E Int.*, vol. 62, pp. 184–192, 2014.

[32] ASTM, "Standard Guide for Radiographic Examination," *E94-4*, pp. 1–13, 2010.

[33] ASTM, "Standard Guide for Radioscopy," *E1000-98*, pp. 1–20, 2015.

[34] ASTM, “Standard Guide for Digital Detector Array Radiology,” *E2736-10*, pp. 1–22, 2015.

[35] ASTM, “Standard Practice for Determining Total Image Unsharpness and Basic Spatial Resolution in Radiography and Radioscopy,” *E2002*, pp. 1–7, 2015.

[36] H. Heinrich, P. Ziegenhein, C. P. Kamerling, H. Froening, and U. Oelfke, “GPU-accelerated ray-tracing for real-time treatment planning,” *J. Phys. Conf. Ser.*, vol. 489, no. 1, 2014.

[37] J. Krüger and R. Westermann, “Acceleration Techniques for GPU-based Volume Rendering,” *IEEE Vis.*, pp. 287–292, 2003.

[38] R. L. Siddon, “Prism representation: A 3D ray-tracing algorithm for radiotherapy applications,” *Phys. Med. Biol.*, vol. 30, no. 8, pp. 817–824, 1985.

[39] N. Freud, P. Duvauchelle, J. M. Létang, and D. Babot, “Fast and robust ray casting algorithms for virtual X-ray imaging,” *Nucl. Instruments Methods Phys. Res. Sect. B Beam Interact. with Mater. Atoms*, vol. 248, no. 1, pp. 175–180, 2006.

[40] T. R. C. Ashok D. Belegundu, *Optimization Concepts and Applications in Engineering*, 2nd ed. Prentice Hall, 2011.

[41] H. Voigt, “Soft genetic operators in evolutionary algorithms,” in *Evolution and Biocomputation*, 1995, pp. 1–19.

[42] R. Storn and K. Price, “Differential Evolution – A Simple and Efficient Heuristic for global Optimization over Continuous Spaces,” *J. Glob. Optim.*, vol. 11, no. 4, pp. 341–359, 1997.

[43] ASTM, “Standard Practice for Manufacturing Characterization of Digital Detector Arrays,” *ASTM E2597/E2597M − 14*, pp. 1–19, 2014.

[44] ASTM, “Standard Practice for Radiological Examination Using Digital Detector Arrays,” *E2698-10*, pp. 1–9, 2015.

Appendix A – Coordinate Transformations and Conversions

World Coordinate System (WCS):

The WCS, Figure A-1, Represents the actual inspection volume of the radiographic system that was selected or created from the detector properties list in the application. Used when projecting STL vertices to the detector plane and when intersecting rays with the STL. Initially centered on the geometric middle of the bounding box produced by the component. This shifts as the user selects inputs and orientations within the application.

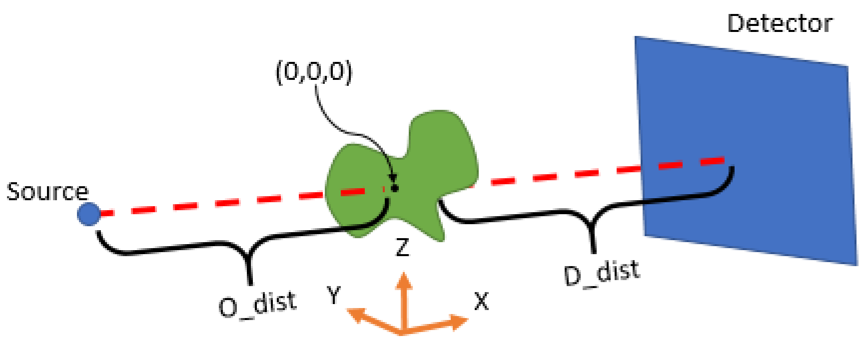

Figure A-1 WCS

Detector Coordinate System (DCS):

The DCS, figure A-2 is used after the STL vertices have been projected to the detector to determine which pixels lay inside each individual triangle. Switch the coordinate system to be centered on the top right corner of the detector allows for easier indexing and selection of pixels.

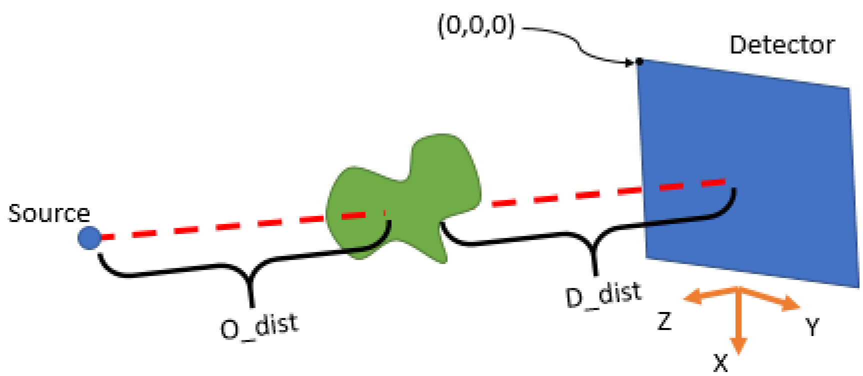

Figure A-2 DCS

Coordinate System Transformations:

Two different coordinate systems are used in back projection ray trace methods and it is necessary to be able to quickly convert between the two systems. Figure A-3 shows the two-different coordinate system and the comparison between them. The transformation between WCS and DCS is a two stage process first the WCS is rotated so that the axes align with the DCS then the rotated is translated to the (0, 0, 0) position of the DCS. After being rotated and translated, the WCS have be transformed into the DCS.

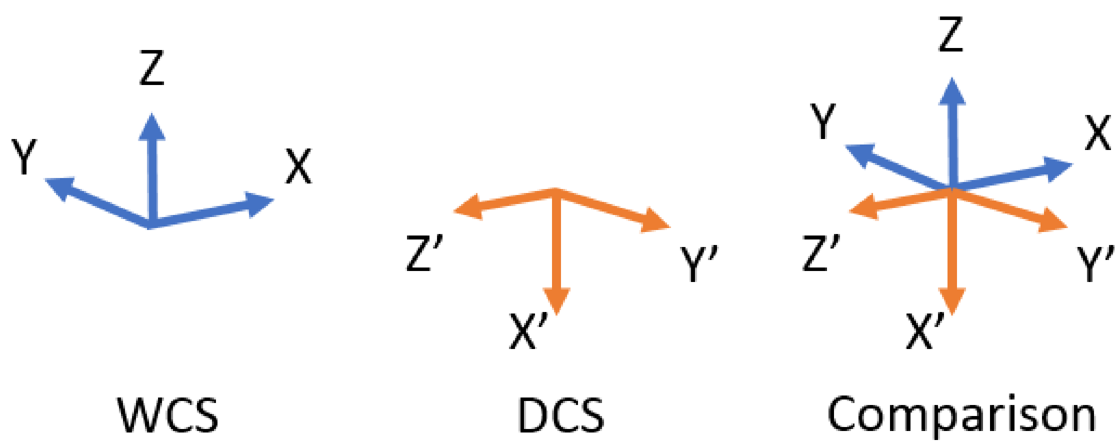

Figure A-3 Comparison of WCS and DCS

The rotation matrix consist of a three, 3x3 matrixes that describe the rotation along the X, Y and Z axes.

$$R_x = \begin{matrix} 1 & 0 & 0 \\ 0 & \cos\theta & -sin\theta \\ 0 & sin\theta & cos\theta \end{matrix} \quad R_y = \begin{matrix} \cos\theta & 0 & -sin\theta \\ 0 & 0 & 0 \\ sin\theta & 0 & cos\theta \end{matrix} \quad R_z = \begin{matrix} 1 & 0 & 0 \\ 0 & \cos\theta & -sin\theta \\ 0 & sin\theta & cos\theta \end{matrix}$$

$$R = R_x * R_y * R_z$$

By inspection of the WCS coordinate system it can be deduced that by rotating the 180 degrees about the X and 90 degrees about the Y, the axes can be aligned with the DCS, resulting in the following rotation matrix.

$$R_{wcs-dcs} = \begin{matrix} 0 & 0 & -1 \\ 0 & -1 & 0 \\ -1 & 0 & 0 \end{matrix}$$

With the axes of the coordinate system now properly aligned with the DCS, the origin now needs to be translated to the origin of the DCS (upper right corner of the detector).

$$T_{wcs-dcs} = [\, Detector_{Height}, Detector_{width}, D_{dist}] \qquad \text{Equation A-1}$$

The Detector_height, Detector_wdith, and D_dist indicate the X, Y, and Z location of the upper right corner of the detector in the WCS as seen in Figure A-4. Each value of T should then be added to its respective column of the rotated points as shown in the complete transformation as show below,

$$A_{dcs} = (A_{wcs}R_{wcs-dcs}) + T_{wcs-dcs} \qquad \text{Equation A2}$$

where A is an Nx3 matrix of (x,y,z) points.

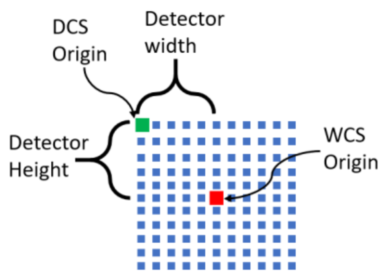

Figure A-4 Virtual DDA diagram

Appendix B – Ti-6Al-4V Experimental Blocks

Table B-1 Thickness and source energy combinations

		Energy (Mev)					
		0.45	3	4	6	8	12
Thickness (mm)	25.4	x					
	50.8	x	x				
	76.2	x	x	x			
	101.6		x	x	x		
	127		x	x	x	x	
	152.4		x	x	x	x	x
	177.8			x	x	x	x
	203.2				x	x	x

Table B-2 Thickness and flaw Diameter combinations

		Flaw Diameter (in)									
		0.410	0.790	1.194	1.600	1.981	2.387	2.77	3.175	3.581	3.962
Thickness (mm)	25.4	x	x	x	x	x					
	50.8		x	x	x	x	x				
	76.2			x	x	x	x	x			
	101.6			x	x	x	x	x			
	127				x	x	x	x	x		
	152.4					x	x	x	x	x	
	177.8					x	x	x	x	x	
	203.2						x	x	x	x	x

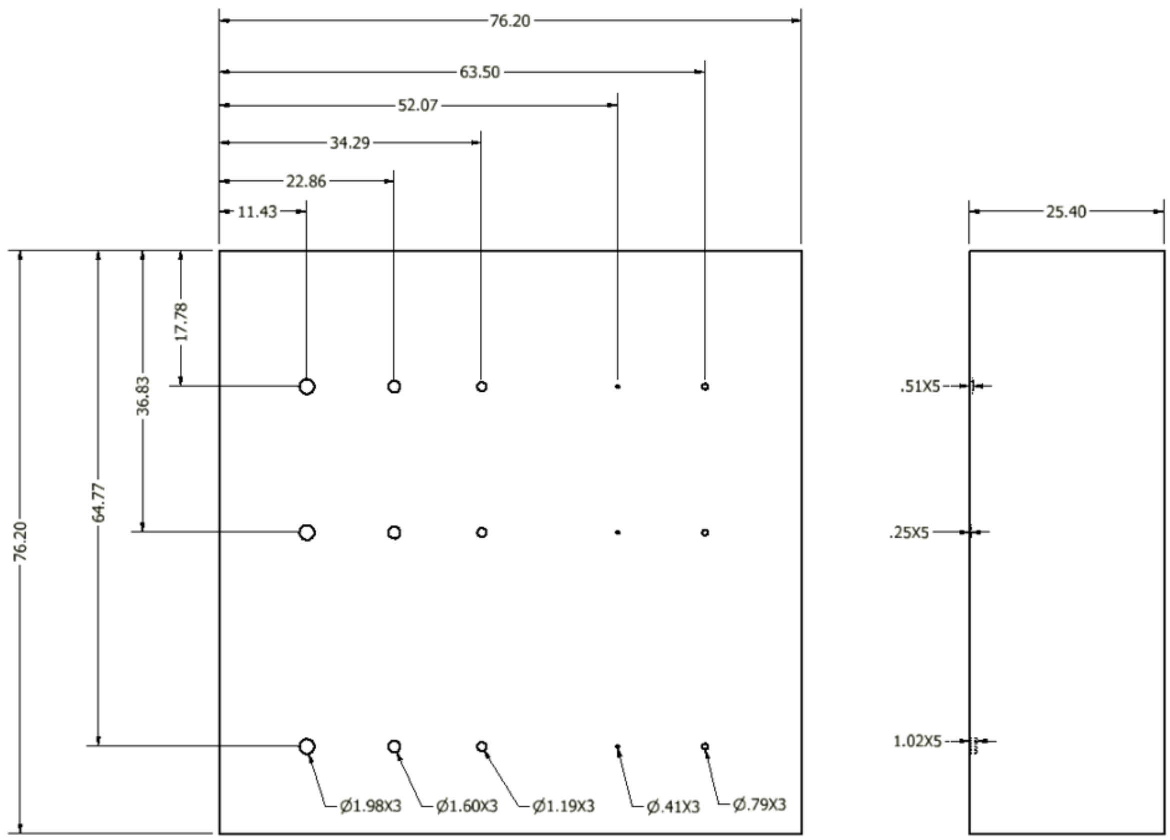

Figure B-1 25.4 mm Block Dimensions

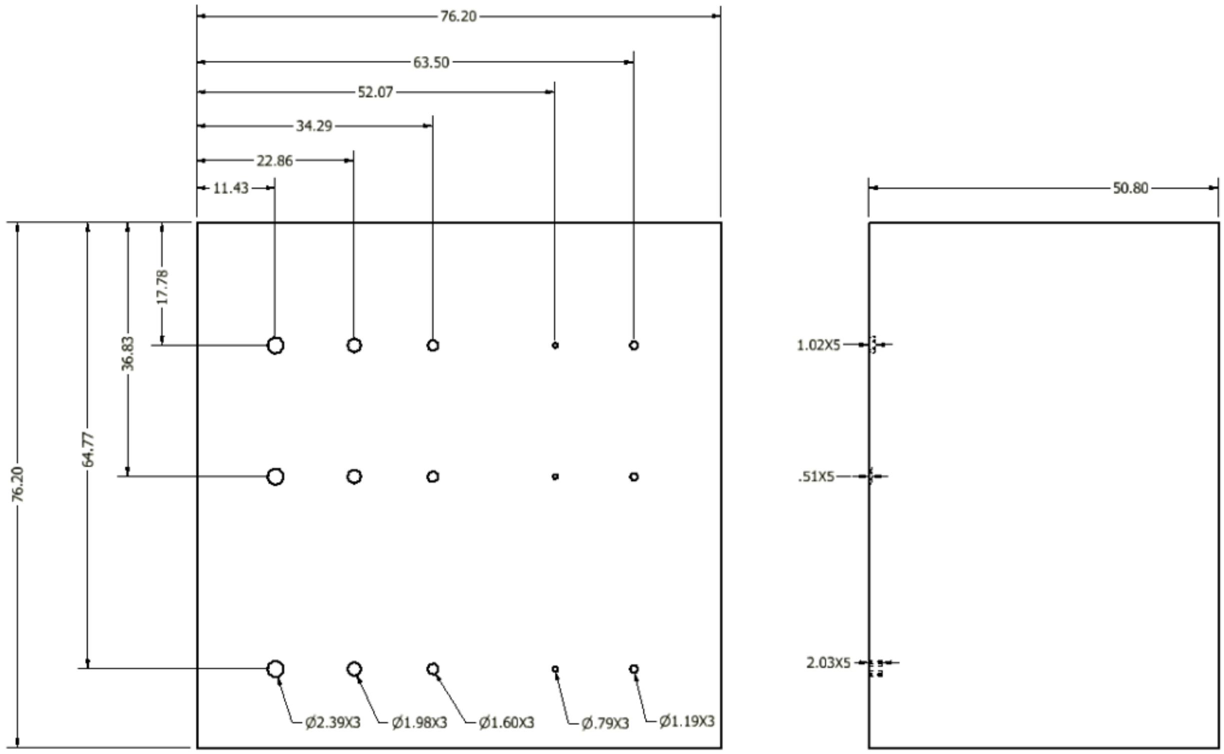

Figure B-2 50.8 mm Block Dimensions

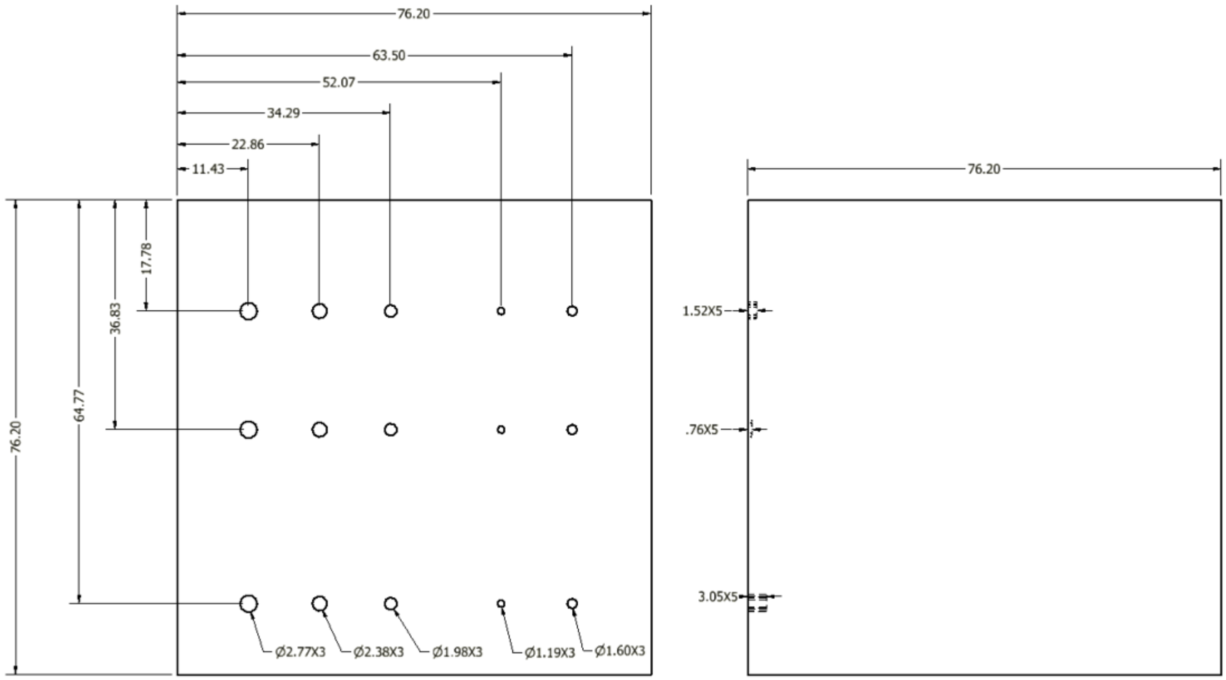

Figure B-3 76.2 mm Block Dimensions

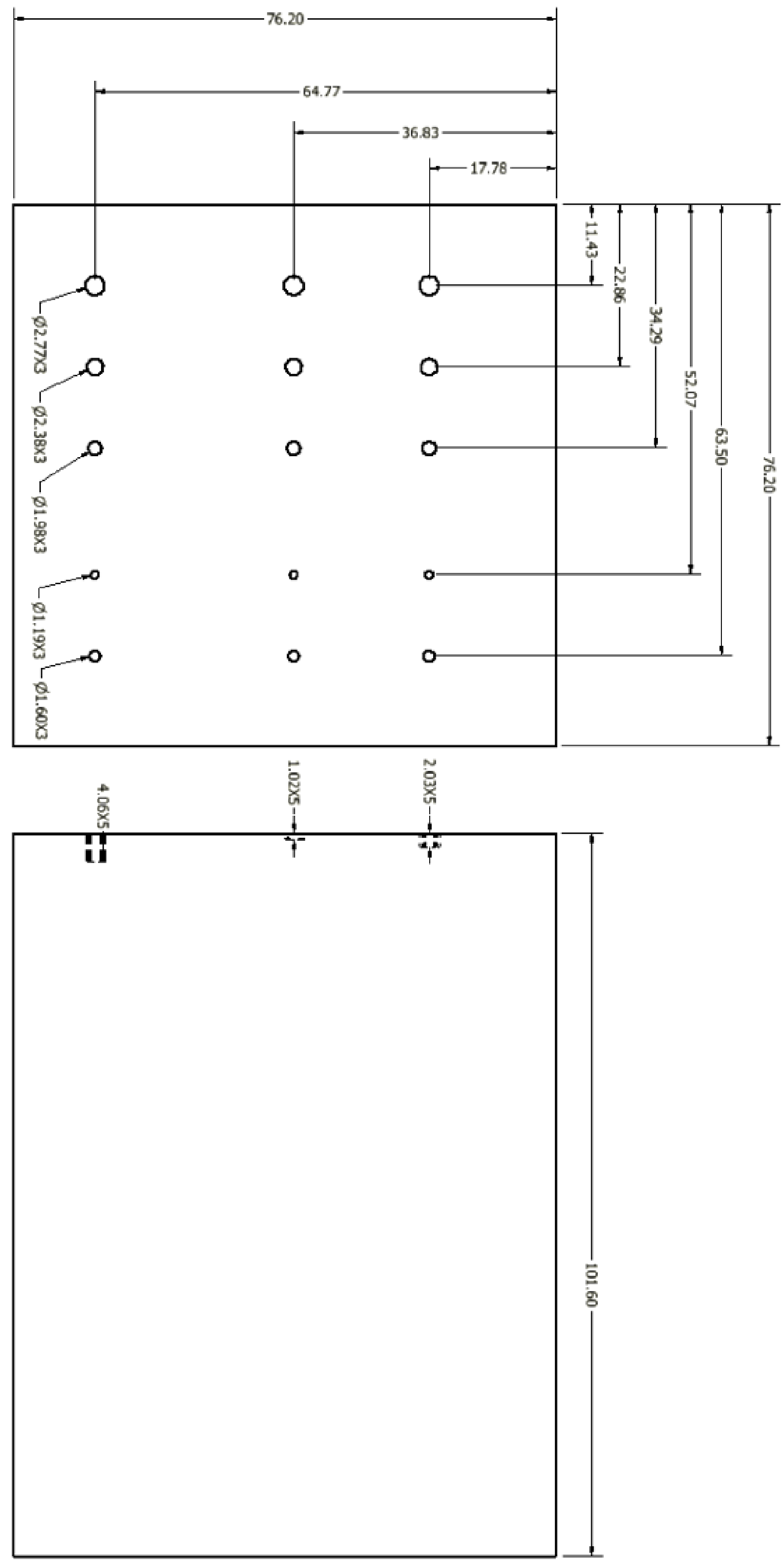

Figure B-4 101.6 mm Block Dimensions

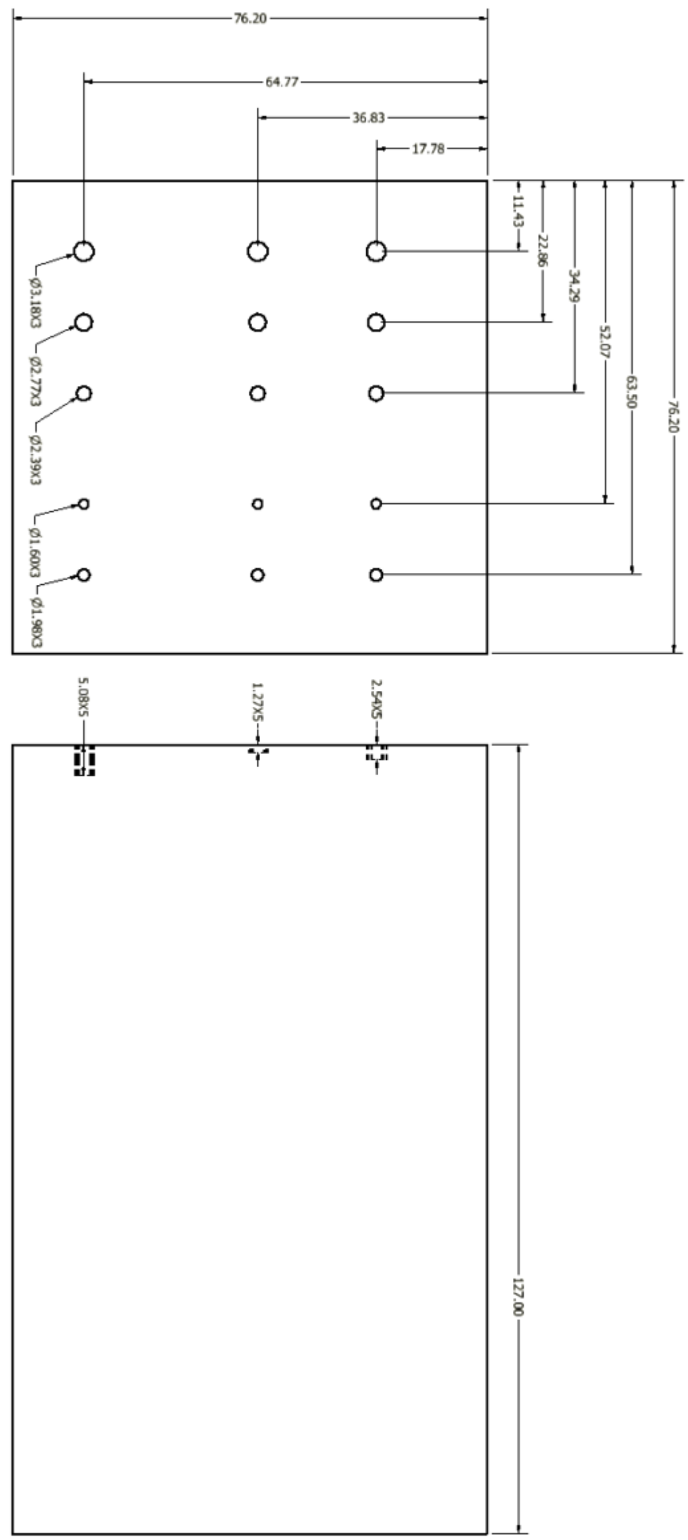

Figure B-5 127 mm Block Dimensions

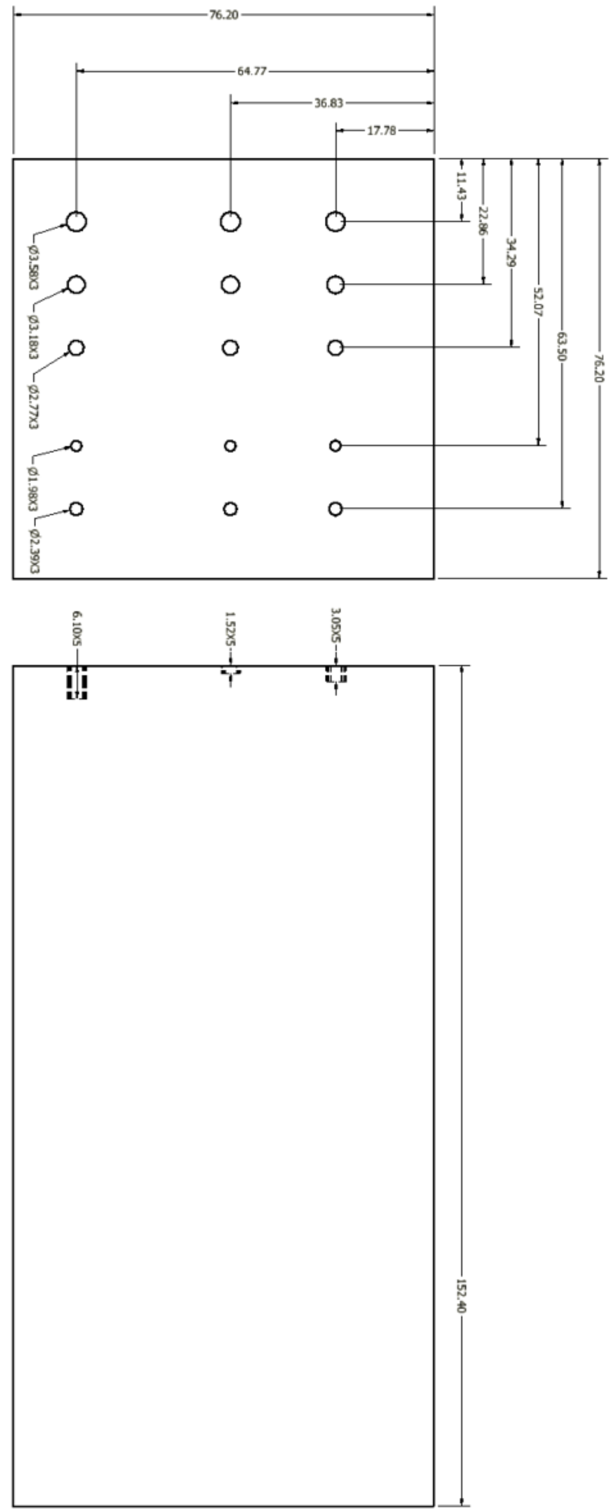

Figure B-6 152.4 mm Block Dimensions

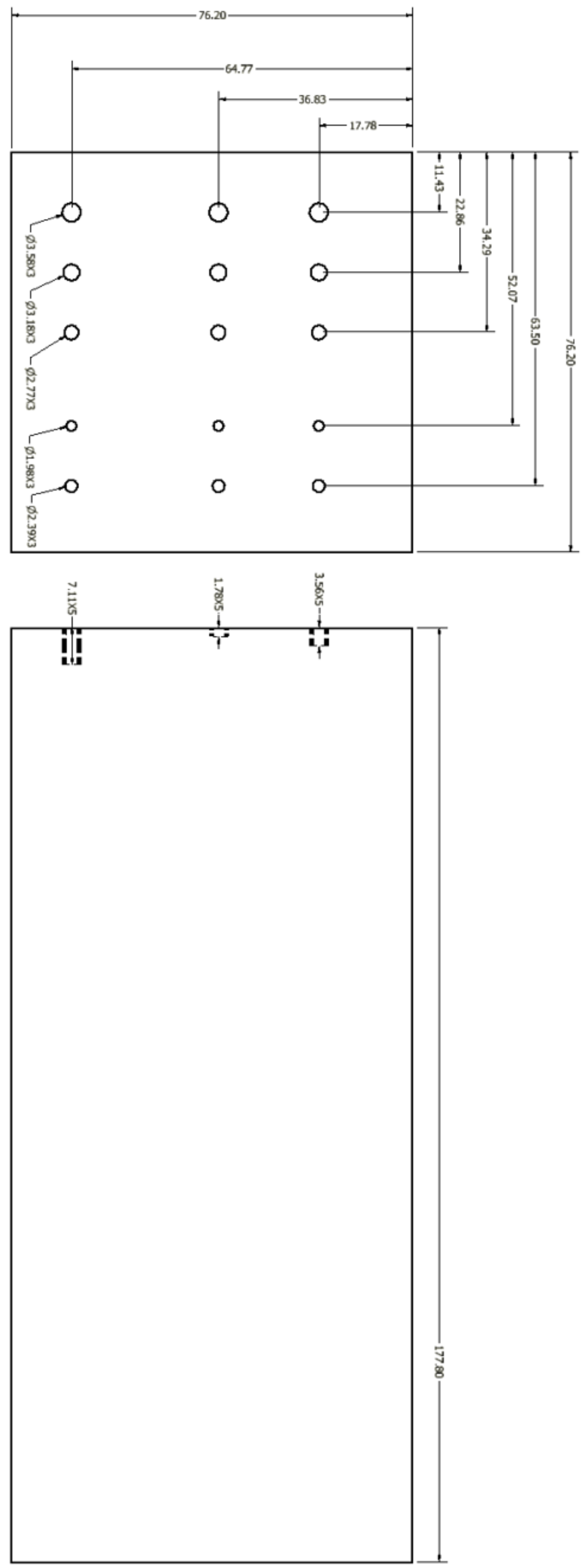

Figure B-7 177.8 mm Block Dimensions

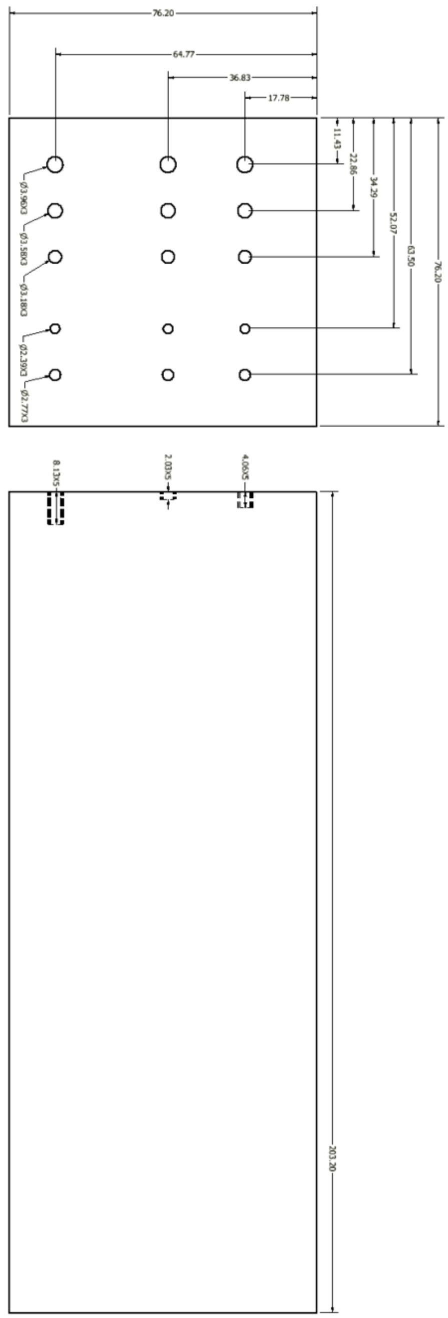

Figure B-8 203.2mm Block Dimensions

Appendix C – Experiment Radiographs

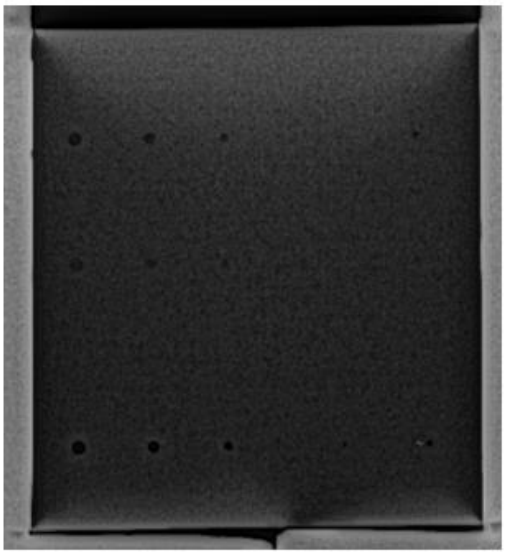

25.4 mm Thick

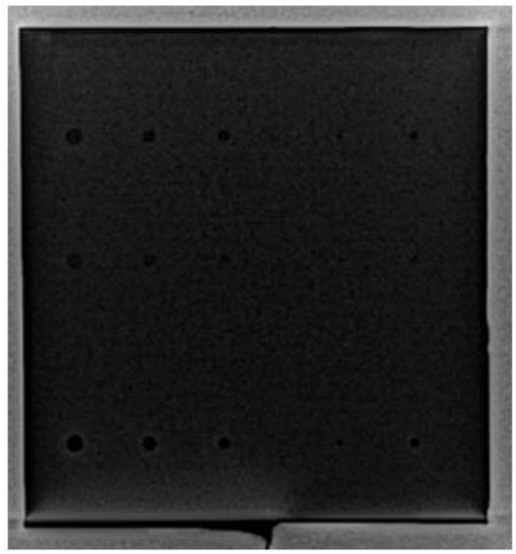

50.8 mm Thick

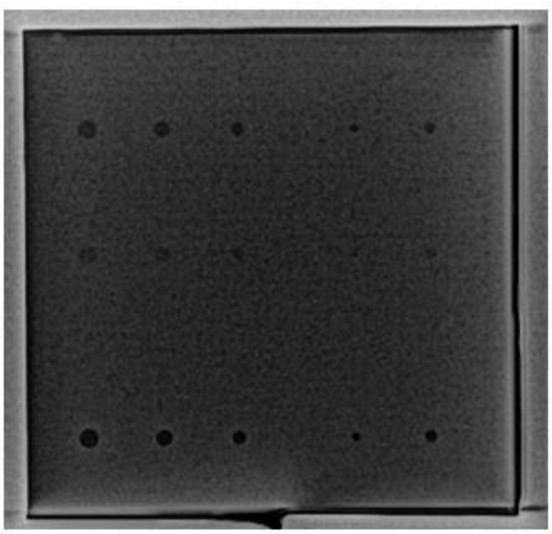

76.2 mm Thick

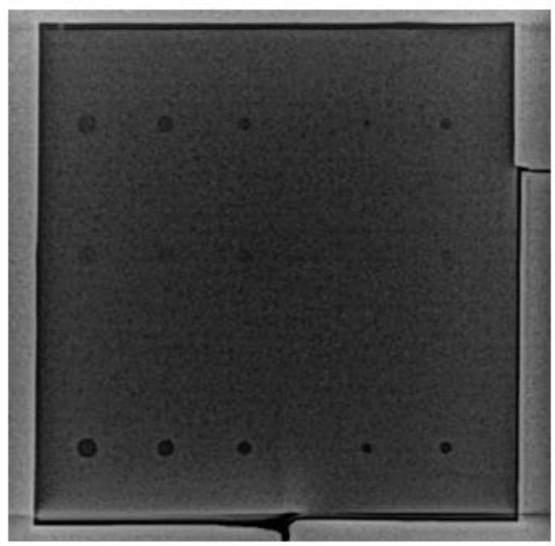

101.6 mm Thick

Figure C-1 0.450 Mev Radiographs

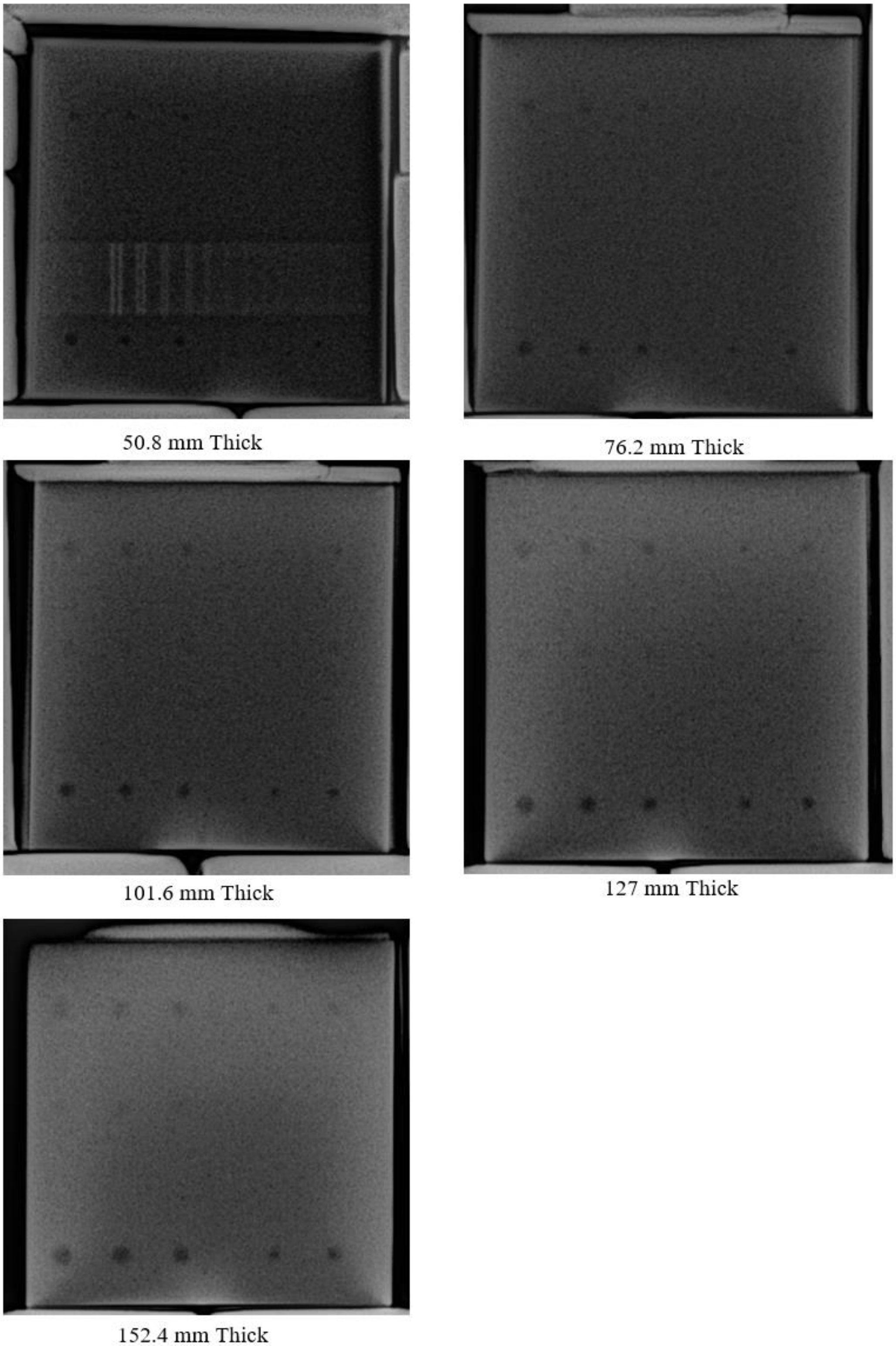

Figure C-2 3 Mev Radiographs

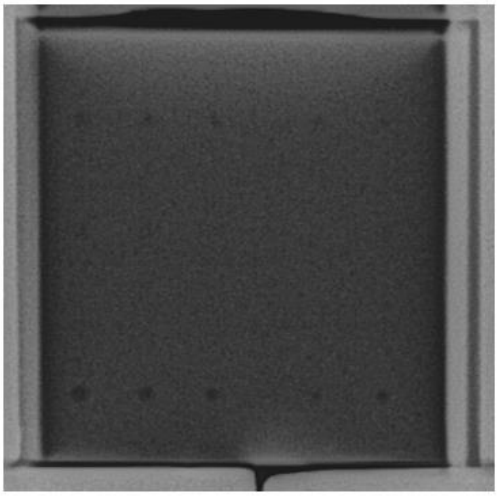

76.2 mm Thick

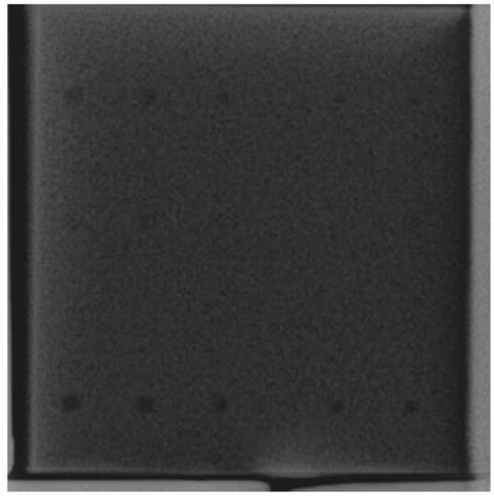

101.6 mm Thick

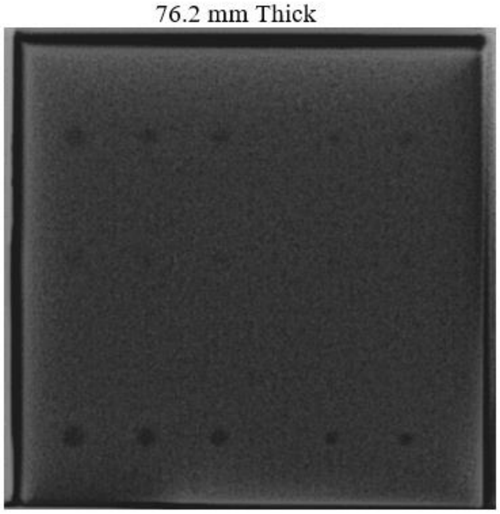

127 mm Thick

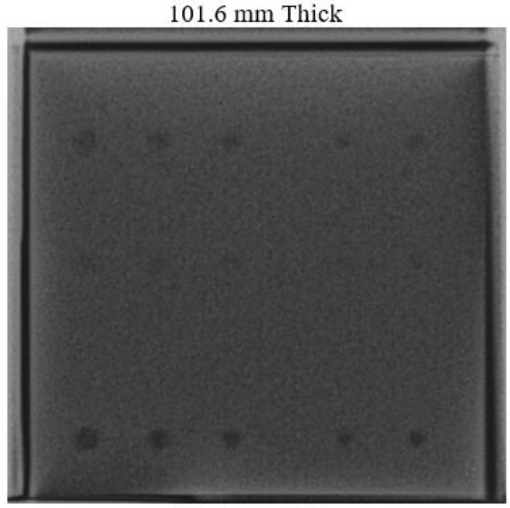

152.4 mm Thick

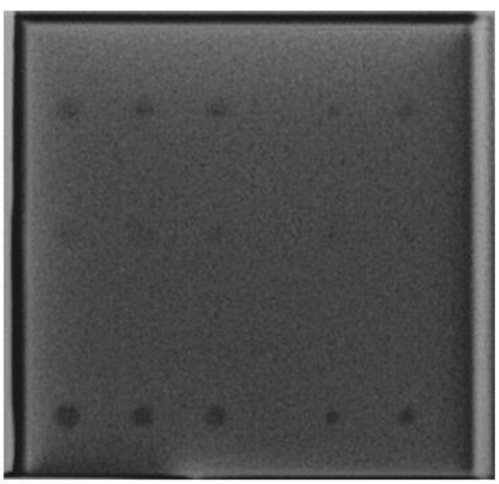

177.8 mm Thick

Figure C-3 4 Mev Radiographs

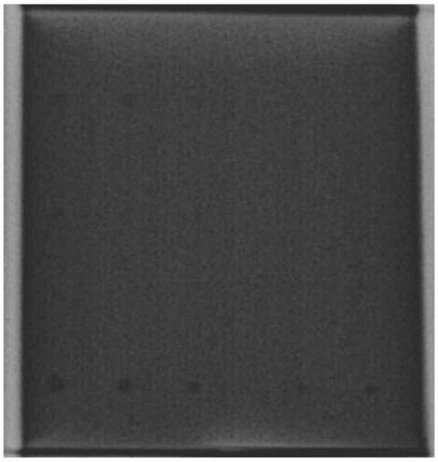

101.6 mm Thick

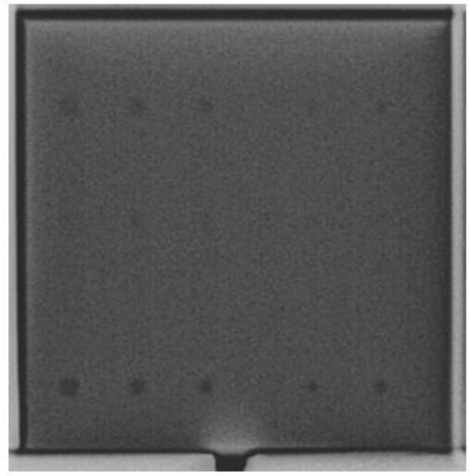

127 mm Thick

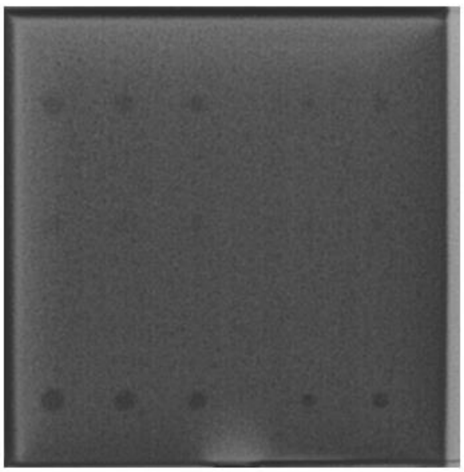

152.4 mm Thick

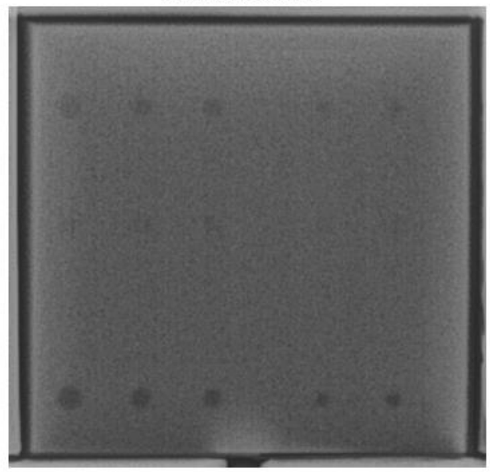

177.8 mm Thick

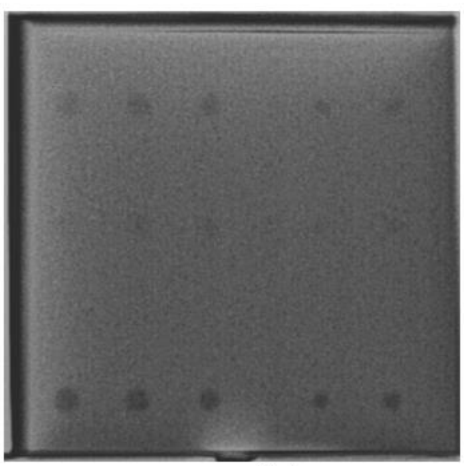

203.2 mm Thick

Figure C-4 6 Mev Radiographs

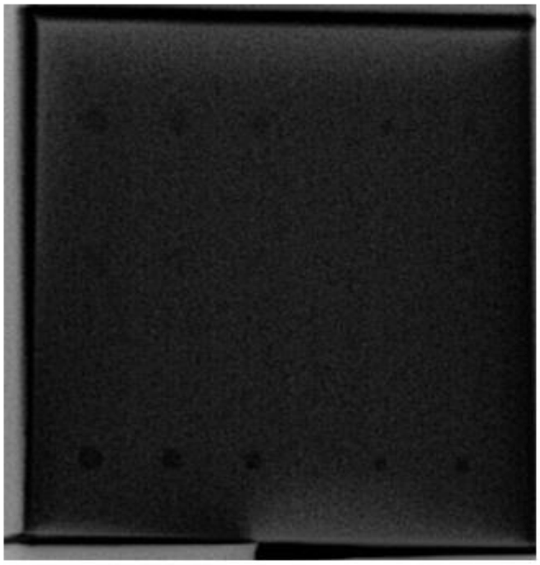

127 mm Thick

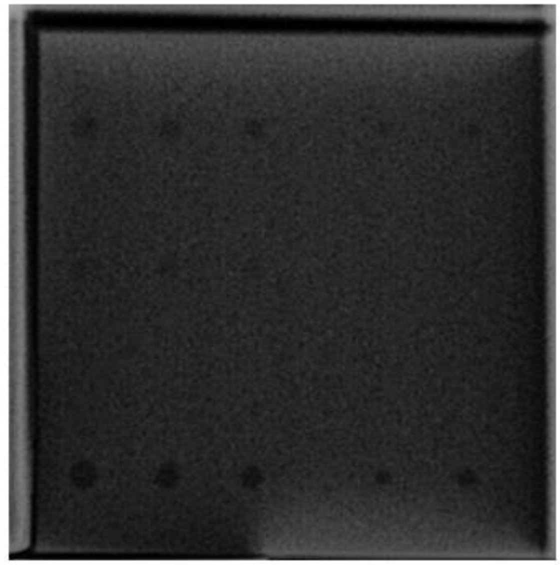

152.4 mm Thick

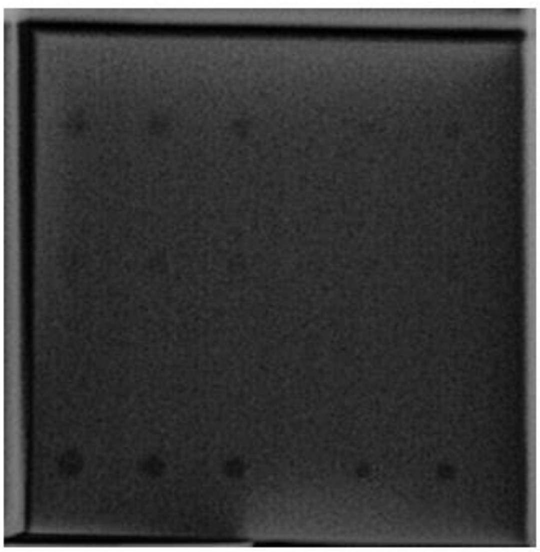

177.8 mm Thick

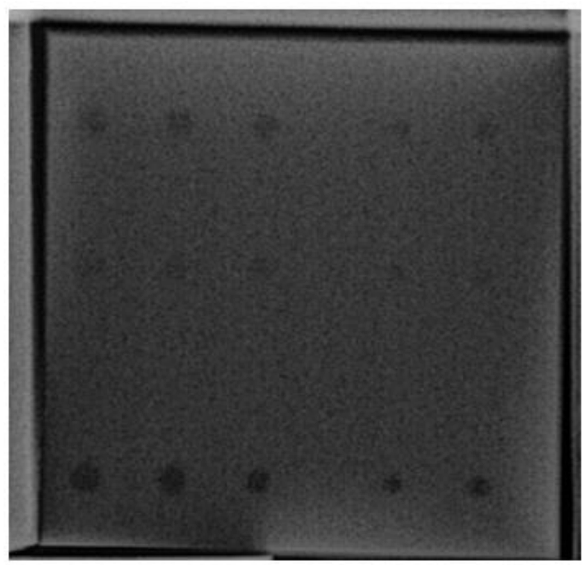

203.2 mm Thick

Figure C-5 8 Mev Radiographs

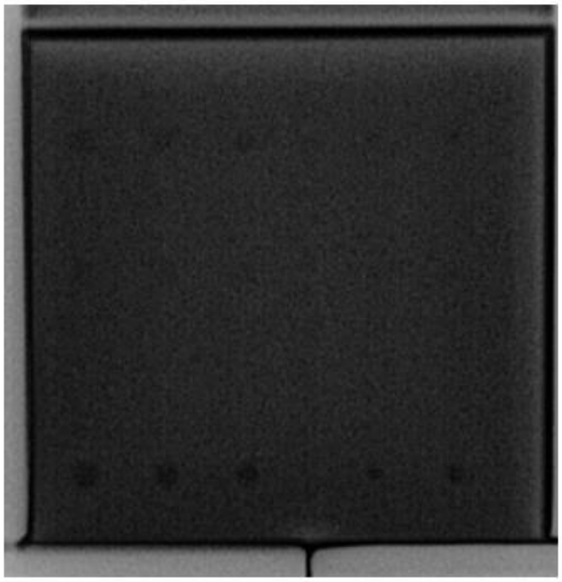

152.4 mm Thick

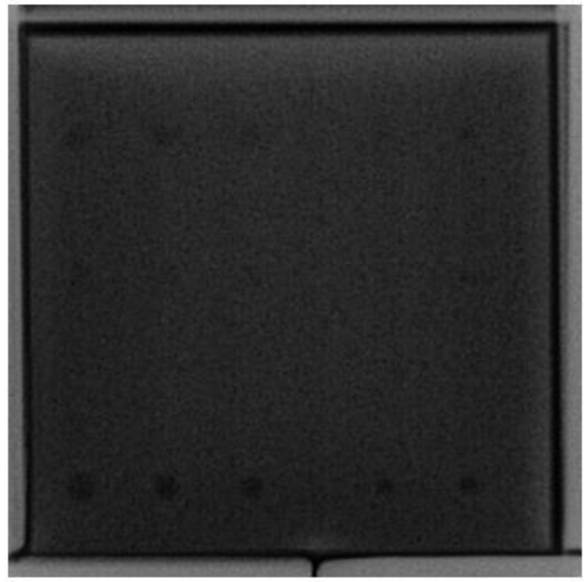

177.8 mm Thick

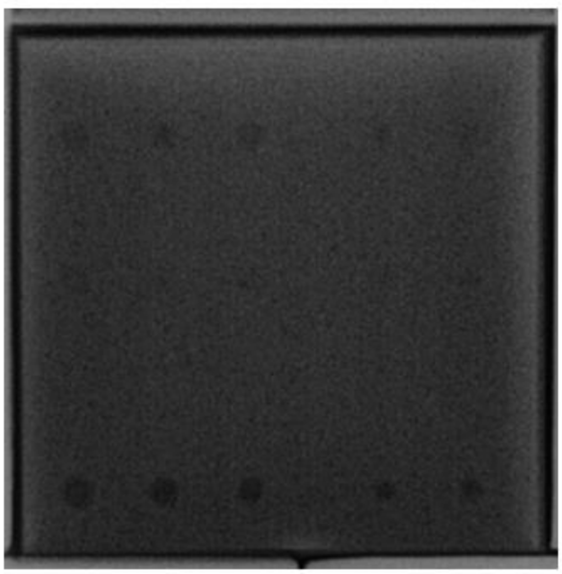

203.2 mm Thick

Figure C-6 12 Mev Radiographs

Appendix D – Probability of Detection

Table D-1 0.450 Mev probability of detection values

MeV	Block Thickness (mm)	Hole Dia. (mm)	Hole Depth (mm)	POD
0.45	25.4	1.984375	0.508	97.18%
0.45	25.4	1.5875	0.508	100.00%
0.45	25.4	1.190625	0.508	100.00%
0.45	25.4	0.79375	0.508	97.86%
0.45	25.4	0.396875	0.508	0.00%
0.45	25.4	1.984375	0.254	56.03%
0.45	25.4	1.5875	0.254	99.89%
0.45	25.4	1.190625	0.254	97.98%
0.45	25.4	0.79375	0.254	43.33%
0.45	25.4	0.396875	0.254	0.00%
0.45	25.4	1.984375	1.016	100.00%
0.45	25.4	1.5875	1.016	100.00%
0.45	25.4	1.190625	1.016	100.00%
0.45	25.4	0.79375	1.016	99.98%
0.45	25.4	0.396875	1.016	42.02%

MeV	Block Thickness (mm)	Hole Dia. (mm)	Hole Depth (mm)	POD
0.45	50.8	2.38125	1.016	99.49%
0.45	50.8	1.984375	1.016	99.94%
0.45	50.8	1.5875	1.016	99.98%
0.45	50.8	1.190625	1.016	96.68%
0.45	50.8	0.79375	1.016	20.73%
0.45	50.8	2.38125	0.508	92.61%
0.45	50.8	1.984375	0.508	100.00%
0.45	50.8	1.5875	0.508	99.08%
0.45	50.8	1.190625	0.508	87.58%
0.45	50.8	0.79375	0.508	21.99%
0.45	50.8	2.38125	2.032	100.00%
0.45	50.8	1.984375	2.032	99.98%
0.45	50.8	1.5875	2.032	99.59%
0.45	50.8	1.190625	2.032	100.00%
0.45	50.8	0.79375	2.032	91.11%

MeV	Block Thickness (mm)	Hole Dia. (mm)	Hole Depth (mm)	POD
0.45	76.2	2.778125	1.524	98.66%
0.45	76.2	2.38125	1.524	98.91%
0.45	76.2	1.984375	1.524	99.14%
0.45	76.2	1.5875	1.524	98.92%
0.45	76.2	1.190625	1.524	93.76%
0.45	76.2	2.778125	0.762	99.22%
0.45	76.2	2.38125	0.762	99.55%
0.45	76.2	1.984375	0.762	99.98%
0.45	76.2	1.5875	0.762	52.06%
0.45	76.2	1.190625	0.762	75.57%
0.45	76.2	2.778125	3.048	99.53%
0.45	76.2	2.38125	3.048	98.55%
0.45	76.2	1.984375	3.048	100.00%
0.45	76.2	1.5875	3.048	99.94%
0.45	76.2	1.190625	3.048	100.00%

MeV	Block Thickness (mm)	Hole Dia. (mm)	Hole Depth (mm)	POD
0.45	101.6	2.778125	2.032	89.02%
0.45	101.6	2.38125	2.032	99.84%
0.45	101.6	1.984375	2.032	98.48%
0.45	101.6	1.5875	2.032	98.75%
0.45	101.6	1.190625	2.032	98.67%
0.45	101.6	2.778125	1.016	69.10%
0.45	101.6	2.38125	1.016	67.36%
0.45	101.6	1.984375	1.016	88.32%
0.45	101.6	1.5875	1.016	74.46%
0.45	101.6	1.190625	1.016	15.94%
0.45	101.6	2.778125	4.064	99.73%
0.45	101.6	2.38125	4.064	95.84%
0.45	101.6	1.984375	4.064	99.99%
0.45	101.6	1.5875	4.064	99.96%
0.45	101.6	1.190625	4.064	99.43%

Table D-2 3 Mev probability of detection values

MeV	Block Thickness (mm)	Hole Dia. (mm)	Hole Depth (mm)	POD
3	50.8	2.38125	1.016	25.10%
3	50.8	1.984375	1.016	0.32%
3	50.8	1.5875	1.016	83.03%
3	50.8	1.190625	1.016	30.72%
3	50.8	0.79375	1.016	8.01%
3	50.8	2.38125	0.508	19.22%
3	50.8	1.984375	0.508	42.35%
3	50.8	1.5875	0.508	40.67%
3	50.8	1.190625	0.508	49.18%
3	50.8	0.79375	0.508	0.65%
3	50.8	2.38125	2.032	86.61%
3	50.8	1.984375	2.032	66.03%
3	50.8	1.5875	2.032	97.72%
3	50.8	1.190625	2.032	74.04%
3	50.8	0.79375	2.032	2.83%

MeV	Block Thickness (mm)	Hole Dia. (mm)	Hole Depth (mm)	POD
3	76.2	2.778125	1.524	39.32%
3	76.2	2.38125	1.524	14.73%
3	76.2	1.984375	1.524	47.43%
3	76.2	1.5875	1.524	10.61%
3	76.2	1.190625	1.524	0.00%
3	76.2	2.778125	0.762	49.89%
3	76.2	2.38125	0.762	0.96%
3	76.2	1.984375	0.762	0.01%
3	76.2	1.5875	0.762	44.41%
3	76.2	1.190625	0.762	16.89%
3	76.2	2.778125	3.048	94.45%
3	76.2	2.38125	3.048	71.70%
3	76.2	1.984375	3.048	53.13%
3	76.2	1.5875	3.048	49.59%
3	76.2	1.190625	3.048	34.18%

MeV	Block Thickness (mm)	Hole Dia. (mm)	Hole Depth (mm)	POD
3	101.6	2.778125	2.032	57.76%
3	101.6	2.38125	2.032	44.20%
3	101.6	1.984375	2.032	66.33%
3	101.6	1.5875	2.032	79.72%
3	101.6	1.190625	2.032	0.41%
3	101.6	2.778125	1.016	55.48%
3	101.6	2.38125	1.016	18.13%
3	101.6	1.984375	1.016	18.73%
3	101.6	1.5875	1.016	42.00%
3	101.6	1.190625	1.016	14.44%
3	101.6	2.778125	4.064	84.08%
3	101.6	2.38125	4.064	65.84%
3	101.6	1.984375	4.064	75.29%
3	101.6	1.5875	4.064	89.65%
3	101.6	1.190625	4.064	48.49%

MeV	Block Thickness (mm)	Hole Dia. (mm)	Hole Depth (mm)	POD
3	127	3.175	2.54	59.26%
3	127	2.778125	2.54	55.15%
3	127	2.38125	2.54	99.76%
3	127	1.984375	2.54	36.90%
3	127	1.5875	2.54	82.19%
3	127	3.175	1.27	33.73%
3	127	2.778125	1.27	58.99%
3	127	2.38125	1.27	30.45%
3	127	1.984375	1.27	1.68%
3	127	1.5875	1.27	16.31%
3	127	3.175	5.08	92.16%
3	127	2.778125	5.08	98.65%
3	127	2.38125	5.08	95.63%
3	127	1.984375	5.08	93.02%
3	127	1.5875	5.08	72.11%

MeV	Block Thickness (mm)	Hole Dia. (mm)	Hole Depth (mm)	POD
3	152.4	3.571875	3.048	0.00%
3	152.4	3.175	3.048	1.20%
3	152.4	2.778125	3.048	56.45%
3	152.4	2.38125	3.048	0.13%
3	152.4	1.984375	3.048	2.85%
3	152.4	3.571875	1.524	25.90%
3	152.4	3.175	1.524	35.17%
3	152.4	2.778125	1.524	39.90%
3	152.4	2.38125	1.524	1.32%
3	152.4	1.984375	1.524	21.35%
3	152.4	3.571875	6.096	94.14%
3	152.4	3.175	6.096	89.87%
3	152.4	2.778125	6.096	95.17%
3	152.4	2.38125	6.096	99.61%
3	152.4	1.984375	6.096	85.06%

Table D-3 4 Mev probability of detection values

MeV	Block Thickness (mm)	Hole Dia. (mm)	Hole Depth (mm)	POD
4	76.2	2.778125	1.524	25.70%
4	76.2	2.38125	1.524	71.82%
4	76.2	1.984375	1.524	54.86%
4	76.2	1.5875	1.524	51.27%
4	76.2	1.190625	1.524	72.10%
4	76.2	2.778125	0.762	69.69%
4	76.2	2.38125	0.762	14.24%
4	76.2	1.984375	0.762	0.15%
4	76.2	1.5875	0.762	13.03%
4	76.2	1.190625	0.762	0.06%
4	76.2	2.778125	3.048	90.00%
4	76.2	2.38125	3.048	89.21%
4	76.2	1.984375	3.048	93.55%
4	76.2	1.5875	3.048	91.88%
4	76.2	1.190625	3.048	69.62%

MeV	Block Thickness (mm)	Hole Dia. (mm)	Hole Depth (mm)	POD
4	101.6	2.778125	2.032	44.59%
4	101.6	2.38125	2.032	76.84%
4	101.6	1.984375	2.032	33.12%
4	101.6	1.5875	2.032	81.96%
4	101.6	1.190625	2.032	30.95%
4	101.6	2.778125	1.016	38.41%
4	101.6	2.38125	1.016	32.50%
4	101.6	1.984375	1.016	5.70%
4	101.6	1.5875	1.016	88.92%
4	101.6	1.190625	1.016	1.25%
4	101.6	2.778125	4.064	97.59%
4	101.6	2.38125	4.064	99.96%
4	101.6	1.984375	4.064	88.52%
4	101.6	1.5875	4.064	100.00%
4	101.6	1.190625	4.064	86.99%

MeV	Block Thickness (mm)	Hole Dia. (mm)	Hole Depth (mm)	POD
4	127	3.175	2.54	77.04%
4	127	2.778125	2.54	87.55%
4	127	2.38125	2.54	96.69%
4	127	1.984375	2.54	76.38%
4	127	1.5875	2.54	90.39%
4	127	3.175	1.27	49.42%
4	127	2.778125	1.27	46.94%
4	127	2.38125	1.27	25.80%
4	127	1.984375	1.27	64.36%
4	127	1.5875	1.27	67.49%
4	127	3.175	5.08	99.99%
4	127	2.778125	5.08	99.56%
4	127	2.38125	5.08	96.04%
4	127	1.984375	5.08	97.44%
4	127	1.5875	5.08	85.46%

MeV	Block Thickness (mm)	Hole Dia. (mm)	Hole Depth (mm)	POD
4	152.4	3.571875	3.048	91.60%
4	152.4	3.175	3.048	92.50%
4	152.4	2.778125	3.048	96.44%
4	152.4	2.38125	3.048	91.52%
4	152.4	1.984375	3.048	82.08%
4	152.4	3.571875	1.524	78.69%
4	152.4	3.175	1.524	91.26%
4	152.4	2.778125	1.524	81.90%
4	152.4	2.38125	1.524	70.37%
4	152.4	1.984375	1.524	56.02%
4	152.4	3.571875	6.096	99.77%
4	152.4	3.175	6.096	100.00%
4	152.4	2.778125	6.096	99.71%
4	152.4	2.38125	6.096	99.61%
4	152.4	1.984375	6.096	90.55%

MeV	Block Thickness (mm)	Hole Dia. (mm)	Hole Depth (mm)	POD
4	177.8	3.571875	3.556	98.14%
4	177.8	3.175	3.556	95.73%
4	177.8	2.778125	3.556	99.55%
4	177.8	2.38125	3.556	93.11%
4	177.8	1.984375	3.556	93.96%
4	177.8	3.571875	1.778	54.26%
4	177.8	3.175	1.778	96.53%
4	177.8	2.778125	1.778	88.05%
4	177.8	2.38125	1.778	70.26%
4	177.8	1.984375	1.778	91.70%
4	177.8	3.571875	7.112	99.21%
4	177.8	3.175	7.112	96.42%
4	177.8	2.778125	7.112	98.26%
4	177.8	2.38125	7.112	95.78%
4	177.8	1.984375	7.112	73.05%

Table D-4 6 Mev probability of detection values

MeV	Block Thickness (mm)	Hole Dia. (mm)	Hole Depth (mm)	POD
6	101.6	2.778125	2.032	26.89%
6	101.6	2.38125	2.032	43.12%
6	101.6	1.984375	2.032	31.98%
6	101.6	1.5875	2.032	59.51%
6	101.6	1.190625	2.032	0.35%
6	101.6	2.778125	1.016	45.24%
6	101.6	2.38125	1.016	15.54%
6	101.6	1.984375	1.016	2.93%
6	101.6	1.5875	1.016	88.34%
6	101.6	1.190625	1.016	0.01%
6	101.6	2.778125	4.064	87.74%
6	101.6	2.38125	4.064	81.41%
6	101.6	1.984375	4.064	91.84%
6	101.6	1.5875	4.064	91.29%
6	101.6	1.190625	4.064	83.91%

MeV	Block Thickness (mm)	Hole Dia. (mm)	Hole Depth (mm)	POD
6	127	3.175	2.54	43.82%
6	127	2.778125	2.54	53.20%
6	127	2.38125	2.54	36.08%
6	127	1.984375	2.54	75.10%
6	127	1.5875	2.54	22.75%
6	127	3.175	1.27	59.09%
6	127	2.778125	1.27	37.13%
6	127	2.38125	1.27	24.82%
6	127	1.984375	1.27	14.54%
6	127	1.5875	1.27	19.77%
6	127	3.175	5.08	88.35%
6	127	2.778125	5.08	81.21%
6	127	2.38125	5.08	86.19%
6	127	1.984375	5.08	99.67%
6	127	1.5875	5.08	56.91%

MeV	Block Thickness (mm)	Hole Dia. (mm)	Hole Depth (mm)	POD
6	152.4	3.571875	3.048	72.41%
6	152.4	3.175	3.048	90.15%
6	152.4	2.778125	3.048	98.06%
6	152.4	2.38125	3.048	78.36%
6	152.4	1.984375	3.048	41.48%
6	152.4	3.571875	1.524	69.92%
6	152.4	3.175	1.524	53.08%
6	152.4	2.778125	1.524	92.96%
6	152.4	2.38125	1.524	99.70%
6	152.4	1.984375	1.524	12.65%
6	152.4	3.571875	6.096	98.97%
6	152.4	3.175	6.096	99.97%
6	152.4	2.778125	6.096	98.98%
6	152.4	2.38125	6.096	99.76%
6	152.4	1.984375	6.096	98.42%

MeV	Block Thickness (mm)	Hole Dia. (mm)	Hole Depth (mm)	POD
6	177.8	3.571875	3.556	92.01%
6	177.8	3.175	3.556	93.65%
6	177.8	2.778125	3.556	97.41%
6	177.8	2.38125	3.556	94.82%
6	177.8	1.984375	3.556	97.53%
6	177.8	3.571875	1.778	36.17%
6	177.8	3.175	1.778	69.94%
6	177.8	2.778125	1.778	57.01%
6	177.8	2.38125	1.778	66.88%
6	177.8	1.984375	1.778	25.19%
6	177.8	3.571875	7.112	95.91%
6	177.8	3.175	7.112	97.77%
6	177.8	2.778125	7.112	92.26%
6	177.8	2.38125	7.112	95.96%
6	177.8	1.984375	7.112	79.10%

MeV	Block Thickness (mm)	Hole Dia. (mm)	Hole Depth (mm)	POD
6	203.2	3.96875	4.064	97.46%
6	203.2	3.571875	4.064	99.80%
6	203.2	3.175	4.064	98.14%
6	203.2	2.778125	4.064	99.37%
6	203.2	2.38125	4.064	99.37%
6	203.2	3.96875	2.032	26.24%
6	203.2	3.571875	2.032	99.61%
6	203.2	3.175	2.032	99.95%
6	203.2	2.778125	2.032	58.62%
6	203.2	2.38125	2.032	60.56%
6	203.2	3.96875	8.128	92.40%
6	203.2	3.571875	8.128	94.32%
6	203.2	3.175	8.128	94.67%
6	203.2	2.778125	8.128	94.74%
6	203.2	2.38125	8.128	85.00%

Table D-5 8 Mev probability of detection values

MeV	Block Thickness (mm)	Hole Dia. (mm)	Hole Depth (mm)	POD
8	127	3.175	2.54	86.09%
8	127	2.778125	2.54	72.73%
8	127	2.38125	2.54	53.91%
8	127	1.984375	2.54	53.54%
8	127	1.5875	2.54	84.16%
8	127	3.175	1.27	58.72%
8	127	2.778125	1.27	36.93%
8	127	2.38125	1.27	24.05%
8	127	1.984375	1.27	61.69%
8	127	1.5875	1.27	31.87%
8	127	3.175	5.08	90.98%
8	127	2.778125	5.08	86.43%
8	127	2.38125	5.08	95.10%
8	127	1.984375	5.08	86.31%
8	127	1.5875	5.08	58.97%

MeV	Block Thickness (mm)	Hole Dia. (mm)	Hole Depth (mm)	POD
8	152.4	3.571875	3.048	93.29%
8	152.4	3.175	3.048	85.37%
8	152.4	2.778125	3.048	88.06%
8	152.4	2.38125	3.048	79.71%
8	152.4	1.984375	3.048	36.77%
8	152.4	3.571875	1.524	56.81%
8	152.4	3.175	1.524	81.08%
8	152.4	2.778125	1.524	98.97%
8	152.4	2.38125	1.524	49.70%
8	152.4	1.984375	1.524	0.00%
8	152.4	3.571875	6.096	96.88%
8	152.4	3.175	6.096	67.32%
8	152.4	2.778125	6.096	84.89%
8	152.4	2.38125	6.096	80.77%
8	152.4	1.984375	6.096	77.95%

MeV	Block Thickness (mm)	Hole Dia. (mm)	Hole Depth (mm)	POD
8	177.8	3.571875	3.556	99.84%
8	177.8	3.175	3.556	96.05%
8	177.8	2.778125	3.556	96.37%
8	177.8	2.38125	3.556	85.86%
8	177.8	1.984375	3.556	86.85%
8	177.8	3.571875	1.778	53.58%
8	177.8	3.175	1.778	87.76%
8	177.8	2.778125	1.778	48.82%
8	177.8	2.38125	1.778	28.42%
8	177.8	1.984375	1.778	34.23%
8	177.8	3.571875	7.112	92.29%
8	177.8	3.175	7.112	91.07%
8	177.8	2.778125	7.112	92.70%
8	177.8	2.38125	7.112	91.97%
8	177.8	1.984375	7.112	89.03%

MeV	Block Thickness (mm)	Hole Dia. (mm)	Hole Depth (mm)	POD
8	203.2	3.96875	4.064	94.92%
8	203.2	3.571875	4.064	95.87%
8	203.2	3.175	4.064	95.66%
8	203.2	2.778125	4.064	94.25%
8	203.2	2.38125	4.064	96.33%
8	203.2	3.96875	2.032	30.22%
8	203.2	3.571875	2.032	91.09%
8	203.2	3.175	2.032	92.86%
8	203.2	2.778125	2.032	87.32%
8	203.2	2.38125	2.032	96.12%
8	203.2	3.96875	8.128	78.95%
8	203.2	3.571875	8.128	98.77%
8	203.2	3.175	8.128	93.80%
8	203.2	2.778125	8.128	94.95%
8	203.2	2.38125	8.128	93.16%

Table D-6 12 Mev probability of detection values

MeV	Block Thickness (mm)	Hole Dia. (mm)	Hole Depth (mm)	POD
12	152.4	3.571875	3.048	80.65%
12	152.4	3.175	3.048	67.68%
12	152.4	2.778125	3.048	72.70%
12	152.4	2.38125	3.048	83.29%
12	152.4	1.984375	3.048	14.27%
12	152.4	3.571875	1.524	50.41%
12	152.4	3.175	1.524	66.28%
12	152.4	2.778125	1.524	88.62%
12	152.4	2.38125	1.524	42.62%
12	152.4	1.984375	1.524	50.18%
12	152.4	3.571875	6.096	92.38%
12	152.4	3.175	6.096	77.34%
12	152.4	2.778125	6.096	68.90%
12	152.4	2.38125	6.096	85.99%
12	152.4	1.984375	6.096	58.24%

MeV	Block Thickness (mm)	Hole Dia. (mm)	Hole Depth (mm)	POD
12	177.8	3.571875	3.556	71.21%
12	177.8	3.175	3.556	57.26%
12	177.8	2.778125	3.556	94.13%
12	177.8	2.38125	3.556	79.03%
12	177.8	1.984375	3.556	18.96%
12	177.8	3.571875	1.778	62.29%
12	177.8	3.175	1.778	55.85%
12	177.8	2.778125	1.778	85.73%
12	177.8	2.38125	1.778	12.28%
12	177.8	1.984375	1.778	33.34%
12	177.8	3.571875	7.112	89.65%
12	177.8	3.175	7.112	91.17%
12	177.8	2.778125	7.112	72.40%
12	177.8	2.38125	7.112	91.11%
12	177.8	1.984375	7.112	79.00%

MeV	Block Thickness (mm)	Hole Dia. (mm)	Hole Depth (mm)	POD
12	203.2	3.96875	4.064	98.84%
12	203.2	3.571875	4.064	100.00%
12	203.2	3.175	4.064	89.49%
12	203.2	2.778125	4.064	40.45%
12	203.2	2.38125	4.064	82.30%
12	203.2	3.96875	2.032	60.99%
12	203.2	3.571875	2.032	26.12%
12	203.2	3.175	2.032	48.44%
12	203.2	2.778125	2.032	61.96%
12	203.2	2.38125	2.032	27.18%
12	203.2	3.96875	8.128	79.80%
12	203.2	3.571875	8.128	95.82%
12	203.2	3.175	8.128	93.09%
12	203.2	2.778125	8.128	72.71%
12	203.2	2.38125	8.128	64.53%